All Inkjet Printed Piezoelectric Polymer Actuators for Microfluidic Lab-on-a-Chip Systems

Dissertation

zur Erlangung des akademischen Grades

Doktor der Ingenieurwissenschaften (Dr.-Ing.)

Friedrich-Schiller-Universität Jena

seit 1558

vorgelegt dem Rat der
Physikalisch-Astronomischen Fakultät
der Friedrich-Schiller-Universität Jena

von

Dipl.-Ing. Oliver Pabst

geboren am 30.08.1982 in Braunschweig

Gutachter

1. Prof. Dr. Andreas Tünnermann,
   Friedrich-Schiller-Universität Jena

2. Dr. habil. Michael Wegener,
   Fraunhofer-Institut für Angewandte Polymerforschung, Potsdam

3. Dr. Ari Alastalo,
   VTT Technical Research Centre of Finland, Espoo, Finnland

Tag der Disputation: 16. Dezember 2014

Zusammenfassung

Drucktechnologien zur Herstellung elektronischer Komponenten wurden in den vergangen Jahren verstärkt untersucht, da sie einen besonders kostengünstigen Materialauftrag sowie großflächige Beschichtungen ermöglichen. Im Rahmen der vorliegenden Arbeit werden die Vorteile dieser Verfahren genutzt um piezoelektrische Aktuatoren zu erzeugen, die sich für die Integration in polymerbasierte Lab-on-a-Chip (LOC) Systeme für Einweg-Applikationen eignen. Ausgehend von analytischen Modellen zum Aktuatorverhalten werden piezoelektrische Polymeraktuatoren auf Basis von P(VDF-TrFE) (Poly(vinylidenfluorid-*co*-trifluoroethylen)) erstmals vollständig mittels Inkjet Druck-verfahren hergestellt und eingehend charakterisiert. Dabei sind die eingesetzten Prozesstemperaturen kompatibel mit kostengünstigen Polymersubstraten, die typischerweise in LOC Systemen verwendet werden. Das Verhalten gedruckter P(VDF-TrFE) Aktuatoren wird anhand des piezoelektrischen d_{31}-Koeffizienten, der remanenten Polarisation P_{rem} sowie der Morphologie für verschiedene Wärmebehandlungen der gedruckten Schichten charakterisiert. Ein signifikanter Einfluss der Wärmebehandlung auf das Aktuatorverhalten und die Morphologie der P(VDF-TrFE) Schichten wird ermittelt. Wärmebehandlungen oberhalb von 110 °C führen dabei zu signifikantem piezoelektrischen Verhalten mit d_{31} und P_{rem} von bis zu 10 pm V^{-1} bzw. 5.8 µC cm^{-2}. Die erzielten Erkenntnisse werden genutzt, um in einer Membranpumpe mit gedrucktem P(VDF-TrFE) Aktuator als Demonstrator Pumpraten von bis zu 130 µL min^{-1} nachzuweisen, was für den Einsatz in LOC Systemen geeignet ist.

Im Vergleich zum gegenwärtigen Stand der Technik sind sowohl der in dieser Arbeit vorgestellte Herstellungsprozess als auch die Untersuchungen zum Verhalten Inkjet gedruckter P(VDF-TrFE) Aktuatoren neuartig. Sie können in Kombination mit den analytischen Modellen genutzt werden, um Aktuatoren für verschiedene Anwendungen, aber auch andere piezoelektrische Bauteile wie Sensoren oder Speicherelemente auszulegen. Die niedrigen Prozesstemperaturen und der Einsatz digitaler Drucktechnologien ermöglichen die direkte und kostengünstige Integration von Aktuatoren in polymerbasierte LOC Systeme, was einen Vorteil gegenüber konventionellen, lithographie- und vakuumbasierten Prozessen darstellt. Im Gegensatz zu den meisten gegenwärtigen Mikropumpen entfällt ein Fügeschritt, der nötig wäre um einen separat gefertigten Aktuator auf einer Pumpmembran aufzubringen. Darüber hinaus sind der vorgeschlagene Herstellungsprozess und das Design kompatibel mit Prozessen und Materialien, die in LOC Systemen bereits eingesetzt werden. Sie können daher perspektivisch einen höheren Integrationsgrad und somit intelligentere LOC Systeme erzielen.

Abstract

Printing technologies for the fabrication of electronic components have emerged in recent years and have attracted interest due to their capabilities of cost-effective material deposition and their suitability for large-area coatings. In this thesis, the benefits of inkjet printing technologies are used to manufacture piezoelectric actuators that are suitable for integration in polymer-based, disposable microfluidic lab-on-a-chip (LOC) systems. Based on analytical models of actuator behavior, piezoelectric actuators with poly(vinylidene fluoride-*co*-trifluoroethylene) (P(VDF-TrFE)) as the active material are inkjet printed and characterized in detail for the first time here. The processing temperatures are compatible with cost-effective polymer substrates that are typically used in LOC systems. The performance of printed P(VDF-TrFE) actuators is characterized for different thermal treatments of the printed films by investigations of the piezoelectric d_{31} coefficient, the remanent polarization P_{rem} and morphology. The thermal treatment exhibits a significant influence on device performance and morphology. Annealing at temperatures above 110 °C yields distinct piezoelectric behavior, indicated by large d_{31} and P_{rem} values of up to 10 pm V^{-1} and 5.8 µC cm^{-2}, respectively. Furthermore, an increased degree of crystallinity of the ferroelectric β-phase is found for higher annealing temperatures. These findings are employed to demonstrate the function of a membrane pump with an inkjet printed P(VDF-TrFE) actuator as a proof of concept. Pump rates of up to 130 µL min^{-1} are realized, which is suitable for applications in LOC systems.

Compared to the state-of-the-art, the manufacturing approach introduced here as well as the established knowledge about the behavior of inkjet printed P(VDF-TrFE) actuators are novel. These findings combined with the analytical models can be employed to design actuators for different applications as well as other piezoelectric devices like sensors or memory elements. The low processing temperatures and the use of digital printing technologies enable the direct and cost-effective integration of actuator functionalities in polymeric LOC systems, which would be challenging with conventional, lithography- and vacuum-based manufacturing approaches. Different from most current micropumps, an additional assembly step is not required, which would be necessary when an actuator is manufactured separately and then attached to the pump membrane. Furthermore, the manufacturing approach and design introduced here are compatible with processes and materials that are used in LOC systems. They allow a cost-effective integration of further functionalities, leading to a higher degree of integration and thus smarter systems.

Table of contents

1 Introduction

Within the past approximately 15 years, the fields of organic and printed electronics have emerged in which printing technologies are employed for functionalities beyond graphics. Different from conventional lithography-based electronics fabrication, especially digital printing techniques like drop-on-demand inkjet offer a cost-effective and extremely flexible material deposition. Using this technique, solutions or dispersions of various functional materials can be deposited with high resolution in an additive way. Drop-on-demand inkjet printing is a data-driven process; therefore no masking is required. Examples of printable components include organic light emitting diodes, organic photovoltaics, memory elements and RFID antennas [1]. Processing can be performed at low temperatures and often in ambient atmosphere, which enables the use of cost-effective and flexible polymer substrates. Furthermore, large-scale manufacturing is possible when processing is compatible with roll-to-roll processing lines that are common in graphic printing [2].

Actuators represent a key element in technical applications where defined motion of a component is required and convert an input energy, mostly electrical energy, into mechanical energy. Piezoceramic actuators based on lead-zirconate-titanate ceramics (PZT) are well-established and widely used, but require high sintering temperatures above 900 °C during manufacturing [3], which is not compatible with common polymer substrate materials. Therefore, PZT actuators are typically fabricated separately and attached to other components in an additional assembly step. Alternatively, electroactive polymer actuators (EAP) offer large mechanical deflections and can be manufactured at low temperatures [4]. However, they also typically require a joining step, which increases manufacturing costs. The most common piezoelectric polymers are poly(vinyledene fluoride) (PVDF) and PVDF copolymers like poly(vinylidene fluoride-*co*-trifluoroethylene) (P(VDF-TrFE)) [5]. Screen printing has been used to deposit P(VDF-TrFE) for applications in piezoelectric and pyroelectric sensors [6,7]. However, a detailed study of the actuator behavior of printed piezoelectric polymers has not been reported up to now.

Microfluidic lab-on-a-chip (LOC) systems are also termed micro total analysis systems and implement biological or chemical analyses on a compact chip. They are often designed for point-of-care diagnostics [8,9]. In order to ensure sterile chips, the devices can be realized as single-use, disposable systems. Cost-effective manufacturing of LOC systems by polymer replication technologies is well-established [10]. When the integration of further functionalities on the chip is desired, manufacturing by low-cost techniques and using low

processing temperatures is crucial. Conventional lithography- and vacuum-based processing is well-developed and cost-effective for high production volumes of miniaturized systems, however the costs increase significantly for large chip sizes [11]. Considering the relatively large chip sizes that are common in LOC systems (typically 25.5 × 75.5 mm^2) [12], this limits the applicability of lithography-based processing. Controlled fluid transport by pumps represents a key functionality in LOC systems and is currently typically realized off-chip. As an alternative, various approaches for manufacturing micropumps have been reported [13]. Most micropumps are designed as reciprocating membrane pumps, in which a periodic membrane movement generates a volume change in the underlying pump chamber that is converted to a directed fluid flow by the help of valves [13]. Actuation in such pumps is often realized using piezoceramic PZT elements [14]. Alternatively, also electroactive polymers as pump actuators have been reported [15]. The actuators are typically manufactured separately and mounted on the pump membrane in an additional assembly step; no additive manufacturing of a piezoelectric polymer micropump actuator by printing technologies has been reported up to now.

As a basis for the work summarized in this thesis, the following open research topics are identified: (i) The direct integration of electronic functionalities in disposable, polymer-based LOC systems requires cost-effective and low-temperature alternatives to conventional lithography-based processes. (ii) A detailed characterization of the actuator behavior of printed piezoelectric polymers has not been reported up to now. (iii) Assembly steps required to mount piezoelectric actuators on polymer-based micropumps could be avoided by additive manufacturing approaches for actuators.

These topics are targeted by the following three main aspects. (i) A novel process chain for manufacturing P(VDF-TrFE) actuators based on cost-effective inkjet printing is established that is compatible with temperature-sensitive polymer substrates typically used in LOC systems. (ii) The first detailed characterization of printed P(VDF-TrFE) actuators is presented. (iii) A novel membrane pump is manufactured and characterized, which features a piezoelectric polymer actuator that is printed directly onto the pump membrane.

The manufacturing approach introduced here is used to inkjet print a sandwich structure of two silver electrodes and a P(VDF-TrFE) layer subsequently onto a passive polymer substrate. In order to ensure compatibility with temperature-sensitive polymer substrates, the processing temperatures have to be lower than approximately 150 °C, preferably below 130 °C [16]. Therefore, low-temperature sintering techniques are employed

for sintering the as-printed silver nanoparticle dispersions used for the electrodes. The performance of printed P(VDF-TrFE) actuators is investigated by ferroelectric hysteresis measurements as well as static and dynamic deflection measurements. It is well-known that an annealing step leads to an increased crystallinity in the ferroelectric β-phase of P(VDF-TrFE), which results in distinct piezoelectric behavior. This has been reported for spin-coated films [17,18], but not yet for printed P(VDF-TrFE) films. Therefore, the influence of different thermal annealing steps applied to the as-printed P(VDF-TrFE) films on actuator performance and morphology is studied here for the first time. Furthermore, analytical models for actuator behavior are adopted in order to predict the device performance. Finally, the basic functionality of the actuators in a reciprocating membrane pump with passive valves is demonstrated. Pump rates in the range of 10 $\mu L\,min^{-1}$ to 100 $\mu L\,min^{-1}$ with a membrane diameter of 15 mm at maximum are aimed at, which is appropriate for typical applications in LOC systems [19] and considers typical chip sizes in LOC systems [12]. The goal of these investigations is to establish a process chain and knowledge about performance parameters in printed P(VDF-TrFE) films that can be used to design actuators as well as other piezoelectric devices like sensors or memory elements. Furthermore, the suggested manufacturing route is compatible with the integration of further on-chip functionalities.

The thesis is structured as follows: Chapter 2 reviews the state-of-the-art in organic and printed electronics, electroactive polymer actuators with special attention to PVDF and its copolymers, as well as micropumps. Chapter 3 contains analytical models of piezoelectric actuators configured as cantilever bending beams and membrane actuators. The influence of geometry variations and material properties on the actuator behavior is studied. Chapter 4 describes the novel manufacturing process that has been developed. Aspects of the required sintering or annealing steps after printing of each layer are covered. Chapter 5 provides a study of the piezoelectric behavior and the morphology of the printed layers with respect to different thermal treatments of the as-printed films. The actuator behavior, characterized by the d_{31} coupling coefficient and the remanent polarization P_{rem} is studied. Correlations between morphology and device performance are set up, leading to processing recommendations. In chapter 6, the static and dynamic actuator behavior is investigated for cantilever and membrane actuators in different geometries. Furthermore, the device stability is studied. A basic pump demonstrator with an inkjet printed P(VDF-TrFE) actuator is presented in chapter 7. The behavior of the pump is characterized by measurements of the liquid flow rate with respect to backpressure. The thesis concludes with a summary and outlook in chapter 8.

2 Concepts and state-of-the-art in organic electronics and piezoelectric polymer actuators

This chapter provides an overview of basic concepts and the state-of-the-art in the fields that are most relevant for this thesis. The overview starts with an introduction to printed and organic electronics and points out examples of printed materials and devices. Special attention is paid to aspects of low-temperature processing on polymer substrates. Afterwards, electroactive polymer actuators are discussed. A separate section focuses on properties, structure and applications of piezoelectric polymers based on PVDF and its copolymers. Finally, different types of pumps for applications in microfluidic lab-on-a-chip systems are described. The aim of this chapter is to introduce basic concepts and recent developments in the research fields that are related to this work.

2.1 Printed and organic electronics

The generation of electronic functionalities by printing processes has gained increased attention in recent years. Early works on printed organic and inorganic transistors were published by Bao et al. [20], Ridley et al. [21], Sirringhaus et al. [22] and Kawase et al. [23] and gave rise to the growing field of printed and organic electronics. In this field, solutions or dispersions of functional materials like metal nanoparticles or semiconducting polymers, can be applied on different substrates using techniques that are well-known from text and graphic printing [24]. Despite these benefits, limitations in performance, reliability and technology readiness have avoided a significant market entry of printed electronics [25]. Optimistic early expectations like “Print your next PC” [26] remain visions hitherto. However, especially the potential low processing costs of printed electronics qualify it for applications in disposable products, where manufacturing with conventional technologies is economically not feasible.

Table 2.1 lists up common printing techniques that have been used for printed electronics applications and points out key parameters. In flexo, gravure and offset printing, ink transfer to the substrate is realized by mechanical contact between the substrate and a flexible printing plate (flexo), metallic roll (gravure) or an offset cylinder. Using these techniques, high printing speeds can be realized. In screen printing, pastes or inks are pushed through a patterned screen or mesh onto the substrates. Depending on the mesh geometry, relatively thick layers (up to 100 µm) can be obtained [24]. For all contact-type printing

techniques, initial costs for the printing plates, rolls or meshes are present, which makes the techniques cost-effective only for large production volumes.

Table 2.1 Overview of printing techniques commonly used in the field of printed electronics, adapted from [24].

Technique	Print resolution (µm)	Print speed (m min^{-1})	Wet film thickness (µm)	Ink viscosity (mPa s)
Flexo printing	30 – 75	50 – 500	0.5 – 8	50 – 500
Gravure printing	20 – 75	20 – 1000	0.1 – 5	50 – 200
Offset printing	20 – 50	15 – 1000	0.5 – 2	20000 – 100000
Screen printing	50 – 100	10 – 100	3 – 100	500 – 50000
Inkjet printing	30 – 75	1 – 100	0.3 – 20	1 – 40 [a]
Aerosol printing [27]	≈ 10	6 – 12	0.1 – 2	1 – 10000

[a] Typically, inks with viscosities up to 40 mPa s at room temperature can be deposited using inkjet printing. Materials with higher viscosities have been printed when the viscosity was reduced to 20 to 40 mPa s by heating [28].

Inkjet printing, in contrast, is a non-contact, data-driven and mask-free printing technique where droplets of a liquid, the "ink", are ejected from a nozzle. The breakup of a jet of liquid into individual droplets was described by Rayleigh already in 1878 [29] and forms the basis of current inkjet printers. Inkjet printers can be classified into continuous-jet and drop-on-demand devices (see Figure 2.1).

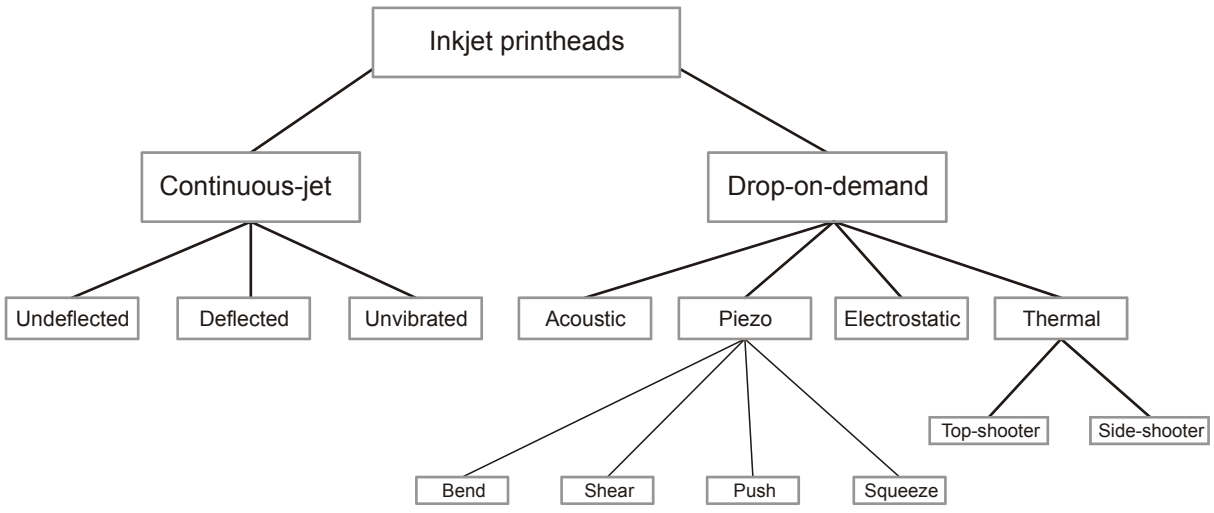

Figure 2.1 Overview of different inkjet printing principles, adapted with permission from reference [30], originally published in reference [31].

In continuous inkjet printers, a continuous stream of droplets is generated and is typically deflected electrostatically for printing generic layouts. Nowadays, continuous inkjet printers are mostly used for marking purposes, e.g. on food packages [30]. Drop-on-demand

inkjet printers generate individual droplets of ink mostly by means of a piezoelectric actuator (piezo inkjet) or a heating element (thermal inkjet or bubble jet). Droplets can also be generated using acoustic or electrostatic actuation, however piezoelectric and thermal inkjet printheads dominate the market [31]. In thermal inkjet printheads a vapor bubble is generated by a resistive heater, which leads to the ejection of a droplet. They are mostly used in graphic printing and can be further divided based on the placement of the heater into top or side shooter printheads. For printing of functional materials, piezoelectric inkjet printheads are most commonly used because they are able to dispense a wider range of solvents compared to thermal inkjet printheads [30]. An important advantage of drop-on-demand inkjet printing is its high flexibility. As processing is fully data-driven, changes to the design do not result in additional costs for masks, which is a clear advantage compared to contact-type printing techniques and conventional lithography-based processes.

Aerosol jet printing is a different drop-on-demand printing technique in which an aerosol of ink is directed through an orifice using a stream of a carrier gas for aerodynamic focusing. Using aerosol jet, feature sizes down to 10 µm can be realized, but the technology is currently available with single or few parallel orifices only [27], which limits processing speed.

Within the past years, results on various inkjet printed organic and inorganic functional materials and devices have been reported [1,32-34]. Radio-frequency identification (RFID) antennas represent a prominent application of printing technologies [35,36] and typically consist of only one printed electrode layer. Organic light-emitting diodes (OLEDs) require printing of multiple layers (electrodes, emitting layer, hole and electron transport layers) [37,38] and have been printed by different research groups for applications such as lighting or displays. Their complementary devices, organic photodiodes (OPD) and organic photovoltaic (OPV) devices have also been studied and all-printed OPDs with different layer setups have been reported [39-41]. Recent focuses in research on OPV have been optimizing of the organic semiconducting materials e.g. by combinatorial screening [42] and up-scaling of the processes to roll-to-roll lines for large-area solar cell production [43]. Apart from optical applications, printing of memory devices as key components in electronic systems has been studied. Write-once-read-many memories [44] as well as rewriteable non-volatile memories [45] have been reported. For sensing applications, pyroelectric sensors for temperature measurements [6] as well as piezoelectric pressure sensors based on PVDF

copolymers have been fabricated [7]. Furthermore, results on inkjet printed chemical sensors for the detection of volatile organic compounds were reported [46,47].

For good performance of printed devices, precise control of the printed features is necessary. Aspects of composition of the polymer solutions [42,48] as well as suppression of interlayer dissolving have been investigated. When using inkjet printing, film formation or line morphology of the printed patterns depend on the drying behavior of the printed droplets. The so-called coffee drop effect leads to ring stains of liquid drops, similar to droplets of dried coffee. The reason for this effect is the higher solvent evaporation rate at the outer boundary of the droplet, which leads to a capillary flow and thus a mass transport to the boundary, leaving a ring-shaped structure [49]. The morphology of printed structures can be controlled by adapting the solvent system in the ink as well as the substrate temperature during printing [50].

Electrical contacts in printed electronic devices are often realized using metal nanoparticle dispersions that are mostly based on silver or gold, but also copper, nickel and aluminum nanoparticle dispersions have been reported [16]. Typical particle diameters in such dispersions are in the range of 5 nm to 50 nm. Due to the small particle size, the melting or sintering temperatures are reduced significantly compared to the bulk melting temperature [51]. However, for sufficiently high conductivities sintering temperatures above 150 °C are still required usually. This is not compatible with temperature-sensitive low-cost polymer substrates and therefore requires temperature resistant and expensive polymers such as polyimide [16]. Several alternative sintering techniques that are compatible with temperature-sensitive substrates have been investigated. Localized sintering with laser [52,53] or ultraviolet radiation [54] and global sintering with xenon flash lamps [55-57] have been demonstrated for different types of metal nanoparticle inks. Contact and contactless electrical sintering [58,59], exposure to low-pressure plasma [60,61] or atmospheric-pressure plasma [62,63] as well as microwave radiation [57,64] have been employed successfully to metal nanoparticle dispersions. Furthermore, chemical reactions can trigger sintering of printed silver features [65,66]. These low-temperature sintering techniques allow processing on temperature-sensitive and low-cost polymer substrates, which brings printed electronics closer to applications.

2.2 Electroactive polymer actuators

Actuators are key components in systems where defined motion of a part is needed. Prominent examples for applications of actuators are piezoelectric fuel injection nozzles in automotive engines, electrostatically actuated digital micromirror devices in video projectors or pumps, e.g. for drug delivery [67]. Piezoelectric ceramic actuators are widely used, well-established and are often based on PZT [3]. They offer reproducible performance and are employed in many applications like in highly precise nanopositioning systems for microscopy [68], ultrasonic transducers or for droplet ejection in piezoelectric inkjet printheads [69]. Additive deposition of PZT thick films is possible when screen printing [70,71] or inkjet printing is used [72]. One drawback of piezoceramic materials are the high sintering temperatures required during manufacturing, which are typically in the range of 900 °C to 1250 °C [3]. Therefore, manufacturing is not compatible with low-cost polymer materials and a joining step is required where a separately manufactured actuator is applied to a polymer component.

In recent years, actuators based on polymeric materials have been studied intensively due to their relatively large deflections and low processing temperatures. Due to their ability to generate large strains and thus their similarity to human muscles for specific actuator types, they have also been named “artificial muscles” [4]. Electroactive polymer actuators are often divided by the principle of operation into ionic and electronic EAP [73,74]. Table 2.2 contains a classification of ionic and electronic EAP and examples of materials for the different sub-categories.

In ionic EAP, ion transport in a liquid electrolyte is induced electrically and leads to a volume change. Actuation requires only low voltages of few volts, but high currents [74]. Examples of ionic EAP are polymer gels [75,76], ionic polymer-metal composites (IPMC) [77], conducting polymers [78-80], and carbon nanotubes [81]. Ionic EAP need to be operated in a liquid medium, which is undesired for certain tasks. Furthermore, the response to an applied electric input signal is relatively slow, typically in the range of seconds. However, it is expected that they might be suitable for operation in biological environments in implantable medical devices [74].

In electronic EAP, on the other hand, actuation is caused by the application of an electric field. Compared to ionic EAP, higher electric fields in the range of 100 V μm^{-1}, but lower currents and in total less electric power are required for driving the actuators. The mechanical response does not depend on the diffusion of ions and therefore the actuators can

be driven with frequencies up to the MHz range. Furthermore, the actuators do not require operation in a liquid electrolyte and can thus be driven in air [74]. The piezoelectric effect in PVDF was described for the first time by Kawai in 1969 [82]. Piezoelectric and ferroelectric polymers, especially based on PVDF and its copolymers, have been studied intensively since then [5,83]. For industrial purposes, they are used as hydrophones (underwater microphones) in naval applications [84] or as pressure sensors in diesel injection lines [85]. Apart from that, the high chemical durability of PVDF has made it a prominent material for coating of chemical processing equipment [86].

Table 2.2 Classification of electroactive polymer actuators (EAP), adapted from reference [74].

EAP class	EAP sub-categories	Examples of materials
Ionic EAP	Polymer gels	Poly(acrylic acid)
	Ionic polymer-metal composites (IPMC)	Metalized ion exchange membranes, e.g. Nafion/Pt
	Conducting polymers	Polypyrrole (PPy) Polyanniline (PANi)
	Carbon nanotubes	Single-walled nanotubes / multi-walled nanotubes
Electronic EAP	Piezoelectric polymers	Poly(vinylidene fluoride) (PVDF) and its copolymers
	Electrostrictive polymers	Electrostrictive paper
	Liquid crystal elastomers	ferroelectric liquid crystalline elastomers (FLCEs)
	Dielectric elastomers	Silicone elastomers, acrylic elastomers, polyurethane elastomers

Other types of electronic EAP include electrostrictive polymers like high-energy-electron irradiated PVDF copolymers [87] or liquid crystal elastomers [88]. Dielectric elastomer actuators are a further type of electronic EAP that have attracted attention due to their extremely large strains of more than 100% that have been reported [89,90]. In those actuators a passive elastomer like silicone rubber (poly(dimethyl siloxane), PDMS) or an acrylic elastomer is coated with electrodes. When a voltage is applied across the polymer, the actuator gets compressed in thickness due to electrostatic Maxwell stress and expands laterally [91]. Due to the large strains, the electrodes have to be compliant to achieve sufficient cyclic stability of the actuators, which is the main issue in dielectric elastomer actuators up to now [92]. Possible realizations of compliant electrodes include carbon powder [93], structured metal electrodes [94] or graphene [95].

2.3 Piezoelectric P(VDF-TrFE) copolymers

Among the electroactive polymer materials discussed in the previous section, piezoelectric polymers based on PVDF and its copolymers are the most established EAP materials currently [5]. Commercial applications of PVDF-based devices include hydrophones with bandwidths up to 80 MHz [96,97] and ultrasonic transducers [98]. This section focuses on the specific properties of P(VDF-TrFE) copolymers.

The direct piezoelectric effect describes the generation of charges as a response to an applied mechanical stress that is present in certain crystalline materials that do not exhibit a center of symmetry. This effect is used in piezoelectric sensors, where a mechanical stress is converted to an electric signal. The indirect or converse piezoelectric effect, on the other hand, describes the mechanical response of a piezoelectric material to an applied electric field and is employed in piezoelectric actuators [99]. In piezoelectric polymers like PVDF [82] or P(VDF-TrFE), ferroelectric behavior is caused by (i) the presence of a large dipole moment associated to the presence of fluorine atoms in the polymer backbone, (ii) alignment of the dipole moment of the repeating units by an appropriate conformation and (iii) the presence of a crystal structure with aligned dipole moments of different polymer chains. When the ferroelectric materials are poled by applying an electric field, piezoelectric behavior is obtained [17]. Compared to piezoelectric polymers, PVDF and P(VDF-TrFE) exhibit high piezoelectric responses at room temperature [100,101].

Table 2.3 compares piezoelectric and mechanical properties of PVDF and P(VDF-TrFE) with inorganic piezoelectric materials like PZT and quartz. Piezoelectric polymers exhibit a significantly lower Young's modulus Y compared to PZT or quartz, and require larger electric fields in the range of 40 V μm^{-1} for poling or driving. The piezoelectric coupling coefficient d_{31} of piezoelectric polymers is significantly lower than for PZT, and the effect has an opposite sign. Therefore, P(VDF-TrFE) will expand while a PZT film will contract when a similar electric field is applied, and vice versa. Due to the low Young's modulus of piezoelectric polymers, significant actuator deflections can be generated despite the relatively low d_{31} coefficients. However, blocking forces of such actuators are lower than for ceramic actuators.

Table 2.3 Properties of PVDF and P(VDF-TrFE), compared to quartz and piezoceramic PZT, adapted from references [99,102]. Young's modulus Y, density ρ, typical electric driving field E, piezoelectric coefficient d_{31}, Curie temperature T_C and relative permittivity ε_r are compared.

Material	**Y** (GPa)	**ρ** (kg m^{-3})	**E** (V µm^{-1})	**d_{31}** (pm V^{-1})	**T_{Curie}** (°C)	**ε_r**
PVDF	3	1780	≈ 40	20	[a]	9.5 – 13.5 @ 100 Hz [103]
P(VDF-TrFE) (55 wt% VDF)	1.2	1900		25	≈ 70	18
P(VDF-TrFE) (70 wt% VDF)	2.0	1880		10 [104]	110 [105]	14 @ 1 MHz [105]
PZT	≈ 80	7500	≈ 2	-110	≈ 250	2400 @ 1 kHz [b]
Quartz	≈ 75	2650		2	573	4.5

[a] The Curie temperature of pure PVDF is estimated to be 195 to 197 °C [18], which is above the melting temperature.
[b] Value for PI Ceramic material type PIC151 [106].

Pure PVDF is not suitable for processing with printing techniques, because mechanical stretching is required to achieve a high degree of crystallinity in the ferroelectric β-phase and thus piezoelectric behavior [107]. Furthermore, pure PVDF is insoluble in many common solvents [86], thus making the preparation of a printable solution challenging. P(VDF-TrFE) copolymers with a VDF content of more than approximately 50%, however, crystallize directly into the β-phase when cooled from melt to room temperature [17]. It is known that a thermal annealing process improves the piezoelectric behavior as it increases the degree of crystallinity of the P(VDF-TrFE) films. The influences of annealing, polymer composition and mechanical treatment on morphology have been studied widely [108]. Crystallographic methods like X-ray diffraction (XRD), differential scanning calorimetry (DSC) or Fourier-transform infrared spectroscopy (FTIR) have been employed to study the presence of the oriented *all-trans* ferroelectric β-phase and the paraelectric (non-piezoelectric) *gauche-trans* α-phase in P(VDF-TrFE) films [108-110] and nanostructures [111,112]. The transition between these phases is a solid-solid phase transition and has also been studied widely for different polymer compositions [17,113]. Depending on the thermal and processing history of the samples, the temperature of this Curie transition T_C can vary by several 10 K. For a VDF:TrFE ratio of 70:30 wt% it is typically in the range of 100 °C to 120 °C [17]. Electrical poling of the films is required to align the dipoles and can be realized either by directly

applying a voltage to electrodes on the film or by corona poling, in which electric fields are applied without adding electrodes directly to the polymer film in a capacitor-like arrangement [114]. Poling at room temperature or at elevated temperatures [115] can also lead to a partial transformation from the paraelectric to the ferroelectric phase and can thus further improve the piezoelectric behavior [17]. The glass transition temperature T_G of the amorphous portion of semi-crystalline P(VDF-TrFE) films depends on the polymer composition and has been reported to be in the range of -20 °C to -40 °C [116,117]. The influence of a thermal annealing of P(VDF-TrFE) films on morphology and the mechanical properties of the films was investigated by Hahm and Kang [118]. The authors reported a strong relationship between the microstructure and the Young's modulus of the films. Mao et al. [18,119] published the first reports that investigate direct correlations between annealing temperature, film morphology and electrical behavior of P(VDF-TrFE) films (VDF content 70%) prepared by spin-coating. The electrical behavior was investigated by measuring dielectric hysteresis curves. It was found that annealing at or slightly above the Curie transition (approximately 110 °C) leads to high crystallinity of the films and large remanent polarization P_{rem}. For films annealed above their melting temperature of approximately 150 °C, a degraded β-phase and decreased polarization were reported. Figure 2.2 shows atomic force microscopy (AFM) images of P(VDF-TrFE) films annealed at different temperatures that were used in Mao's work.

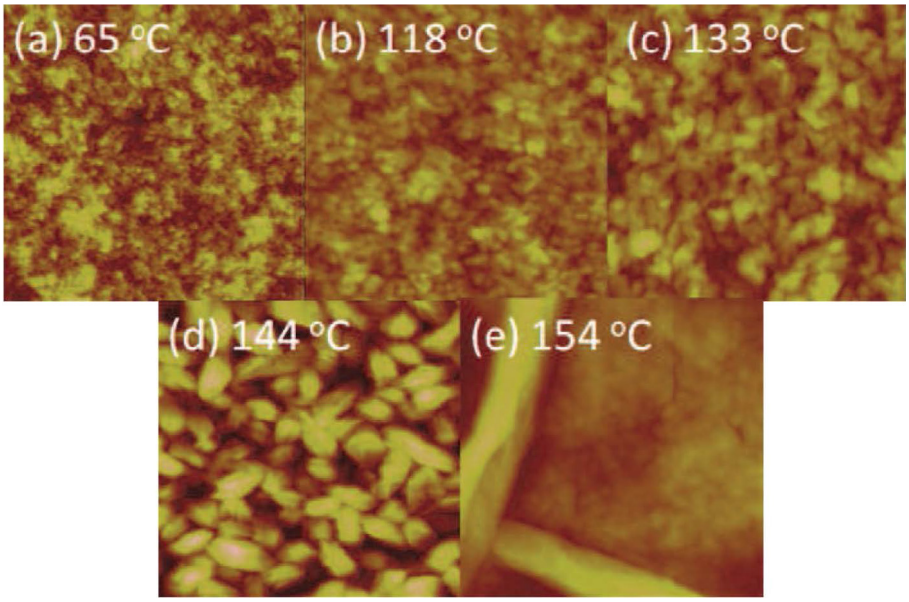

Figure 2.2 AFM images (1 × 1 μm^2) of spin-coated P(VDF-TrFE) films annealed at different temperatures. Reprinted with permission from reference [18], p. 91. © 2011 Duo Mao, Bruce E. Gnade, Manuel A. Quevedo-Lopez. Originally published under CC BY-NC-SA 3.0 license. Available from: http://dx.doi.org/10.5772/17147.

However, it is known from other polymer materials that spin-coating yields different morphologies than inkjet printing [120]. A detailed study of the relationship between the piezoelectric behavior and the morphology of inkjet printed P(VDF-TrFE) films, as used in the work presented here, has not been reported up to now.

Few reports have dealt with the deposition of P(VDF-TrFE) solutions using printing technologies. Zirkl et al. [6,7] have used screen printed P(VDF-TrFE) solutions with 70 wt% VDF content as a piezoelectric and pyroelectric sensor dielectric for printed sensor networks. The authors reported remanent polarization values of 7 $\mu C\ cm^{-2}$. Inkjet printing of P(VDF-TrFE) solutions has been reported by Zhang et al. [15,121]. The reports focus on solution preparation and printability, but not on the performance of actual printed devices. Printed loudspeakers on paper substrates with an active P(VDF-TrFE) layer and polymer electrodes based on PEDOT:PSS were reported by Hübler et al. [122]. A P(VDF-TrFE) solution in cyclopentanone with a VDF content of 75 wt% was deposited using flexography printing.

2.4 Micropumps for lab-on-a-chip systems

Microfluidic lab-on-a-chip systems integrate biological or chemical analysis tasks on a compact chip. They have gained increased interest since the introduction of the concept of miniaturized total analysis systems by Manz et al. in 1990 [8]. For point-of-care applications, single-use disposable LOC systems are often made from polymer substrates to reduce manufacturing costs [9]. Typically they consist of a structured polymer substrate with channels and a cover foil that seals the chip. Depending on the application, various fluidic layouts can be designed that contain different numbers and shapes of channels, reservoirs, micro-mixers or other structures. Manufacturing approaches for the substrates are well-developed and are often based on low-cost polymer replication techniques like hot-embossing or injection molding [10].

Well-defined fluid transport is crucial in most LOC systems and therefore a pumping function is required. External pumps offer excellent performance, but increase the costs of the total system. Therefore different concepts for chip-integrated pumps with typical flow rates in the range of few $\mu L\ min^{-1}$ to several $mL\ min^{-1}$ have been developed. Numerous literature reviews have covered this research field intensively [13,19,123-125]. This section therefore highlights key aspects that are relevant for this thesis. Most micropumps are designed as reciprocating membrane pumps, in which a periodically moving membrane that is mounted above a pumping chamber leads to a fluid flow in combination with valves [13]. The

functional principle of a membrane pump with passive nozzle / diffuser valves is illustrated in Figure 2.3.

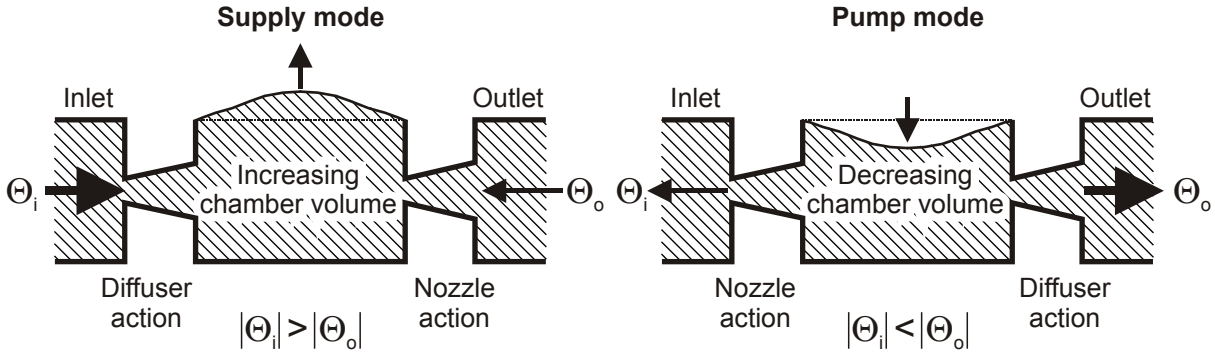

Figure 2.3 Functional principle of reciprocating membrane pumps with passive nozzle / diffuser valves, adopted from reference [14].

In the supply mode the membrane moves upward and the increasing chamber volume results in a fluid flow into the pump both from the inlet and outlet port. Due to the valve function, the flow Θ_i from the inlet port is larger than from the outlet port Θ_o. In the pump mode, the membrane moves downward and the decreasing chamber volume leads to flow out of the pump. In this mode, the flow out of the outlet port is larger than the flow out of the inlet port, thus a net fluid flow from the inlet to the outlet port is realized [14]. Actuation of the membrane is often achieved by piezoceramic PZT actuators that are mounted on a membrane made of glass, silicon or polymers [14,126-129]. Other actuation concepts include electrostatic actuators [130], electromagnetic actuators [131-133], thermo-pneumatic actuators [134,135] or shape-memory alloys [136]. Few reports have investigated electroactive polymer actuators based on IPMC [137] or electrostrictive electron-irradiated P(VDF-TrFE) [138] as pump actuators. Mounting of actuators on the pump membrane requires a separate joining step, which is sometimes undesired. Screen printing of PZT pastes has therefore been employed to generate pump actuators [126], however high sintering temperatures above 900 °C are required. Fluid transport without mechanically moving parts can be realized e.g. by electroosmotic pumps [139,140] or based on electrowetting where individual droplet are moved digitally across an array of electrodes [141].

The inlet and outlet valves of membrane pumps can be designed with or without moving parts [142]. For high pump rates and low leakage currents, active valves actuated by PZT [143] or passive valves with moving cantilevers or bridge-like structures have been proposed [144,145]. Dynamic passive valves without moving parts based on nozzle / diffuser

elements [146,147] exhibit higher leakage flow, but their simple design is beneficial for on-chip integration and manufacturing with replication techniques. A diagram that compares different micropumps from literature concerning their flow rate, backpressure and overall size has been adopted from Laser and Santiago [13] and is displayed in Figure 2.4. Additionally, the target parameters that were specified in the introduction are marked in the figure by a black ellipse. These parameters (pump rate 10 µL min^{-1} to 100 µL min^{-1}, maximum membrane diameter 15 mm) were identified based on typical pump rates [19] and chip sizes [12] in polymer-based disposable LOC systems.

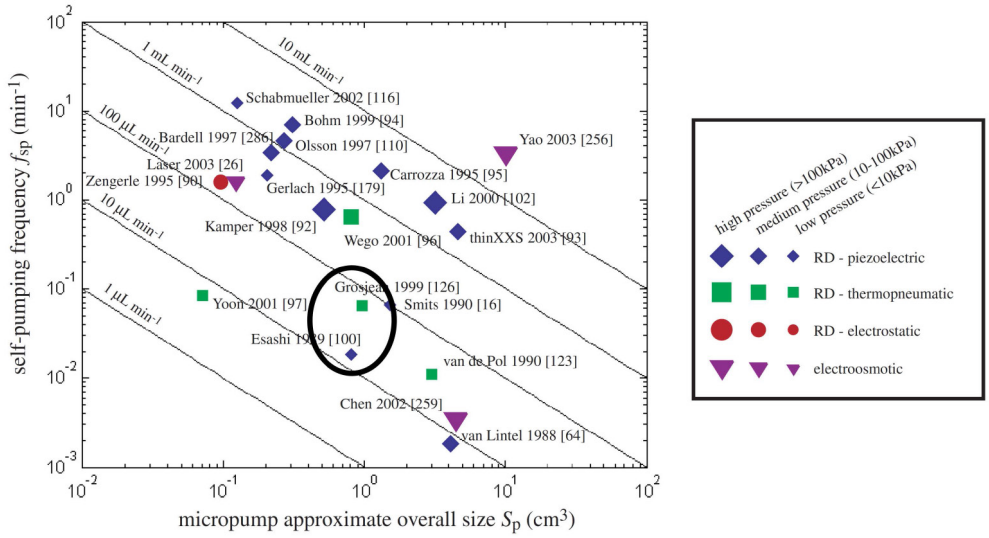

Figure 2.4 Comparison of different micropumps with respect to their flow rate Q_l, backpressure and overall size S_P. The self-pumping frequency is defined as $f_{sp} = Q_l / S_P$.

3 Modeling of actuator behavior

This chapter provides analytical models for predicting the behavior of piezoelectric polymer actuators based on P(VDF-TrFE). After a brief introduction of the fundamental equations for the indirect piezoelectric effect, an analytical model for the deflection of cantilever bending beams is discussed. The scaling of actuator deflection and force with layer setup, geometry parameters and driving boundary conditions is covered. As a second basic geometry, the behavior of circular membrane actuators is described by a separate analytical model. The volume change of an actuated membrane in a reciprocating membrane pump is derived and estimates of the flow rate in a micropump with a P(VDF-TrFE) actuator are provided. Along with the experimental derivation of the piezoelectric d_{31} coefficient of inkjet printed P(VDF-TrFE) films that is provided in chapter 5, the models presented here can be employed to design actuators for other applications than pumping tasks, too.

3.1 Piezoelectric effect

The indirect or converse piezoelectric effect describes the transformation from electrical energy to mechanical energy in a piezoelectric material. An applied electric field E leads to a mechanical strain ε_{piezo} that can be employed in piezoelectric actuators [99]. In-depth descriptions of the piezoelectric effect can be found in references [99,148]. The indirect and direct piezoelectric effect can be described by the following equations, respectively:

$$\varepsilon_{piezo} = dE \qquad D_{el} = d\sigma \,. \tag{3.1}$$

ε_{piezo} denotes the mechanical strain, d the piezoelectric coefficient, E the electric field, D_{el} the electric displacement and σ the mechanical stress. The quantities E and D_{el} are represented by first rank tensors, ε_{piezo} and σ by second rank tensors and d by a third rank tensor [99]. Written in full tensor form and adding the linear elastic and dielectric responses, equation (3.1) is expressed by

$$\varepsilon_{piezo,ij} = d_{kij}E_k + s^E_{ijkl}\sigma_{kl} \qquad D_{el,i} = \varepsilon^\sigma_{ik}E_k + d_{ikl}\sigma_{kl} \,. \tag{3.2}$$

s^E_{ijkl} is the elastic compliance tensor measured under constant electric field, and ε^σ_{ik} is the dielectric permittivity under constant stress. Due to symmetry considerations in crystalline materials, the number of independent factors in equation (3.2) can be reduced [99].

Furthermore, for flat cantilever or membrane actuators that consist of one piezoelectric layer between two electrodes on a passive substrate, the most significant actuation is characterized by the piezoelectric d_{31} coefficient. Therefore, analytical models for such unimorph piezoelectric cantilever or membrane actuators are typically simplified by considering exclusively the d_{31} coefficient [149-152]. Hence, the strain generated due to the indirect piezoelectric effect can be described by

$$\varepsilon_{piezo} = d_{31}\, E. \tag{3.3}$$

3.2 Modeling of cantilever bending beam actuators

Figure 3.1 shows a sketch of a cantilever bending beam with length L that is fixed at one end. The beam consists of a passive substrate and an active P(VDF-TrFE) layer on top. In the model used, a two-layer setup is assumed in which the passive layer represents the influence of the substrate as well as the electrodes.

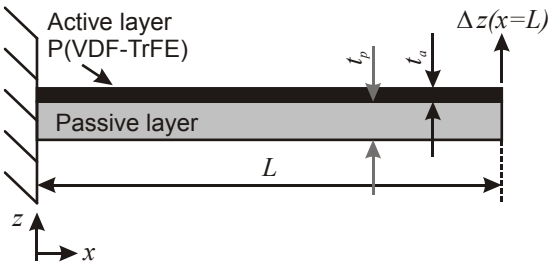

Figure 3.1 Geometry conventions used for modeling of cantilever actuators.

The behavior of cantilever beam actuators was modeled by an adapted closed-form analytical description of cantilever deflection by Hsueh [153]. Originally, the model was set up for thermal stresses; therefore thermally induced strains were replaced by strains caused by the piezoelectric effect ε_{piezo} (3.3). The resulting curvature of the cantilever r_c^{-1} is then given by

$$r_c^{-1} = \frac{Y_p^*(\tfrac{1}{2}t_p^2 + t_p t_b)\, c - Y_a^*\left[\tfrac{1}{2}t_a^2 - t_b\, t_a\right](c - d_{31}E)}{Y_p^*(\tfrac{1}{3}t_p^3 + t_p^2 t_b + t_p t_b^2) + Y_a^*\left[\tfrac{1}{3}t_a^3 - t_b t_a^2 + t_b^2\, t_a\right]}. \tag{3.4}$$

In the equation above, $Y^*_{a/p}$ are the plane strain elastic moduli and $t_{a/p}$ the thicknesses of the respective layers. Subscript a indicates the active layer, while subscript p indicates the passive layer. As the beams studied in this work are much wider than the beam thickness, the beams

can be considered to be in plane strain [149,152]. The isotropic plane strain elastic moduli are then given by

$$Y^*_{a/p} = \frac{Y_{a/p}}{(1-\nu^2)}, \tag{3.5}$$

where the Poisson's ratio ν is assumed to be 0.4 for the passive layer [154] as well as the P(VDF-TrFE) film [155]. The position of the bending axis t_b and the uniform strain component c are defined as

$$c = \frac{Y_a\, t_a\, d_{31}\, E}{Y_p\, t_p + Y_a\, t_a} \qquad \text{and} \qquad t_b = \frac{-Y_p\, t_p^2 + Y_a\, t_a^2}{2\,(Y_p\, t_p + Y_a\, t_a)}. \tag{3.6}$$

Y_p and t_p include the polymer substrate as well as both electrodes and are defined as

$$Y_p = Y_{PET}\frac{t_{PET}}{t_p} + Y_{Ag}\frac{t_{Ag,total}}{t_p} \qquad \text{with} \qquad t_p = t_{PET} + t_{Ag,total}. \tag{3.7}$$

The resulting deflection at the free end of the cantilever $\Delta z(x=L)$ is then given by

$$\Delta z(x=L) = \frac{1}{2r_c} L^2. \tag{3.8}$$

The analytical description of cantilever deflection provides a means for deriving the approximate d_{31} coefficient from measurements of actuator deflection.

The blocking force generated by a cantilever actuator is related to the free deflection by the following expression (I - second moment of area, b_c - cantilever width) [156]:

$$F_{Block} = \Delta z(x=L)\frac{3Y\,I}{L^3} \qquad \text{with} \qquad I = \frac{b_c\,(t_p+t_a)^3}{12}. \tag{3.9}$$

Table 3.1 lists typical geometry parameters as well as material properties that were employed for modeling. The length of the cantilevers was modeled up to 25 mm, which is in a range similar to the target dimensions of the micropump demonstrator. The thickness of the printed silver electrodes was modeled as 1 µm per layer, which was also confirmed by measurements on actual samples (see chapter 4). A fixed substrate thickness of 125 µm was chosen in order to ensure compatibility with typical substrate thicknesses used in commercial microfluidic chips [12]. The modeled thickness range of the printed P(VDF-TrFE) films was chosen to be 0.5 µm to 10 µm. These thicknesses can typically be realized using inkjet

printing when multiple layers are printed. Thicker layers would increase processing times and furthermore lead to high driving voltages *U*. The Young's moduli were modeled using literature values.

Table 3.1 Material and geometry parameters used for modeling of cantilever actuators.

	Substrate PET	**Electrodes** Ag	**Piezoelectric film** P(VDF-TrFE)
Cantilever length (mm)		0 to 25	
Cantilever width (mm)		7	
Layer thickness (µm)	125	2 (total)	0.5 to 10
Young's modulus (GPa)	2 [154]	40 [157]	2 [118]
Piezoelectric coefficient d_{31} (pm V^{-1})	n/a	n/a	10 [104]

In order to determine target parameters for the thickness of the P(VDF-TrFE) layers, the normalized tip deflection was modeled for a fixed substrate thickness of 125 µm and a varying thickness of the P(VDF-TrFE) layer. The resulting characteristics as well as the working range given by the process-related boundary conditions discussed above are displayed in Figure 3.2.

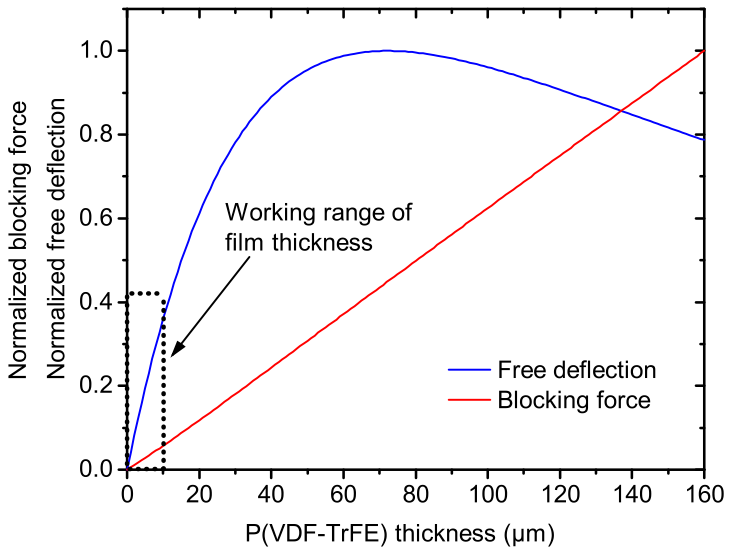

Figure 3.2 Modeled normalized free deflection and blocking force of a cantilever actuator for different thicknesses of the P(VDF-TrFE) layer. Substrate thickness was set as 125 µm.

Within the set process window for the thickness of printed P(VDF-TrFE) films, an increase in P(VDF-TrFE) thickness leads to increased free actuator deflection as well as blocking force, given the same electric driving field. For generating large actuator deflections

and blocking forces it would thus be beneficial to fabricate actuators with thick P(VDF-TrFE) films. A theoretically ideal thickness ratio would be obtained at a P(VDF-TrFE) thickness of 72 µm and would lead to maximized deflection. However, large driving voltages above 20 kV would be required for poling the films and furthermore, inkjet printing would not be a suitable technology to deposit such thick films. Therefore, a film thickness of 10 µm will be assumed in the following discussions and will also be the target thickness for actual printed devices.

Figure 3.3 plots the dependence of free actuator tip deflection and blocking force with respect to the cantilever length. With a P(VDF-TrFE) thickness of 10 µm and an electric field of 40 V µm^{-1} (driving voltage U = 400 V), deflections in the range of 50 µm to 195 µm for cantilever lengths between 10 mm and 20 mm are expected.

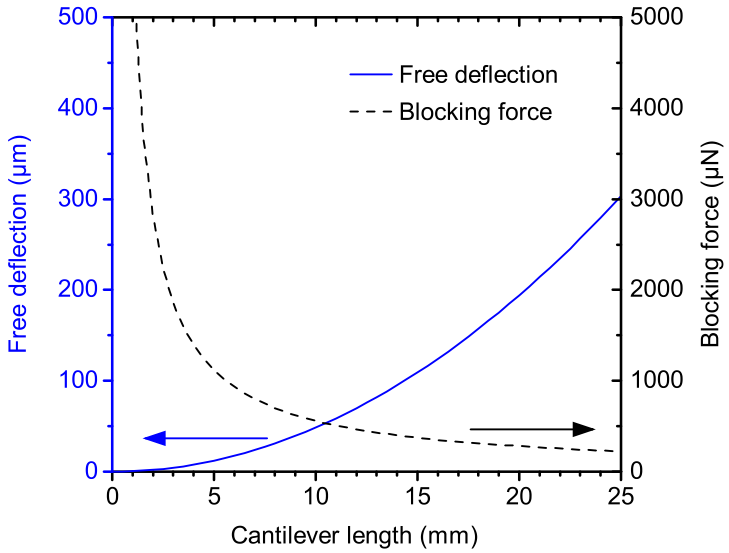

Figure 3.3 Modeled free deflection and blocking force of a cantilever actuator with varying cantilever length and a 10 µm-thick P(VDF-TrFE) film.

These values will be taken as a basis to compare with measured deflections from printed devices. The corresponding blocking forces are in the range of 280 µN to 560 µN and decrease with increasing cantilever length. In order to estimate the effect of geometry variations of the printed P(VDF-TrFE) films on device performance, Figure 3.4 plots the actuator deflection and blocking force for deviations in film thickness of up to ± 2 µm and deviations in cantilever lengths of up to ± 0.5 mm from the target value. With these geometry variations, deviations in deflection and blocking force of approximately 10% and 4% result, respectively. Furthermore, it has to be noted that rough P(VDF-TrFE) layers or tolerances in thickness lead to locally increased driving fields that might increase the risk for dielectric breakdown of the P(VDF-TrFE) films along with local defects like pinholes.

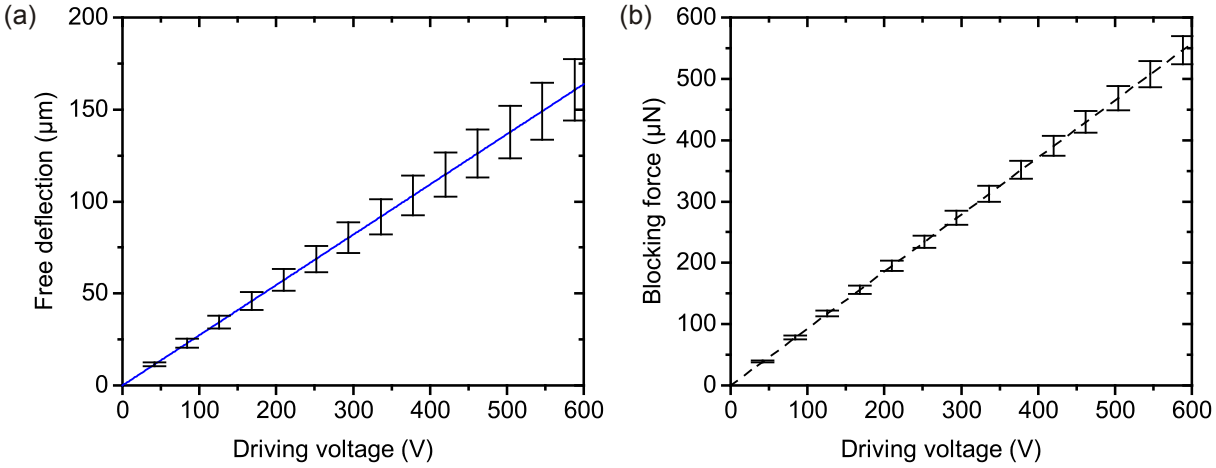

Figure 3.4 Modeled free deflection (a) and blocking force (b) of 15 mm long cantilever actuators. Error bars indicate the expected influence of tolerances in P(VDF-TrFE) film thickness (± 2 µm) and cantilever length (± 0.5 mm).

3.3 Modeling of membrane actuators

The deflection of membrane actuators was modeled using an analytical description by Zhang et al. [158]. A schematic view of a circular membrane with a membrane radius R_p and a radius of the P(VDF-TrFE) layer R_{act} is displayed in Figure 3.5. Similar to the model for cantilever actuators, a two-layer setup of one passive and one active layer was employed.

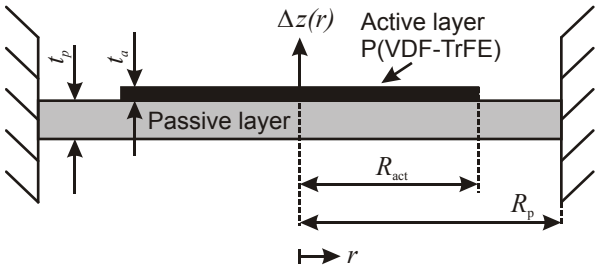

Figure 3.5 Geometry conventions used for modeling of membrane actuators.

The free membrane deflection $\Delta z(r)$ perpendicular to its surface is given by [158]:

$$\Delta z_1(r) = \frac{M_0\left[(R_p^2 - R_{act}^2)(R_{act}^2 - r^2) + R_{act}^2\left(R_{act}^2 - 2R_p^2 \ln\frac{R_{act}}{R_p} - R_p^2\right)\right]}{2\{D_p[(1+\nu_p)R_{act}^2 + (1-\nu_p)R_p^2] + D_e(1+\nu_e)(R_p^2 - R_{act}^2)\}} \quad (0 \le r \le R_{act}), \tag{3.10}$$

$$\Delta z_2(r) = \frac{M_0 R_{act}^2\left(r^2 - 2R_p^2 \ln\frac{r}{R_p} - R_p^2\right)}{2\{D_p[(1+\nu_p)R_{act}^2 + (1-\nu_p)R_p^2] + D_e(1+\nu_e)(R_p^2 - R_{act}^2)\}} \quad (R_{act} \le r \le R_p).$$

M_0 describes the moment caused by piezoelectric actuation and is given by

$$M_0 = D_e \frac{-d_{31} E}{\frac{t_a + t_p}{2} + \frac{2}{t_a + t_p}\left(\frac{1}{Y_a t_a} + \frac{1}{Y_p t_p}\right)(D_a + D_p)}. \tag{3.11}$$

The additional subscript e describes the equivalent properties of the two-layer setup. The flexural modulus D is defined as

$$D_p = \frac{Y_p t_p^3}{12(1-\nu_p^2)} \quad \text{and} \quad D_a = \frac{Y_a t_a^3}{12(1-\nu_a^2)}. \tag{3.12}$$

Free membrane deflection and blocking force F_{Block} are related by the following expression [159]:

$$F_{Block} = \Delta z_1(r=0)\frac{16\pi D_e}{R_p^2}. \tag{3.13}$$

Figure 3.6 plots the normalized membrane deflection for different relative radii of the piezoelectric layer R_{act}/R_p. For a relative radius of 0.6, maximum membrane deflection is obtained, which corresponds to maximum volume change for the target application in a micropump. Using this diameter ratio, a P(VDF-TrFE) film thickness of 10 µm and a driving voltage of 400 V, deflection and force have been modeled for different membrane radii (see Figure 3.7).

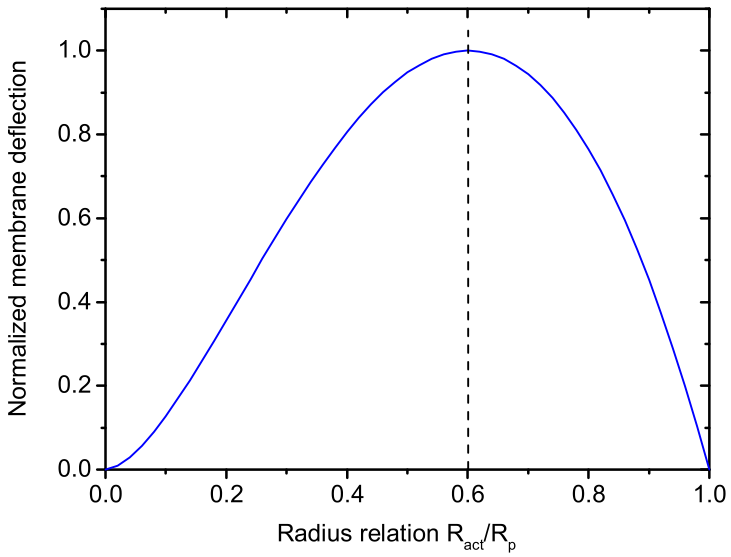

Figure 3.6 Modeled normalized free deflection of a membrane actuator depending on the radius R_{act} of the P(VDF-TrFE) film normalized to the membrane radius R_p.

An increase in free membrane deflection which is proportional to the square of the membrane radius R_p^2 is obtained. For membrane radii of 5 mm and 10 mm, free deflections of 1.8 µm and 7.4 µm are expected, respectively. As stated in equation (3.13), the blocking force is proportional to the free deflection multiplied by R_p^{-2}. Therefore, the blocking force is independent of membrane radius for fixed driving voltage and layer thickness. A blocking force of approximately 1800 µN was derived.

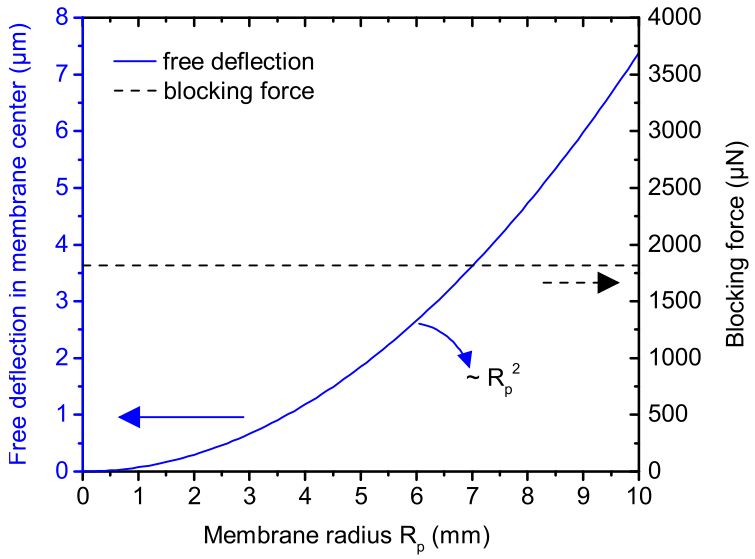

Figure 3.7 Modeled free deflection and blocking force of membrane actuators depending on membrane radius. (Fixed parameters: P(VDF-TrFE) thickness 10 µm, driving voltage 400 V.)

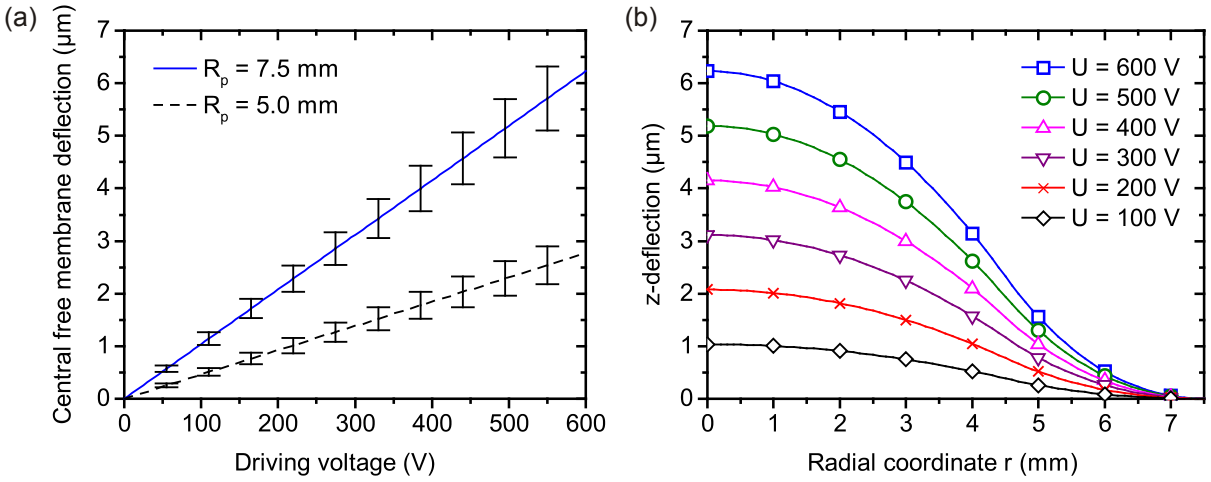

Figure 3.8 (a) Modeled voltage-dependent free deflection of membrane actuators. Error bars indicate expected influence of tolerances in membrane radius and thickness of the piezoelectric layer. (b) Modeled surface profile of a 7.5 mm-radius actuator under different driving voltages.

Figure 3.8 (a) displays the influence of geometry variations on free membrane deflection. With assumed manufacturing tolerances in membrane radius of ± 250 µm and in P(VDF-TrFE) thickness of ± 2 µm, deviations in deflection in the range of 10% can be expected. The modeled membrane deflection with respect to the radial coordinate *r* is plotted in Figure 3.8 (b) for different driving conditions. These shapes provide a basis for comparison with deflected shapes measured on actual samples in this work.

3.4 Modeling of pump behavior

In order to provide a basic model of the pump demonstrator in this work, estimates of the pump behavior are given in this section. It has to be noted that this model does not provide a comprehensive description of the fluidic interdependencies in a reciprocating micropump, but gives a basis for evaluating the demonstrator performance. The volume change ΔV under the deflected membrane for one driving cycle is derived by integrating equation (3.10) over the radius *r*:

$$\Delta V = 2\pi \int_0^{R_p} \Delta z(r)\, r\, dr. \tag{3.14}$$

For cyclic driving of the membrane in pumping applications, the liquid flow rate Q_l can then be estimated by multiplying the volume change by driving frequency f and an overall efficiency factor η for transforming the volume change in air to a liquid pump rate:

$$Q_l = \Delta V\ f\ \eta. \tag{3.15}$$

For quasi-static driving conditions, η accounts for a valve direction sensitivity (η_{valve}). For dynamic driving, it furthermore considers a reduced deflection ($\eta_{\Delta z}$) and a reduction of resonance frequency due to fluid damping (η_f). As a first-order approximation, values of $\eta_{\text{valve}} = 0.2$ [14], $\eta_{\Delta z} = 0.2$ [160] and $\eta_f = 0.25$ [123] were adopted from literature, leading to an overall efficiency under dynamic driving conditions of

$$\eta = \eta_{\Delta z}\ \eta_f\ \eta_{valve} = 0.01. \tag{3.16}$$

Figure 3.9 plots the volume change per stroke of membrane actuators as well as the estimated quasi-static pump rates for membrane pumps with P(VDF-TrFE) actuators.

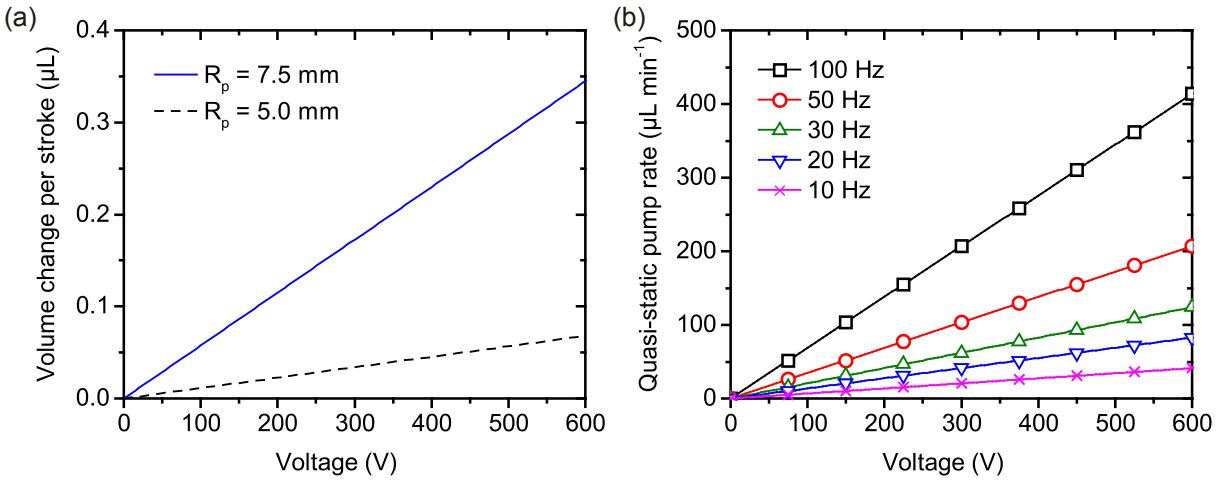

Figure 3.9 (a) Modeled volume change per stroke for membrane actuators. (b) Estimated pump rate for membrane actuators (R_p = 7.5 mm) under quasi-static large-signal driving with different driving frequencies.

For membrane radii of 5 mm and 7.5 mm, volume changes for one actuation stroke of up to 0.07 µL and 0.34 µL were modeled, respectively. For a membrane radius of 7.5 mm, this leads to estimated pump rates of approximately 41 µL min^{-1} to 410 µL min^{-1} for large-signal quasi-static driving (U = 600 V) with frequencies between 10 Hz and 100 Hz. Under quasi-static driving conditions, a pumping cycle is long enough to allow relaxation of all pressure and flow transients generated by valve function, which results in a linear relationship between driving frequency and pump rate [123]. Above a corner frequency that depends on the individual micropump design, insufficient relaxation, energy loss e.g. due to squeeze film damping and other secondary effects lead to lower pump rates [123]. This transition from quasi-static to dynamic behavior is not included in this basic model, but will be briefly discussed during characterization of actual pump demonstrators.

The quasi-static pump rates estimated in this section will be used as a basis for comparing with pump rates measured in an actual pump demonstrator (see chapter 7). An estimation of the dynamic pump rate is provided in section 6.3.3 along with the dynamic actuator characterization.

4 Manufacturing of all inkjet printed P(VDF-TrFE) actuators

This chapter introduces a novel manufacturing process for all inkjet printed P(VDF-TrFE) actuators. The process developed in this work represents the first realization of all inkjet printed P(VDF-TrFE) actuators. The actuators consist of a three-layer setup of two electrodes and an intermediate P(VDF-TrFE) film on top of a passive polymer substrate. The process adjustment for printing and post-treatment of each layer is discussed. For the P(VDF-TrFE) film, the preparation of the printing solution is described, whereas commercially available silver nanoparticle dispersions were used for the electrodes. Aspects of low-temperature post-treatment steps, especially sintering steps for the silver electrodes, are covered. In total, a process chain that consists of three printing and three post-treatment steps is established that is compatible with temperature-sensitive polymer substrates.

4.1 Basic process chain

When using inkjet printing, several process steps are necessary for each printed layer, which is illustrated in Figure 4.1. First, a CAD (computer-aided design) model of the desired structures is generated. Prior to actual printing, an appropriate surface activation step is required to control the wetting conditions, which can be often realized by cleaning with a solvent or plasma activation. The structures are then printed and afterwards functionalized, typically by sintering or tempering. When printing multilayer devices, several iterations of these steps are performed. In this work, a suitable ink was identified for each layer with respect to compatibility of the inks and the required post-treatment steps with the substrate and the previously printed layers. The parameters of surface activation, the printing process itself as well as the post-treatment were adapted for each printed layer, which is covered in more detail in the following sections.

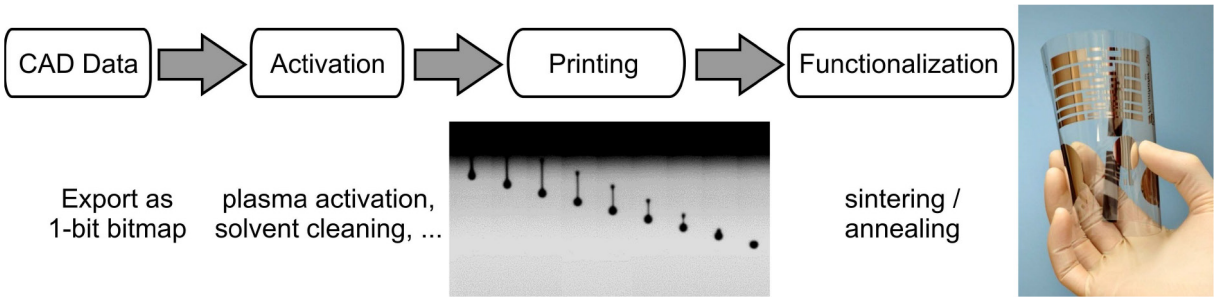

Figure 4.1 Process steps required for each printed layer.

Figure 4.2 shows an overview of the basic process flow that was employed to manufacture all inkjet printed actuators. Biaxially oriented poly(ethylene terephthalate) films (PET, 125 µm thickness, Goodfellow GmbH, Germany) were used as substrates. On top of the substrates, a bottom electrode layer was printed using a commercially available silver nanoparticle dispersion (NPS-JL, Harima Chemicals, Inc., Japan) (a). The as printed-layers were then dried thermally and sintered using a low-pressure argon plasma exposure to generate electrically conductive electrodes. On top of the bottom electrodes, an approximately 9 µm thick P(VDF-TrFE) film was inkjet printed (b). After printing, the film was annealed in order to evaporate remaining solvents from the film and to generate a sufficient degree of crystallinity of the ferroelectric β-phase of P(VDF-TrFE). On top of the piezoelectric film, a top electrode was then printed using a commercially available silver nanoparticle dispersion (CCI-300, Cabot Corp., USA) (c). The electrodes were dried and sintered using the same recipe that was employed for the bottom electrodes.

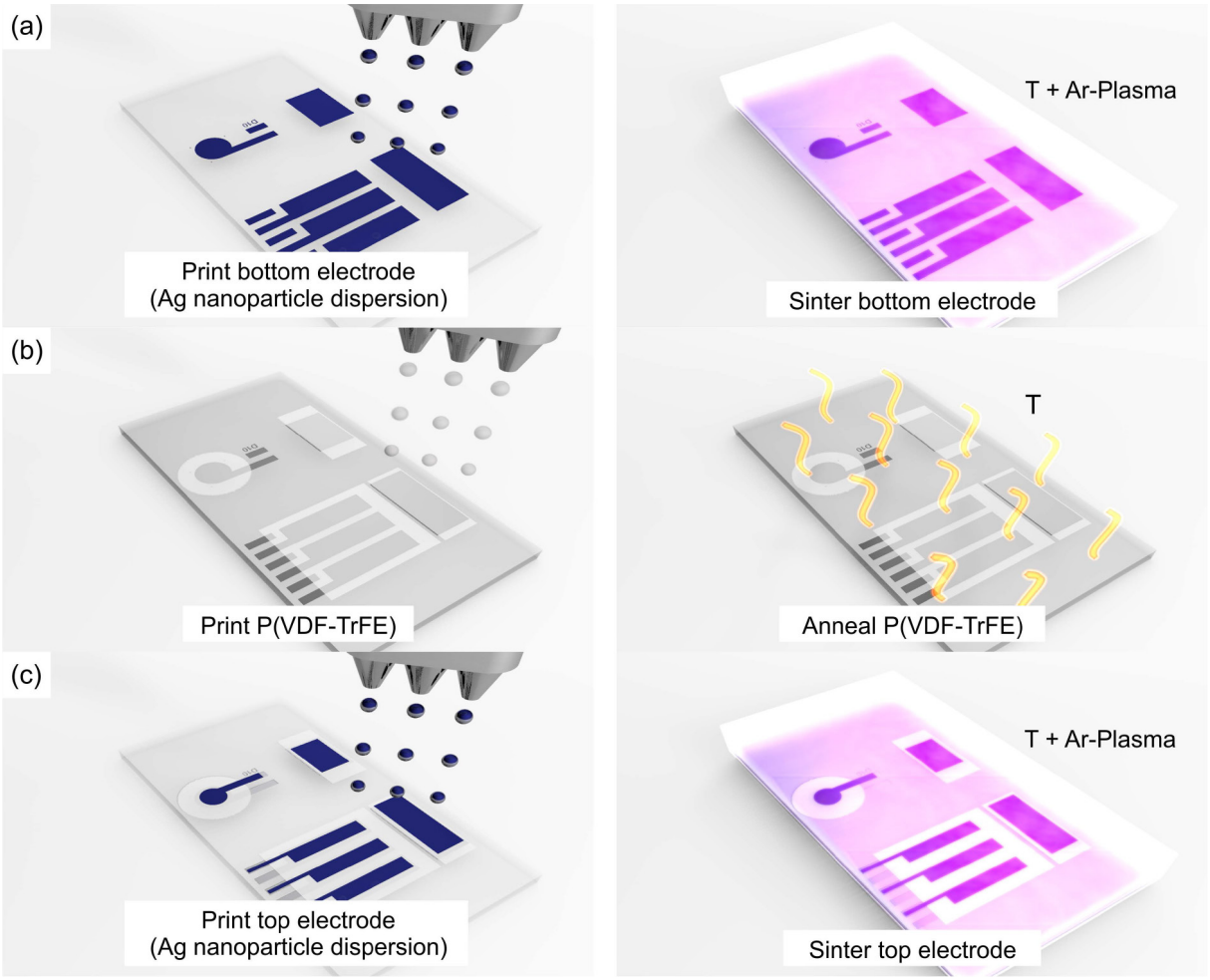

Figure 4.2 Process flow for manufacturing all inkjet printed piezoelectric polymer actuators. Electrodes and piezoelectric P(VDF-TrFE) layers are printed and sintered or annealed subsequently.

4.2 Inkjet printing equipment

All active layers that are required for building up the actuators were deposited using drop-on-demand inkjet equipment. Piezoelectric printheads from Fujifilm Dimatix, Inc. (USA) were used in two different deposition setups. Figure 4.3 shows a compact deposition system that was employed for printing the electrode layers. It is a commercial printing setup (Omnijet 100, Unijet Co., Ltd., South Korea) and includes a two-axis positioning stage, driving hardware for the actual printheads and several cameras for sample and printhead alignment as well as a stroboscopic droplet visualization setup. 1-bit bitmap images can be printed from the printer software. The machine is equipped with driving hardware for single-use printing cartridges with 16 square nozzles with an edge length of 22 µm, a nozzle spacing of 254 µm and a nominal droplet volume of 10 pL (DMC-11610, Fujifilm Dimatix, Inc., USA). The single-use cartridges feature an on-head ink reservoir with a volume of approximately 1.5 mL. Typically they were filled with 1 mL of fluid. Due to the small dead volume, they are suitable especially for academic purposes, ink development or for printing expensive inks like precious metal inks. The positioning stage has a nominal positioning accuracy of ± 5 µm. In order to avoid dust particles on the substrates or the wet printed films, the printer is placed in a laminar flow environment (BMF Reinraumtechnik GmbH, Germany).

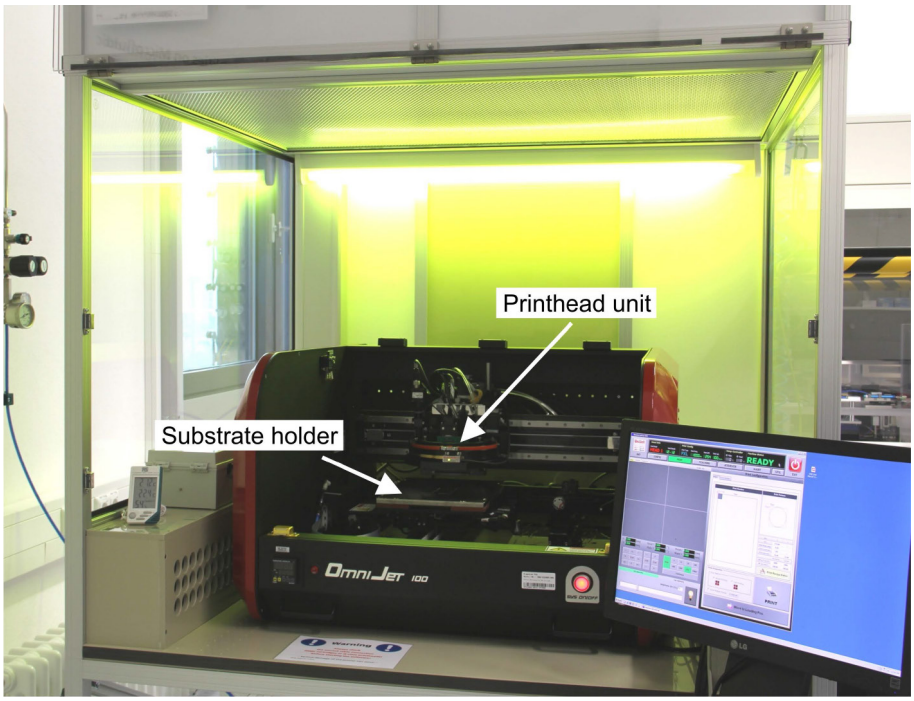

Figure 4.3 Compact drop-on-demand inkjet deposition system (Unijet Co., Ltd.).

For printing the P(VDF-TrFE) solution, a second printing setup was employed. A photograph of the setup is displayed in Figure 4.4. As a positioning system, a six-axis robot with a positioning accuracy of approximately 20 µm and a working range of 650 mm is used (KR 5, Kuka Roboter GmbH, Germany). The robot is mounted on the frame of a granite table. The granite plate itself carries the substrate holder and is equipped with an air suspension. On the tool holder of the robot, a piezoelectric printhead with 256 nozzles and a nominal droplet volume of 80 pL was mounted (Nova 256/80, Fujifilm Dimatix Inc., USA). The printhead is designed for industrial multi-use and exhibits a nozzle spacing of 279 µm. The control of the printhead is realized via a Dimatix Apollo II printhead support kit. The whole setup consisting of the robot and the printhead support kit is controlled by LabVIEW based software. A temperature-controlled on-head ink reservoir with a volume of approximately 25 mL is mounted next to the printhead (b) and can be automatically refilled with a peristaltic pump unit (c).

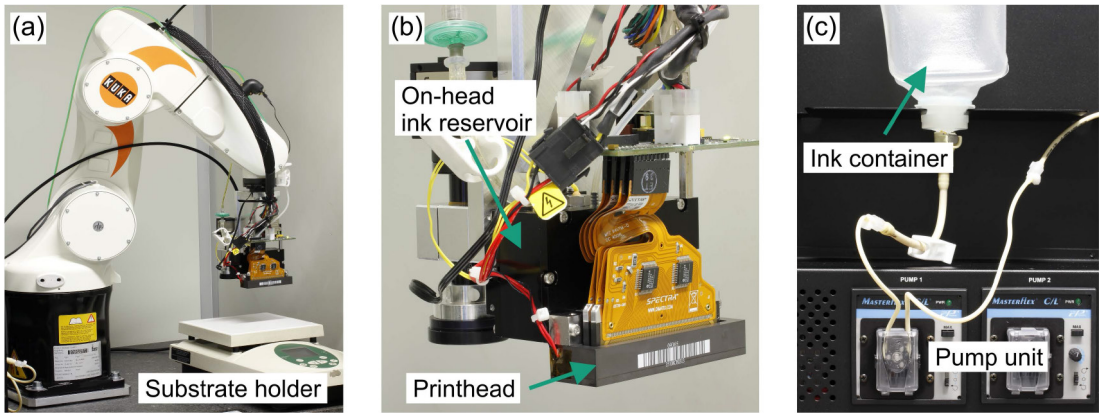

Figure 4.4 (a) Custom drop-on-demand inkjet deposition system consisting of industrial inkjet printheads (Fujifilm Dimatix Inc., USA) and a six-axis robot as a positioning tool (Kuka Roboter GmbH, Germany). Detailed view of printhead (b) and automatic refill unit (c).

When printing laterally large and / or thick layers, it is desired to use as many nozzles on the printhead as possible in order to speed up processing. For a proper function of many nozzles, it is necessary to purge a relatively large volume of fluid through the nozzles and wipe the nozzle plate. With this cleaning procedure, air bubbles are removed from the channels, the nozzles are wetted and residuals of dried ink are removed from the nozzle plate. For well-working nozzles, it was typically necessary to fill the ink container with a volume of approximately 100 mL. With relatively inexpensive polymers like P(VDF-TrFE), it is feasible to use such large amounts of ink also under research conditions. Furthermore, the ink that is expelled from the printhead during purging can be filtered and re-used.

4.3 Printing of three-layer actuator structure

Using the two printing setups described above, the actuator layer structure consisting of two electrodes and a piezoelectric P(VDF-TrFE) film was manufactured. The PET substrates were purchased from Goodfellow GmbH, Germany. The upper working temperature of the substrates recommended by the manufacturer is approximately 140 °C [154]. PET was chosen because it is a widely used low-cost substrate material in printed electronics [1] and offers good thermal stability compared to other typical polymer substrates like PMMA (poly(methyl methacrylate), $T_G \approx 105$ °C) or PC (polycarbonate, $T_G \approx 135$ °C). On top of the PET substrates, the electrodes and the P(VDF-TrFE) film were printed consecutively.

4.3.1 Bottom electrode layer

Bottom electrodes were printed using a commercially available silver nanoparticle dispersion in tetradecane with a solid content of 55 wt% and an average particle diameter of 7 nm (NPS-JL, Harima Chemicals, Inc., Japan) [161]. Prior to printing, the PET substrates were washed with isopropanol to remove dust and residuals of the protective foil with which the substrates were delivered. Reproducible wetting with the Harima silver dispersion was achieved when the substrates were wiped with xylene prior to printing. The nanoparticle dispersions were printed using the Unijet printing setup equipped with disposable Dimatix DMC cartridges with a nominal droplet volume of 10 pL (see Figure 4.3). With driving voltages between 35 V and 40 V, a printing frequency of 2 kHz and a fire pulse width of 10 µs, controllable droplet formation was achieved for all 16 nozzles of the printhead. The bottom electrodes were printed using a droplet spacing of 60 µm. With these parameters, printing of the bottom electrode layer took approximately 10 minutes for a typical layout (10 circular actuators with 15 mm diameter).

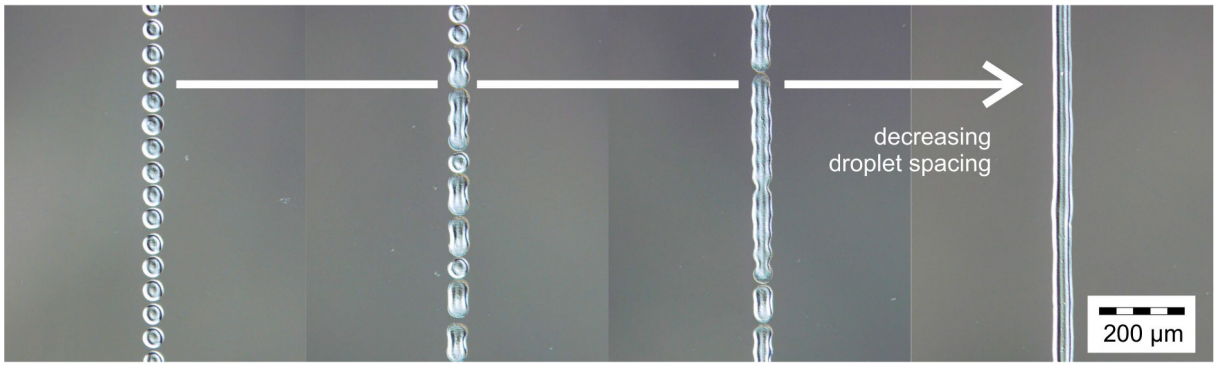

Figure 4.5 Influence of droplet spacing on line morphology for printed silver nanoparticle dispersions.

Figure 4.5 shows silver lines that were printed with different droplet spacings. Depending on the wetting conditions, the droplet spacing needs to be optimized to generate smooth and continuous printed lines or layers.

For sintering the as-printed electrodes, consecutive thermal and low-pressure argon plasma treatments were employed. First, the electrodes were dried in a convection oven (Heraeus UT 20P, Thermo Fisher Scientific Inc., USA) for 60 min at a temperature of 100 °C. After this drying step a resistivity of approximately 80 μΩ cm was achieved, which corresponds to 50 times the resistivity of bulk silver. The resistivity was determined from at least five printed lines by cross-section and two-point resistance measurements.

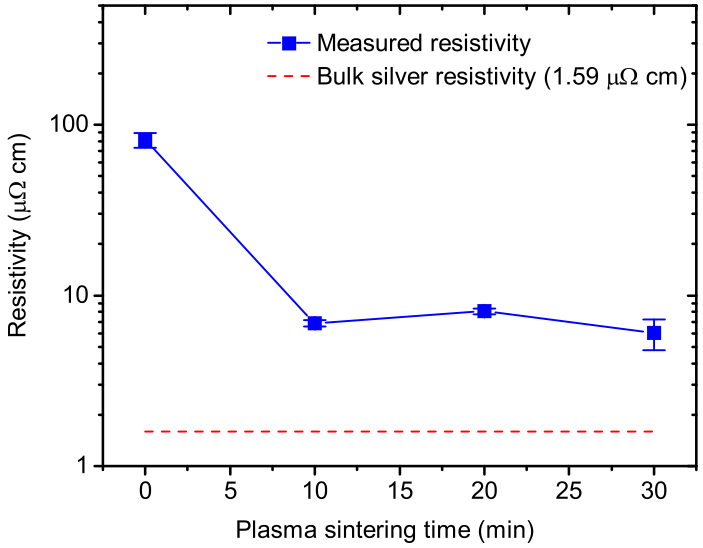

Figure 4.6 Resistivity of plasma-sintered silver nanoparticle dispersions used for bottom electrodes.

In order to increase the conductivity, the samples were afterwards sintered using a low-pressure argon plasma exposure. The plasma treatment was run in a plasma chamber equipped with a 50 kHz RF (radio frequency) generator (V55-GKM, Plasma Finish GmbH / Pink GmbH, Germany) using an RF power of 240 W. The duration of the plasma treatment was varied between 10 min and 30 min. The resulting resistivity values are plotted in Figure 4.6. Already after a short plasma treatment of 10 min, the resistivity drops to approximately four times the bulk silver resistivity, which is a typical value for printed silver nanoparticle dispersions [16]. With longer durations of the plasma treatment, the resistivity decreases slightly further, but remains in the same order of magnitude. Without the argon plasma treatment, temperatures well above 150 °C would be necessary to generate comparable conductivities [16], which would limit the compatibility with temperature-sensitive polymer substrates. During the low-pressure argon plasma treatment, the global temperatures remain moderate. Directly after the plasma treatment, the temperature of the

substrate holder in the plasma chamber was measured to be below 70 °C by a contact-type resistive temperature sensor, which agrees with literature values for this sintering technique [162]. The sintering approach is therefore suitable for temperature-sensitive polymer substrates. For processing actuator bottom electrodes, the duration of the plasma treatment was set to 30 min to ensure thorough sintering. A photograph of printed and sintered silver bottom electrodes is depicted in Figure 4.7. The resistance measured across the bottom electrodes was in the range of few Ohm (Ω), while the thickness of the bottom electrodes was measured by white light interferometry to be approximately 500 nm.

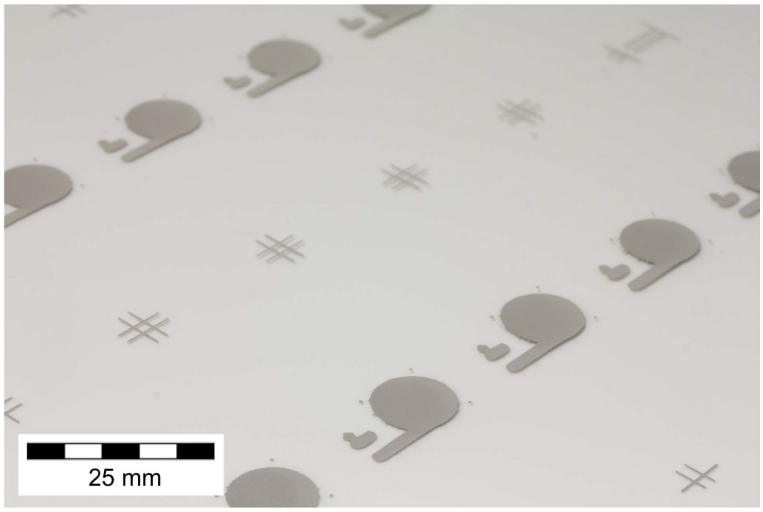

Figure 4.7 Bottom electrode layer of membrane actuators printed from a silver nanoparticle dispersion.

4.3.2 P(VDF-TrFE) layer

On top of the printed and sintered bottom electrodes, a P(VDF-TrFE) film was printed. From analytical modeling discussed in chapter 3, a target thickness of 10 µm was identified as a trade-off between relatively large actuator deflection and tolerable driving voltages. Such film thicknesses can be generated by printing multiple layers on top of each other. In order to keep the processing time in a reasonable range, the robot-based printing setup equipped with a printhead with 256 nozzles and a nominal droplet volume of 80 pL was used (see Figure 4.4).

P(VDF-TrFE) powder with a VDF:TrFE ratio of 70:30 wt% was dissolved in cyclopentanone. The powder was purchased from Solvay Specialty Polymers Italy S.p.A., while cyclopentanone (boiling point 131 °C) was purchased from VWR International GmbH. Different concentrations of the P(VDF-TrFE) solution were prepared and the viscosity of the solutions was measured using a rolling ball viscosimeter (AMVn / DMA4100, Anton Paar GmbH, Austria). A logarithmic plot of the viscosity with respect to different polymer contents is displayed in Figure 4.8.

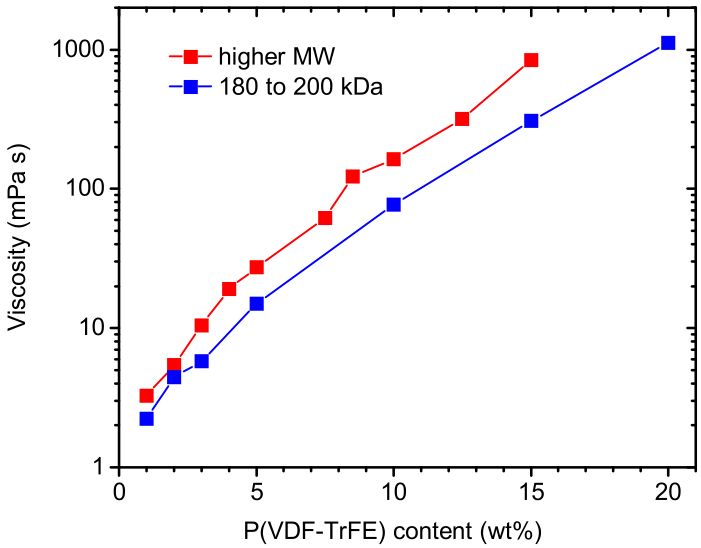

Figure 4.8 Viscosity of P(VDF-TrFE) solutions in cyclopentanone for different solid contents (logarithmic plot).

An exponential increase of viscosity with polymer content was observed with viscosities in the range of 2 mPa s to >1000 mPa s for polymer contents between 1 wt% and 20 wt%. Good printability with the 80 pL printhead (Galaxy 256/80, Dimatix Inc.) was achieved for a concentration of 2 wt% and a molecular weight (MW) of 180 kDa to 200 kDa, which corresponds to a viscosity of 4.5 ± 0.4 mPa s. Higher viscosities of more than 1000 mPa s would be appropriate when using screen printing as an alternative deposition technique [24,163]. When using higher molecular weight P(VDF-TrFE) powder, lower solid contents are required for inkjet printable solutions. Due to the relatively high target thickness of 10 µm, this is undesired.

The fire pulse of the printhead was set to a voltage amplitude of 150 V and a width of 16 µs. Printing was performed using printing frequencies between 800 Hz and 1000 Hz. Prior to the first printing run, the printhead was purged thoroughly using approximately 20 mL of the P(VDF-TrFE) solution. With this preparation, all nozzles of the printhead could be used. However, regular purging was necessary to keep the nozzles running and to remove residuals of dried ink from the nozzle plate. Purging was performed typically in an interval of 5 min with a purged volume of approximately 5 mL. The purged ink was filtered and re-used.

During printing, dot spacing was set to 70 µm in the moving direction of the robot (x-direction), while in the direction normal to the robot movement (y-direction), the intrinsic nozzle spacing of the printhead of 279 µm defined the droplet spacing. This lead to line-like structures of the printed P(VDF-TrFE). For generating a film thickness of approximately 9 µm, 100 layers were printed on top of each other. Uncontrollable drying effects were avoided by heating the substrate holder to temperatures between 40 °C and 80 °C depending

on the moving speed of the robot. This heating lead to drying of the layers before the next layer was printed. With this approach, line-like morphologies and functioning actuators were fabricated without the need for time-consuming drying and re-alignment steps when printing and drying each layer separately. With the as-described printing procedure, printing of the piezoelectric layer took approximately 30 minutes for a typical actuator layout (10 circular actuators with 15 mm diameter).

As discussed in chapter 1, a post-treatment of the printed P(VDF-TrFE) is necessary to remove solvents from the film and to set a sufficient degree of crystallinity of the piezoelectric β-phase. Based on literature values, elevated temperatures of typically up to 130 °C are required for this annealing step [119]. In this work, annealing of the as-printed P(VDF-TrFE) films was performed in a convection oven for 24 hours. The basic annealing profile is displayed in Figure 4.9.

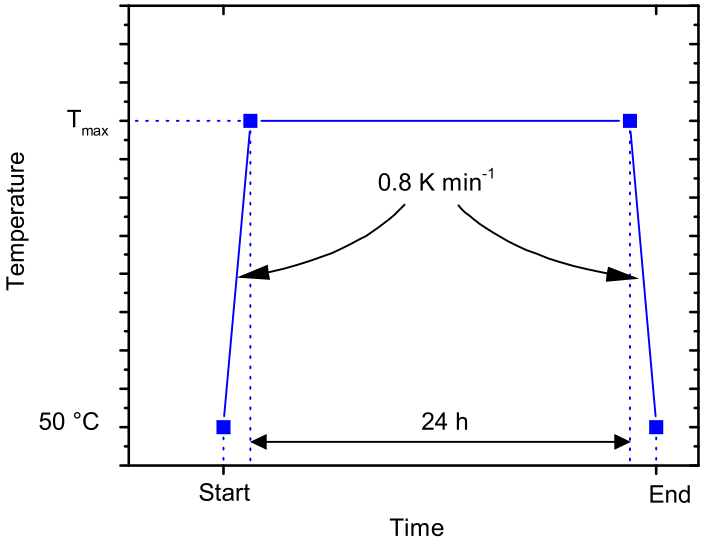

Figure 4.9 Basic temperature profile employed for annealing the as-printed P(VDF-TrFE) films.

The samples were placed in the oven that was pre-heated to a temperature of 50 °C, which is well below the temperature of the ferroelectric-paraelectric phase transition in P(VDF-TrFE) [116]. A defined temperature gradient of 0.8 K min^{-1} was then applied to heat the samples to the maximum tempering temperature T_{max}. In this work, different maximum temperatures were investigated to study the effect of annealing on the morphology of the P(VDF-TrFE) films and actuator performance. These influences are discussed in more detail in chapter 5. The samples were kept at T_{max} for 24 hours. This long duration was chosen in order to minimize the amount of remaining solvents in the P(VDF-TrFE) films and to clearly separate the effects of annealing temperature from time-dependent influences. After 24 hours, the samples were cooled down to 50 °C again with a temperature gradient of 0.8 K min^{-1}. A

photograph of printed and annealed P(VDF-TrFE) films on top of printed silver bottom electrodes for membrane actuators is displayed in Figure 4.10.

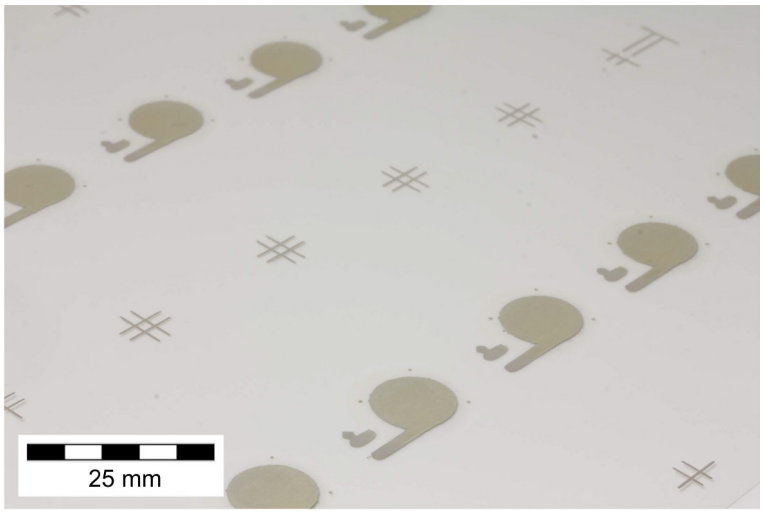

Figure 4.10 Bottom electrode and piezoelectric layers of membrane actuators.

4.3.3 Top electrode layer

Finally, top electrodes were inkjet printed on top of the previously printed bottom electrode and P(VDF-TrFE) film. In order to ensure good wetting, the surface energy of the P(VDF-TrFE) film was increased by a low-pressure argon plasma activation. With this activation, good wetting was achieved when printing a commercial silver nanoparticle dispersion in a mixture of ethanol and ethylene glycol (CCI-300, Cabot Corp., USA). The particle diameter in the silver nanoparticle dispersion ranges from 30 nm to 50 nm and the silver content is 20 wt%. Figure 4.11 shows examples of as-printed silver nanoparticle dispersion on non-treated and plasma-activated printed P(VDF-TrFE) films. Without plasma activation (a), continuous films could not be generated, whereas the activated films lead to defined wetting of the silver nanoparticle dispersions (b).

In order to keep ink consumption low, the same compact inkjet deposition system with disposable cartridges was used as for printing the bottom electrodes. Stable droplet formation was achieved for all 16 nozzles with a fire pulse amplitude of 35 V, a pulse width of 5 µs and a printing frequency of 2 kHz. Continuous top electrodes were achieved with a droplet spacing of 20 µm.

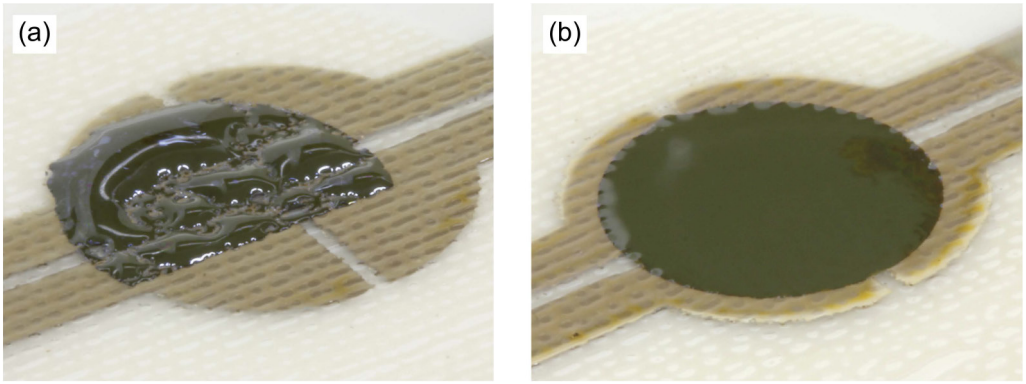

Figure 4.11 Effect of plasma activation on wetting properties. Non-activated P(VDF-TrFE) film with printed silver nanoparticle dispersion (a). Wetting behavior on plasma-activated P(VDF-TrFE) film (b).

Due to the different wetting properties compared to printing the bottom electrodes, the top electrodes are thicker than the bottom electrodes. The thickness was measured to be approximately 1.8 µm by scanning electron microscopy (SEM) of the actuator cross-section, whereas 0.5 µm were measured for the bottom electrodes. Printing of top electrodes for a typical sample with 10 membrane actuators took approximately 10 min. Sintering of the top electrodes was performed using the same combined thermal and argon plasma treatment that was employed for sintering bottom electrodes. The dependence of resistivity on the duration of the plasma treatment is displayed in Figure 4.12.

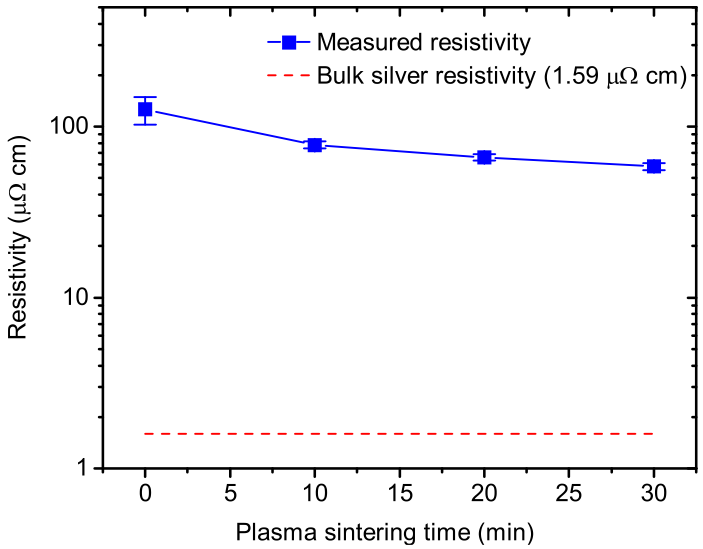

Figure 4.12 Resistivity of plasma-sintered silver nanoparticle dispersions used for top electrodes.

After a one-hour thermal treatment at 100 °C, the printed top electrodes exhibit a resistivity of approximately 40 times bulk silver resistivity. With a low-pressure argon plasma treatment, the resistivity is reduced to approximately 20 times the bulk silver value. Due to the different solvent composition and particle size in the ink (30 nm to 50 nm instead of 7 nm), the resistivity is higher than observed for the bottom electrodes. However, the overall

resistance measured across actuator top electrodes remained low (< 10 Ω). Higher conductivities would require higher temperatures or longer sintering times, which would be undesired as it might influence the properties of the underlying P(VDF-TrFE) film. Therefore, the sintering regime was not modified further in order to keep the processing temperatures as low as possible.

4.4 Processing summary

Figure 4.13 shows fully-processed P(VDF-TrFE) membrane actuators, which were afterwards separated by cutting and mounted for actuator characterization. Figure 4.14 shows an SEM cross-sectional view of the layer setup. A thickness of the P(VDF-TrFE) film of approximately 9 µm was measured, which agrees with the target thickness. As discussed previously, different thicknesses were measured for the bottom (≈ 0.5 µm) and top electrodes (≈ 1.8 µm) due to different wetting conditions.

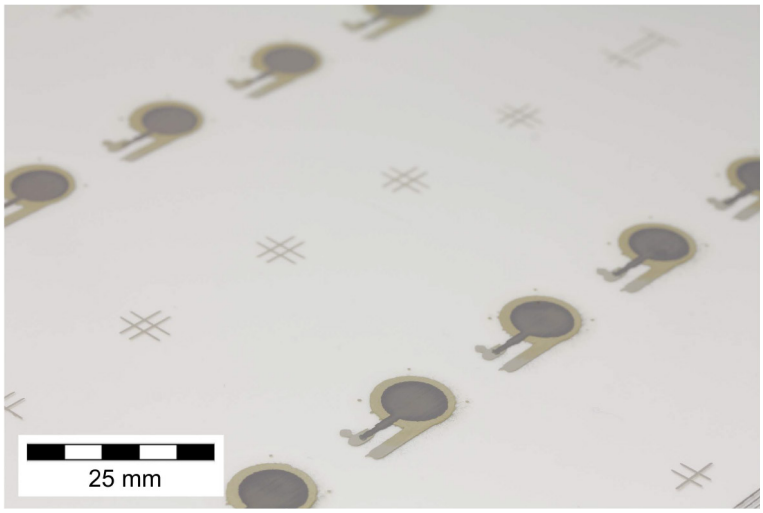

Figure 4.13 Fully processed membrane actuators with two silver electrodes and a piezoelectric film in between.

In summary, this chapter described a novel manufacturing approach for piezoelectric actuators based on P(VDF-TrFE). All active layers were applied using drop-on-demand inkjet printing. Electrodes were printed using two different commercial silver nanoparticle dispersions, while the P(VDF-TrFE) films were printed from solutions. After printing each layer, a thermal or combined thermal and plasma treatment was employed to remove the solvents, sinter the metal nanoparticles or increase the crystallinity of the P(VDF-TrFE) film. Particular attention was paid to compatibility of the post-treatment steps with temperature-sensitive polymer substrates. A summary of the process parameters that were used is displayed in Table 4.1

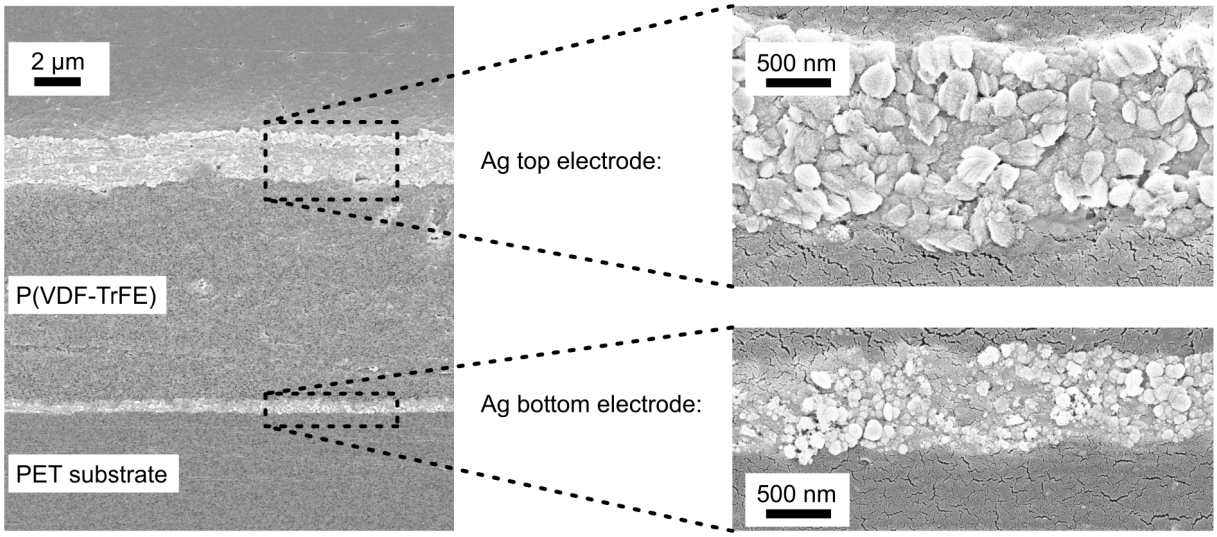

Figure 4.14 Cross-sectional SEM image of layer sandwich with close-up views of the silver bottom and top electrodes.

Table 4.1 Overview of process parameters for manufacturing all inkjet printed P(VDF-TrFE) actuators.

	Type of ink and printhead	Pre-treatment	Printing parameters	Post-treatment
Bottom electrode 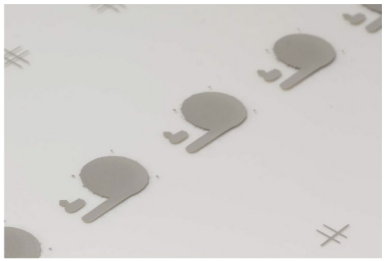	Silver nanoparticle dispersion in tetradecane (NPS-JL, Harima Chemicals, Inc., Japan) Dimatix DMC cartridge droplet volume 10 pL	washing in isopropanol wiping with xylene	droplet spacing 60 µm 2 kHz printing frequency 16 nozzles active 1 layer printing time for 10 membrane actuators ≈ 10 min	Drying in convection oven 60 min @ 100 °C low-pressure argon plasma sintering (50 kHz generator @ 240 W, 30 min)
Piezoelectric layer 	P(VDF-TrFE) solution in cyclopentanone VDF:TrFE ratio 70:30 wt% solid content 2 wt% Dimatix Nova 256/80 printhead droplet volume 80 pL		droplet spacing 70 µm / 279 µm (x/y), 0.8 to 1.0 kHz printing frequency up to 256 nozzles active 100 layers printing time for 10 membrane actuators ≈ 20 min	annealing in convection oven, 24 hours @ maximum temperature (typically up to 130 °C)
Top electrode 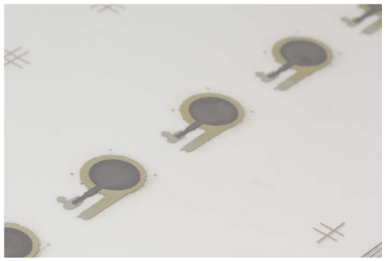	Silver nanoparticle dispersion in ethanol / ethylene glycol (CCI-300, Cabot Corp., USA) Dimatix DMC cartridge droplet volume 10 pL	low-pressure argon plasma activation	droplet spacing 20 µm 2 kHz printing frequency 16 nozzles active 1 layer printing time for 10 membrane actuators ≈ 12 min	Drying in convection oven 60 min @ 100 °C low-pressure argon plasma sintering (50 kHz generator @ 240 W, 30 min)

5 Performance and morphology of inkjet printed actuators

In this chapter, correlations between film morphology and performance of inkjet printed P(VDF-TrFE) actuators are discussed for the first time. The piezoelectric behavior of P(VDF-TrFE) is determined by the presence of ferroelectric β-phase crystals. In order to investigate this influence for the inkjet printed actuators, measurements of the remanent polarization P_{rem} and the piezoelectric d_{31} coefficient are reported. A strong influence of the annealing of the as-printed P(VDF-TrFE) films on the electrical and electromechanical performance is discussed. Furthermore, the structure of P(VDF-TrFE) films that have undergone different thermal treatments is studied by calorimetric and scattering techniques. Relations between the microscopic structure and the device performance are set up, leading to recommendations for process temperatures. The findings discussed here can be employed to design also other future inkjet printed P(VDF-TrFE) devices like pressure sensors [7] or non-volatile memory elements [119].

5.1 Previous work

As discussed in section 2.3, it is well-known that the degree of crystallinity in VDF/TrFE copolymers influences the piezoelectric and ferroelectric properties. Baltá-Calleja et al. reported that “the volume fraction of ferroelectric crystals is directly proportional to the remanent polarization” [17]. For a strong piezoelectric effect and thus a strong electromechanical coupling, a high volume fraction of ferroelectric crystals is desired. Copolymers of VDF and TrFE with a mole fraction of VDF between 12 and 82% are known to exhibit a mixture of the ferroelectric β-phase and the non-polar α-phase at room temperature. The amount of α- and β-phase crystals depends furthermore on the process conditions. For spin-coated P(VDF-TrFE) films cast from solution it has been demonstrated that a thermal treatment of the as-cast films influences the crystallinity of the two phases [17]. Furthermore, correlations between the morphology of spin-coated P(VDF-TrFE) films and ferroelectric properties [18,119] as well as mechanical properties [118] have been set up.

When P(VDF-TrFE) actuators are printed from solutions, as in this work, thermal post-treatments of the as-deposited films are necessary in order to remove solvents and achieve a high degree of crystallinity of the β-phase. At the same time, it has to be assured that the temperature applied does damage the multi-material setup on top of which the P(VDF-TrFE) film is printed. In this work, the underlying layers are a passive PET substrate

and an inkjet printed silver electrode. One limiting factor is the compatibility of the substrate material with the temperatures applied during annealing. For the biaxially oriented PET substrates that were used in this work, the upper working temperature is defined by the manufacturer as approximately 140 °C [154]. When higher temperatures are applied, a softening of the substrate can lead to deformation. This might cause cracks in the setup and result in samples that are easily shortcut or exhibit low breakdown fields.

In order to investigate the behavior of inkjet printed P(VDF-TrFE) films, test samples were prepared and subjected to different temperature profiles when annealing the P(VDF-TrFE) layer. For each temperature profile, measurements of the static deflection of cantilever actuators as well as ferroelectric hysteresis loops were recorded. The piezoelectric d_{31} coefficient and the remanent polarization P_{rem} are extracted and serve as characteristic parameters for the electromechanical and electrical performance, respectively. Furthermore, the morphology of selected samples was studied using differential scanning calorimetry, X-ray diffraction and imaged by atomic force microscopy. Based on these measurements, relations between morphology and actuator performance are set up, leading to recommendations for processing.

5.2 Test structures and preparation

Figure 4.9 shows the basic characteristics of the thermal treatment that was used to anneal the as-printed P(VDF-TrFE) layers. For covering a relatively broad range of temperatures, ten different temperature profiles with maximum temperatures T_{max} ranging from 95 °C to 145 °C were investigated. This range was chosen based on typical temperature regimes taken from literature that were employed for annealing P(VDF-TrFE) [18,118].

For all temperature profiles the influence of a low-pressure argon plasma treatment for sintering the silver top electrode was investigated. For each temperature profile, samples with solely thermally sintered top electrodes as well as samples with top electrodes that were sintered with a combined thermal and argon plasma treatment, as described in section 4.3.1, were investigated. Figure 5.1 shows the test structures that were used to characterize the electrical and electromechanical behavior of printed P(VDF-TrFE) actuators. For ferroelectric hysteresis measurements, square pads with a designed active area of 3 × 3 mm^2 were prepared (a). Deflection measurements were performed on cantilever actuators with an active area of 4 × 15 mm^2 (b). The samples were printed onto PET substrates and the silver bottom and top electrodes were processes as described in chapter 4. After printing the piezoelectric layer with

a thickness of approximately 9 µm, the samples were cut and annealed using different temperature profiles. Afterwards, top electrodes were printed and sintered and the cantilever actuators were mounted on microscopic glass slides (c).

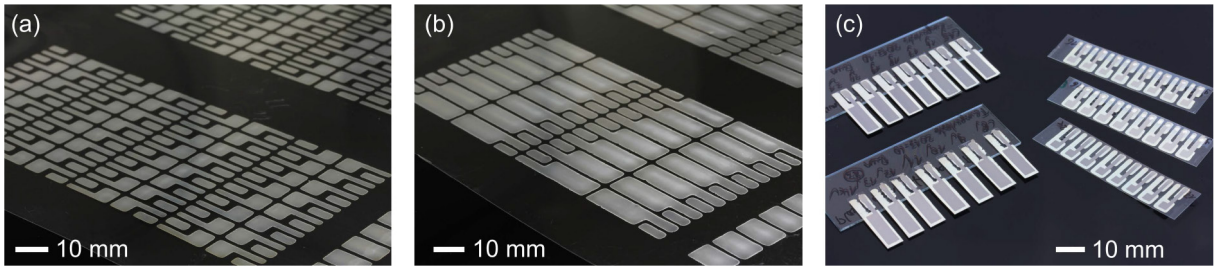

Figure 5.1 Test structures for investigation of the performance of inkjet printed P(VDF-TrFE) actuators. Bottom electrodes for (a) ferroelectric test pads and (b) cantilever actuators. (c) Fully processed samples before characterization.

The dimensions of the samples were designed to be in the order of magnitude of actuators in the targeted micropump application. The pads for ferroelectric measurements were designed with a smaller area to increase the yield of the samples. Major reasons for dielectric breakdown at field strengths below the breakdown strength of bulk P(VDF-TrFE) (approximately 250 V μm^{-1} [105]) of the samples are assumed to be inhomogeneities in film thickness and pinholes in the piezoelectric layer. As the number of pinholes scales with increasing active area, yield and dielectric breakdown strength are higher for smaller active areas.

For reliable DSC measurements, it had to be assured that the printed P(VDF-TrFE) films can be removed from the substrates without removing also the underlying electrode or parts of the substrate, which would lead to additional signals in the DSC thermograms. Therefore, the samples were printed on metalized microscopic glass slides (soda-lime glass, VWR International GmbH, metalized with sputtered Ti/Pt/Au) with a P(VDF-TrFE) thickness of 9 µm and lateral dimensions of approximately 26 × 50 mm^2. A photograph of two samples is provided in Figure 5.2. Using a razor blade it was possible to peel the samples off the substrate while leaving the metalization intact. For morphology investigations, the samples had to be printed without top electrodes. However, to ensure similar process conditions as for actual actuators, the samples were subjected to the heat treatment that was used to sinter the top electrodes. Prior to characterization, the samples were poled electrically using a metalized polypropylene film (PP, Goodfellow GmbH, thickness 8 µm, metalized with aluminum) as a top electrode that was placed on top of the P(VDF-TrFE)-coated area.

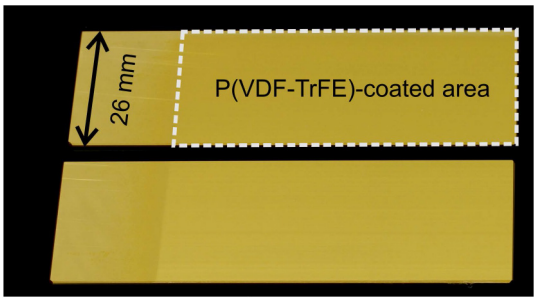

Figure 5.2 Metalized microscopic glass slides with printed P(VDF-TrFE) layer for morphology investigations.

5.3 Electromechanical characterization

The electromechanical behavior of inkjet printed P(VDF-TrFE) actuators was characterized by deflection hysteresis measurements of cantilever bending beams. For the application of actuators, this is the most direct measurement of the device performance and can be described by the piezoelectric coupling coefficient d_{31}. A large d_{31} corresponds to a large expansion or contraction of the P(VDF-TrFE) film which leads to large deflections of a unimorph setup when a given electric field is applied. Figure 5.3 shows the characterization setup that was employed. It is based on a granite table equipped with a substrate holder and an x/y positioning system (LPKF Motion & Control GmbH, Germany).

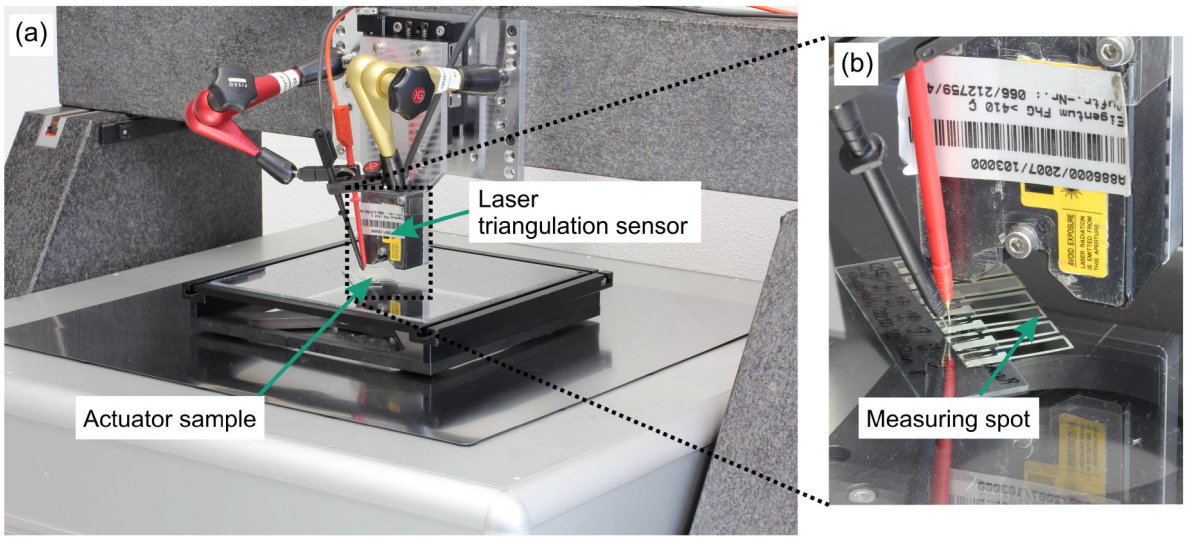

Figure 5.3 Characterization setup used for determining the piezoelectric d_{31} coefficient of cantilever actuator samples (a). Close-up view of one cantilever sample (b).

Defined voltages were applied using a high-voltage amplifier (2220CE, Trek Inc., USA, output voltage range ± 2 kV). The cantilever deflection was measured by a laser triangulation sensor (LK-G10, Keyence Corp., Japan., measurement range ± 1 mm, repeatability 20 nm) mounted above the substrate holder. The setup is controlled via a custom LabVIEW-based interface.

An example of a deflection measurement of a cantilever actuator for voltages up to 600 V is provided in Figure 5.4. This driving voltage corresponds to an electric field of approximately 67 V μm^{-1}. Deflections of the cantilever tip of up to 240 µm were measured. The measurement shows that the printed P(VDF-TrFE) film is capable of operating at such fields.

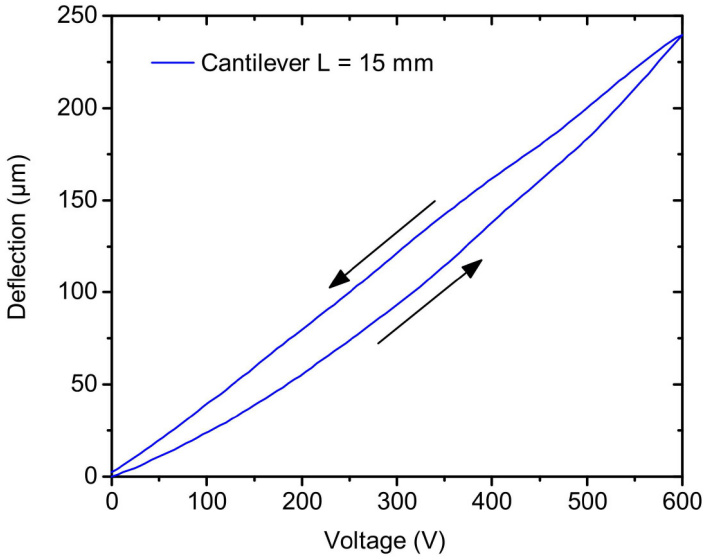

Figure 5.4 Deflection measurement of a 15 mm-long cantilever actuator.

However, due to inhomogeneities and pinholes in the film, the effective dielectric strength was reduced especially for large samples and lead to more frequent dielectric breakdown. Therefore, reduced electric fields were employed during poling and measuring. Prior to measurements, the samples were poled at a DC voltage of 400 V at room temperature for one minute. With a P(VDF-TrFE) thickness of 9 µm, this corresponds to an electric field of approximately 44 V μm^{-1}. Similar fields were applied during deflection hysteresis measurements. With these boundary conditions, more than 90% of the tested samples remained undamaged.

The deflection was recorded while a quasi-static voltage cycle of 0 V – 400 V – 0 V was applied. With the relatively low poling fields, each measurement can in principle increase the poling of the P(VDF-TrFE) films. This influence was investigated by measuring the deflection for 15 consecutive voltage cycles for one sample. Figure 5.5 shows the time-dependent deflection measured for the first three cycles (a) as well as the deflection peaks for all 15 cycles (b). After two to three cycles, only small changes in maximum deflection of approximately 2 µm or 1.2% are visible. Such small deviations cannot be clearly separated from drift effects in the mechanical setup. Therefore, for actual measurements, three voltage cycles were applied and the last cycle was analyzed. The piezoelectric d_{31} coefficient was

extracted from the maximum cantilever displacement at a driving voltage of 400 V by employing the analytical model described in section 3.2 and inserting the geometry of actual printed samples.

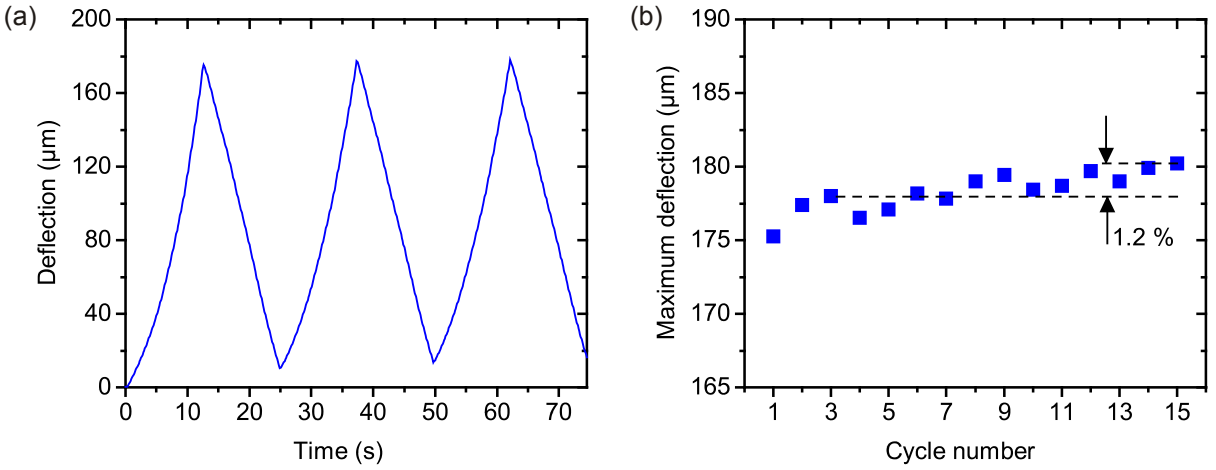

Figure 5.5 Deflection recorded while quasi-static voltage cycles were applied to a cantilever actuator. Time-dependent deflection for the first three cycles (a) and deflection maxima extracted from a measurement of 15 cycles (b). After two to three cycles, only small changes in deflection peaks were observed.

Figure 5.6 shows the d_{31} coefficients that were extracted from the measured maximum cantilever deflection for different temperature profiles and combined thermal and plasma treatments. For each temperature profile, at least five samples were characterized. Depending on the temperature profile, d_{31} coefficients between approximately 0.8 pm V^{-1} and 10 pm V^{-1} were determined. This corresponds to cantilever deflections between approximately 12 µm and 160 µm.

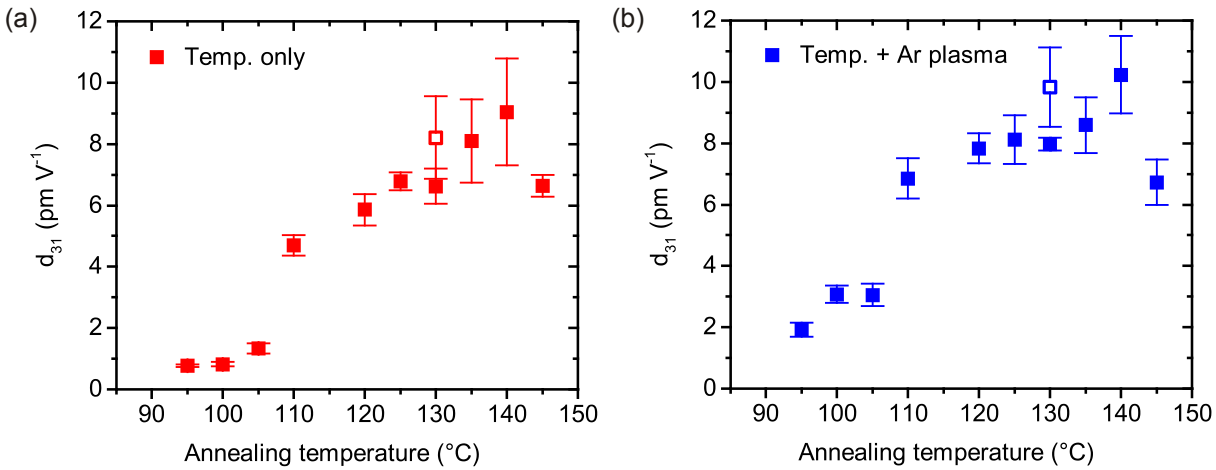

Figure 5.6 Piezoelectric d_{31} coefficient for different thermal (a) and combined thermal and plasma treatments (b) employed for the as-printed P(VDF-TrFE) films. Unfilled marks represent samples for which a reduced cooling rate was employed.

Maximum deflections were observed for the samples annealed at 140 °C. It can be clearly seen that for annealing below 110 °C very low electromechanical coupling with d_{31} coefficients between approximately 0.8 pm V^{-1} and 3 pm V^{-1} occurs. Samples annealed above 110 °C show significantly larger deflections and d_{31} coefficients between 5 pm V^{-1} and 10 pm V^{-1}, which is in the same order of magnitude as typical d_{31} values for P(VDF-TrFE) films found in literature (10 to 12 pm V^{-1}) [104]. Furthermore, it can be seen that the argon plasma sintering leads to an average increase in d_{31} of 1.6 pm V^{-1} compared to samples with solely thermally sintered top electrodes. The plasma treatment thus leads to an additional energy input on the samples, which has an effect on device performance similar to annealing at higher temperatures. The samples annealed at a temperature of 145 °C show lower d_{31} coefficients than those annealed at 140 °C. As 145 °C is slightly above the recommended upper working temperature of the PET substrate, thermally induced deformations in the samples are a possible explanation for the reduced deflection and thus d_{31} values.

Apart from the absolute temperatures, also the heating and cooling rate influences the d_{31} coefficients that were measured. This was not the main point of interest in this study and was therefore investigated only briefly for one exemplary thermal treatment. For a thermal treatment at 130 °C, two different temperature gradients of 0.3 K min^{-1} and 0.8 K min^{-1} were investigated. For all other thermal treatments, gradients of 0.8 K min^{-1} were used. In Figure 5.6, the d_{31} values for reduced gradients are plotted as unfilled squares. In the measurements run in this work, the lower gradients lead to an increase in d_{31} of approximately 1.7 pm V^{-1}.

For all measurements, the standard deviations were in the range of 3% to 20% with a mean value of 10%, which is in agreement with the expected deviations that were modeled in section 3.2. The main reason for these deviations is assumed to be variations in mounting conditions of the cantilever actuators on microscopic glass slides. The actuators were mounted manually, which can lead to varying clamping conditions and thus different effective lengths of the cantilevers. However, clear trends for the influence of the thermal treatments on electromechanical performance of the actuators could be derived from the measurements.

Summarizing the outcome of the electromechanical measurements, the following trends can be identified. Firstly, it is observed that annealing at higher temperatures of up to 140 °C leads to higher d_{31} coefficients. A threshold of approximately 110 °C is visible above which d_{31} increases significantly. Secondly, a low pressure argon plasma treatment of the fully processed and annealed samples leads to an increase in d_{31} compared to samples that

were treated thermally only. Thirdly, a brief investigation suggests an influence of the kinetics of the annealing on the electromechanical behavior. A reduction of the temperature gradient from 0.8 K min^{-1} to 0.3 K min^{-1} that was employed for heating up and cooling down the samples leads to an increase in d_{31}.

For an application of the actuators, a trade-off between large d_{31} coefficients and the thermal stability of the substrates has to be made. In the investigations in this work, biaxially oriented PET substrates with an upper working temperature of approximately 140 °C were used [154]. Compared to other technical polymer substrates like PE (polyethylene), PP or PMMA, the upper working temperature of PET is relatively high. If applications demand one specific substrate material with a low glass transition temperature, the annealing of the P(VDF-TrFE) films has to be adjusted and will lead to lower d_{31} values. In the following sections, results from electrical measurements and morphology investigations will be presented and put in relation to results from electromechanical characterization.

5.4 Electrical characterization

When an electric field is applied to a P(VDF-TrFE) film at room temperature, dipoles are aligned and lead to a polarization P in the films. When the field is removed, a remanent polarization P_{rem} can be observed which corresponds to dipoles that remain aligned without an electric field. The polarization versus electric field can be investigated by measuring ferroelectric hysteresis loops. An example hysteresis loop is plotted in Figure 5.7. Characteristic values are the remanent polarization P_{rem}, maximum polarization P_{max} and the coercive field E_c which is the electric field that needs to be applied to achieve zero polarization of a previously oppositely poled sample. For distinct piezoelectric behavior a large remanent polarization is desired [18,119].

In this section, ferroelectric hysteresis measurements are presented that were performed on all inkjet printed piezoelectric elements using various thermal treatments. In order to assure comparability with the electromechanical characterization discussed in section 5.3, identical thermal treatments were employed. The measurements were performed using a commercial ferroelectric hysteresis measurement system (Aixacct GmbH, Germany, EasyCheck 300), which is based on a current-to-voltage converter (transimpedance amplifier). The system was connected to the same high-voltage amplifier that was used during deflection measurements (2220CE, Trek Inc., USA). Measurements were run at a frequency of 0.05 Hz. In order to ensure thorough poling, the cycles were repeated five times.

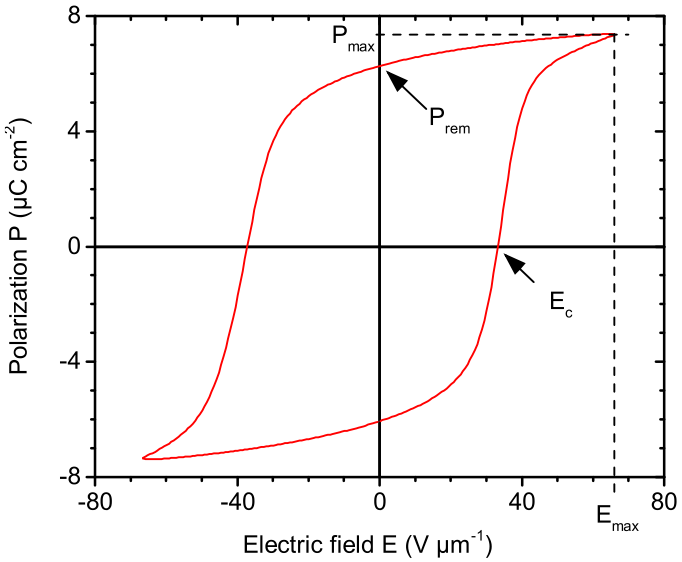

Figure 5.7 Ferroelectric hysteresis curve for one printed P(VDF-TrFE) sample. Remanent polarization P_{rem}, maximum polarization P_{max} as well as coercive field E_c and maximum electric field E_{max} are marked.

Figure 5.8 shows an example hysteresis curve measured on one sample for different maximum driving fields. It can be seen that for low driving fields (< 30 V µm^{-1}) only very little polarization is measured and no pronounced hysteresis is observed. With larger electric fields (> 40 V µm^{-1}), distinct hysteresis loops are gained. It can be seen that the remanent polarization increases with increasing maximum electric field.

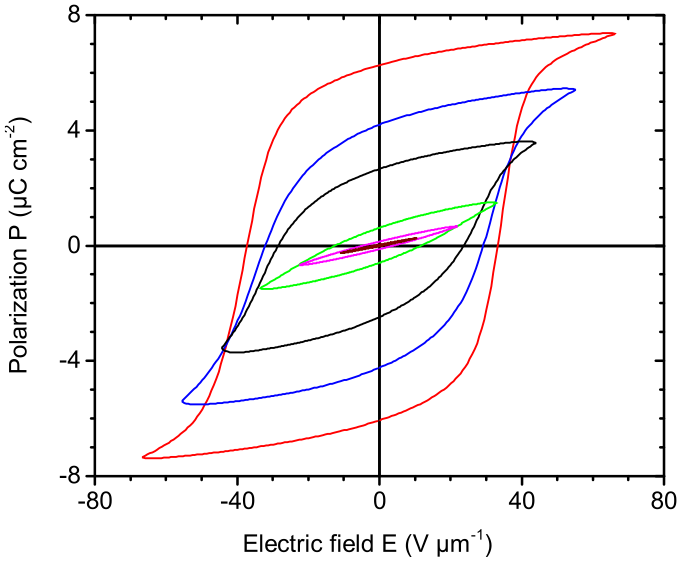

Figure 5.8 Ferroelectric hysteresis curve for one printed P(VDF-TrFE) sample driven at different fields.

From those measurements, the remanent polarization with respect to the applied maximum electric field was extracted and is displayed in Figure 5.9. When the maximum field during hysteresis measurements is higher than 40 V µm^{-1}, the remanent polarization

increases steeply and increases further with increasing electric field. Thus, large fields would in principle be preferred to achieve high-performing actuators.

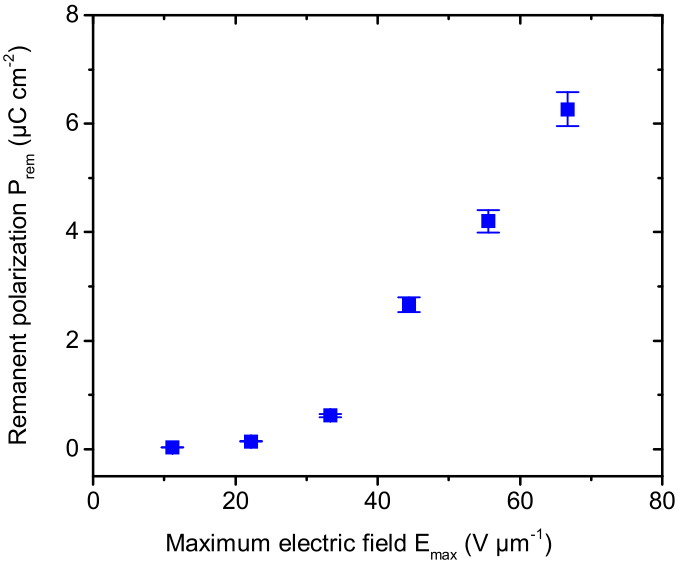

Figure 5.9 Remanent polarization dependent on applied maximum electric field.

However, imperfections in the printed P(VDF-TrFE) films lead to more frequent dielectric breakdown of the samples when driven at large fields. In order to avoid this, measurements were performed with reduced driving fields. For the test pads that were used for ferroelectric hysteresis measurements, the maximum driving voltage was limited to 600 V, which corresponds to an electric field of approximately 67 V µm^{-1}. As discussed previously, for cantilever test samples that were used in deflection measurements, the voltage was further reduced to 400 V, corresponding to an electric field of 44 V µm^{-1}. With these driving parameters, a yield (percentage of working samples) of more than 90% was achieved. Due to the reduced driving fields, the full performance of the samples is not utilized but underestimated by the measurements presented in this work. In other words, the performance of the inkjet printed samples is influenced and partially limited by film quality.

Figure 5.10 shows plots of the remanent and maximum polarization that were recorded for different temperature profiles for annealing the printed P(VDF-TrFE) films. At least five samples were measured for each temperature profile. In general, trends comparable to those observed during cantilever deflection measurements are visible. It can be seen that samples that were annealed thermally with temperatures below 110 °C exhibit only very little remanent polarization (< 1 µC cm^{-2}), while samples annealed above 110 °C show significantly higher values between 4 µC cm^{-2} and 5.2 µC cm^{-2} (a). Similar to the investigation of the coupling coefficient d_{31}, the highest remanent polarization was observed on samples annealed at 140 °C.

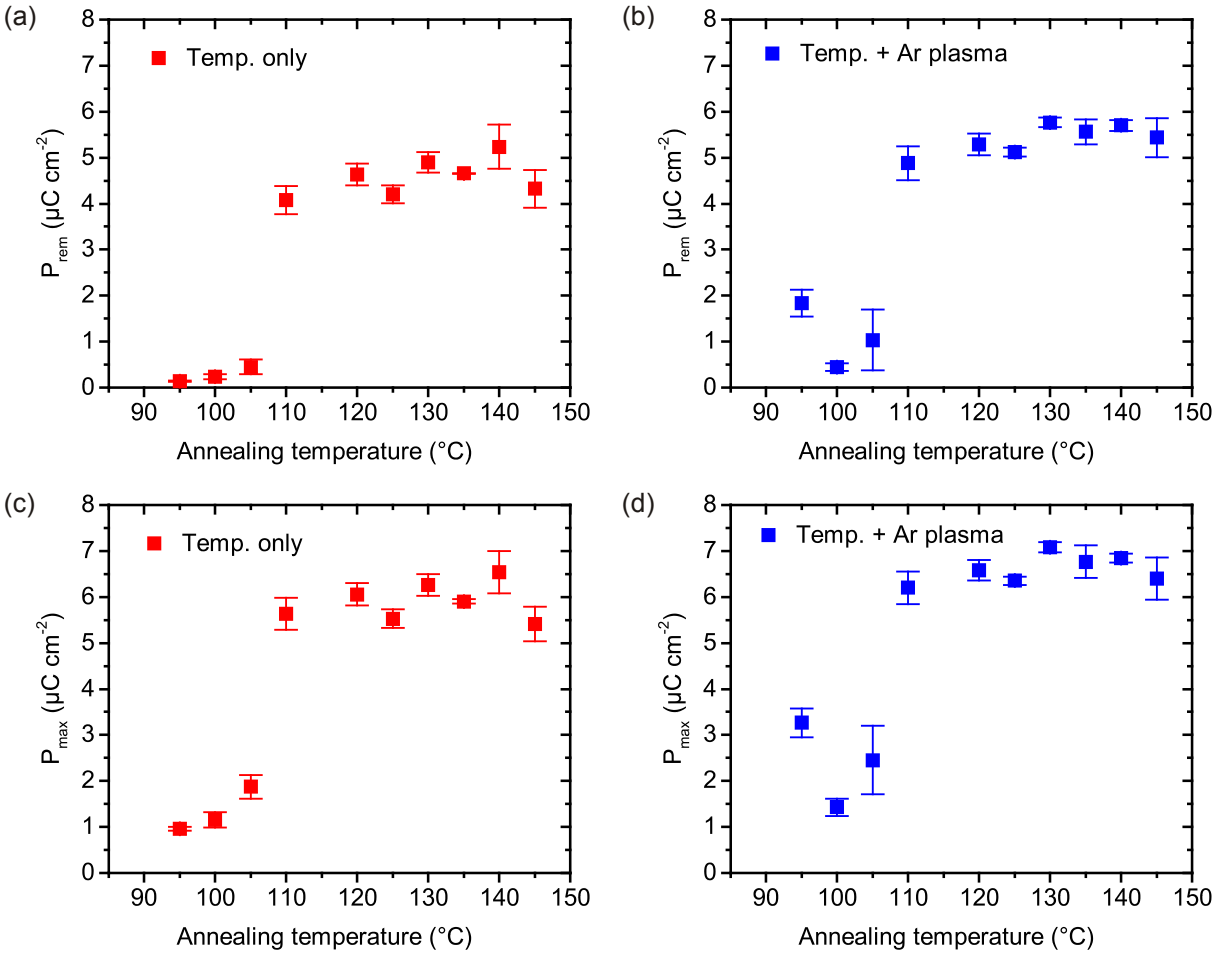

Figure 5.10 Remanent polarization P_{rem} (a-b) and maximum polarization P_{max} (c-d) for different thermal treatments of the piezoelectric layer.

An additional low pressure argon plasma treatment of the previously thermally annealed samples lead to an increase in remanent and maximum polarization. In average, an increase in remanent polarization of 1.4 µC cm^{-2} was observed. Values for P_{rem} of up to 5.8 µC cm^{-2} were determined (Figure 5.10 b). The standard deviations of the measurements are in general small with averages of 0.2 µC cm^{-2} for non-plasma treated samples and 0.3 µC cm^{-2} for plasma-treated samples. The maximum polarization shows similar trends like those observed for the remanent polarization with values ranging from approximately 1 µC cm^{-2} to 7 µC cm^{-2} (Figure 5.10 c-d).

Summarizing the ferroelectric characterization, the trends that were observed correlate with those discussed with electromechanical measurements. An increase in annealing temperature leads to an increase in remanent polarization P_{rem}. Annealing above 110 °C results in significantly higher P_{rem} than annealing below 110 °C. Furthermore, an additional argon plasma treatment of the fully processed samples leads to generally higher P_{rem} compared to samples that were solely heat-treated.

5.5 Morphology of printed P(VDF-TrFE) films

In order to better understand the significant influence of the annealing regime on actuator performance that was discussed in the previous sections, the morphology of inkjet printed P(VDF-TrFE) films subjected to different thermal and combined thermal and plasma treatments is investigated in this section. It is known that a thermal treatment of P(VDF-TrFE) films influences the crystallinity of the paraelectric α-phase and the ferroelectric β-phase. This has been studied extensively with various crystallographic methods like XRD, DSC or FTIR [17] for bulk P(VDF-TrFE) and spin-coated films, but not yet for inkjet printed films. In this work, the morphology of inkjet printed P(VDF-TrFE) films was investigated using DSC, XRD and AFM. The aim of the experiments was to establish correlations between the morphology and the actuator performance. This has not yet been demonstrated for printed P(VDF-TrFE) actuators.

In order to keep the morphology investigations brief, three post-treatments were selected that lead to significant differences in electrical and electromechanical performance. Table 5.1 shows the post-treatments that were selected and the corresponding results from electrical and electromechanical characterization. Furthermore, characteristic morphological information is listed.

Table 5.1 Overview of temperature profiles that were selected for morphology investigations. The piezoelectric coupling coefficient d_{31} and the remanent polarization P_{rem} that were determined for the specific temperature profiles are given as a reference along with characteristic morphological information.

Sample	Treatment	d_{31} (pm V^{-1})	P_{rem} (μC cm^{-2})	Morphology from AFM	Domain size (nm)
A	95 °C	0.8 ± 0.04	0.1 ± 0.01	rod-like	21 ± 7
B	130 °C + Ar-plasma	8.0 ± 0.2	5.8 ± 0.1	globular	63 ± 24
C	145 °C	6.6 ± 0.4	4.3 ± 0.4	globular	138 ± 62

5.5.1 Differential scanning calorimetry

For calorimetric characterization, the printed P(VDF-TrFE) films were removed carefully from the metalized glass substrates using a razor blade to ensure that the underlying metalization remains undamaged. The removed films were then analyzed on a DSC 204 F1 Phoenix (Netzsch, Selb, Germany) in a temperature range between -20 °C and 200 °C. For all measurements, the DSC heating and cooling rates were 10 K min^{-1}. The amorphous fraction

of P(VDF-TrFE) is known to exhibit a glass transition temperature T_G in the range of -20 °C to -40 °C [116,117]. T_G is thus outside the temperature range of annealing and operation of the samples and was not investigated further here.

Figure 5.11 shows the endothermic heat flow recorded during the first DSC heating run for thermally annealed P(VDF-TrFE) films in a temperature range between 80 °C and 160 °C. Additionally, one sample that was not heat-treated after printing was measured as a reference. All curves exhibit endothermic peaks with maxima at approximately 105 °C and 150 °C. The first peak at 105 °C is known to correspond to the solid-solid phase transition from crystals of the ferroelectric β-phase to the paraelectric α-phase. The temperature at which the phase change occurs is also known as Curie temperature T_C [17,111,164]. The as-printed reference sample exhibits a relatively broad T_C peak. The peak becomes more pronounced for the sample annealed at 95 °C, which is close to the peak transition temperature of the Curie transition. Barique and Ohigashi [165] interpreted this effect in solvent-cast P(VDF-TrFE) films as the transformation from *gauche* defects into an *all-trans* chain configuration that corresponds to the ferroelectric β-phase.

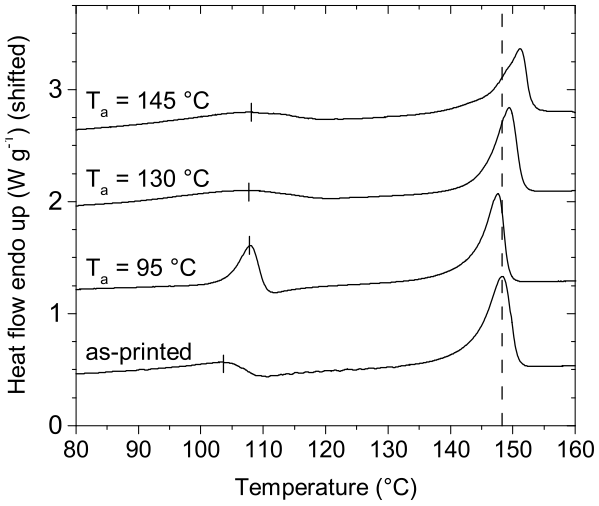

Figure 5.11 DSC plot (first heating) for P(VDF-TrFE) films that were heat-treated at different temperatures after printing. Curves are shifted for better visibility.

Films annealed at 130 °C and 145 °C exhibit broader Curie transition peaks compared to the film that was annealed at 95 °C. During an annealing above T_C, the paraelectric α-phase with a *gauche-trans* chain configuration is stable [166]. Therefore, the transformation into the *all-trans* configuration that was observed for the sample annealed at 95 °C does not occur. Furthermore, the peak Curie transition temperatures exhibit maxima at 108 °C, which is slightly higher than in the reference sample (104 °C). A possible reason for this are differences in the thermal history and the crystallization conditions of the films. The

crystallization of the as-printed reference sample is believed to depend mainly on the thermal history of the polymer powder, ink composition and drying of the as-printed film. The situation is different for samples that were annealed at 130 °C and 145 °C, where the crystallization strongly depends on the cooling rate that was employed after annealing. This cooling rate was 0.8 K min^{-1} for the samples discussed here and therefore, similar Curie temperatures are present for annealing temperatures of 130 °C and 145 °C. The endothermic melting peak of the P(VDF-TrFE) crystals at approximately 150 °C is shifted to higher temperatures with increasing annealing temperatures (148.3, 149.4 and 151.1 °C for the as-printed, 130 °C and 145 °C-sample, respectively). The shift of the melting peak suggests the growth of larger crystals when higher annealing temperatures are employed (Gibbs-Thomson effect) [167].

Figure 5.12 shows the DSC plots of the first cooling and the second heating run. From the first cooling run (a), crystallization at approximately 136 °C can be seen for all samples. As all samples were heated up to 200 °C during the first heating run, which is well above the melting temperature, their thermal history is mostly erased, which leads to similar DSC plots. The second heating run (b) supports these results. The melting temperature coincides for all samples at 151.8 ± 0.2 °C.

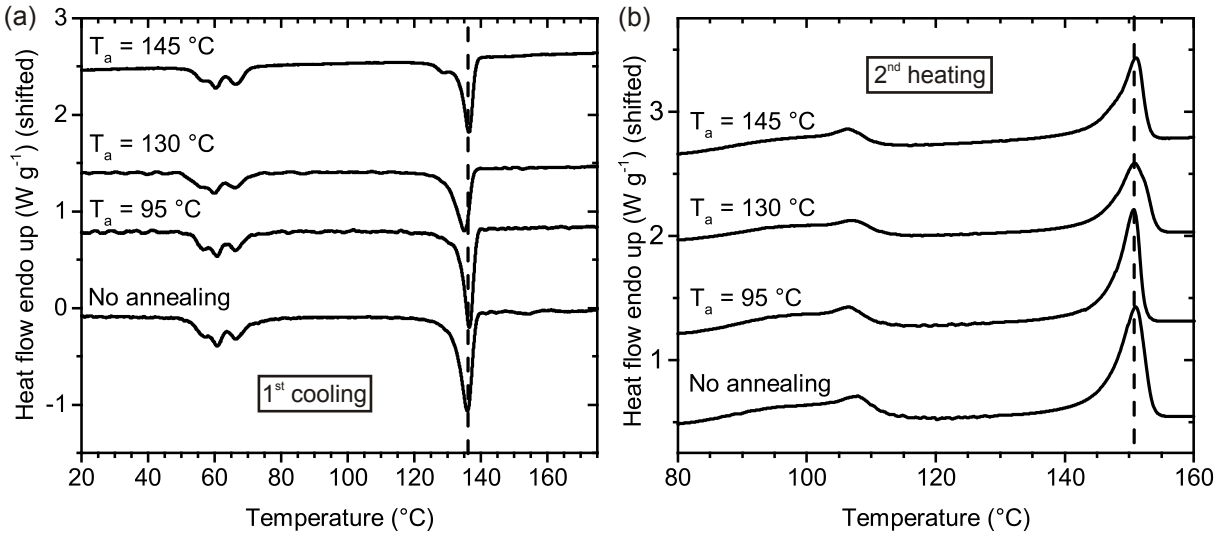

Figure 5.12 (a) DSC plot (first cooling) for P(VDF-TrFE) samples that were previously heat-treated at different temperatures after printing. (b) DSC plot for second heating.

5.5.2 X-ray diffraction

X-ray diffraction was used to determine which predominant phases are visible in the printed P(VDF-TrFE) films after different thermal treatments. Measurements were run using a Bruker D5005 diffractometer (Bruker, Germany, $\lambda = 0.154$ nm, step size 0.03°, integration time 2 s, geometry theta-2 theta). All measurements were performed at room temperature. Figure 5.13 shows the XRD spectra that were recorded for the different temperature regimes. Furthermore, as a reference, Table 5.2 shows the lattice parameters and the corresponding 2Θ peaks in the XRD spectra that are associated to the (110/200) lattice planes of the two phases.

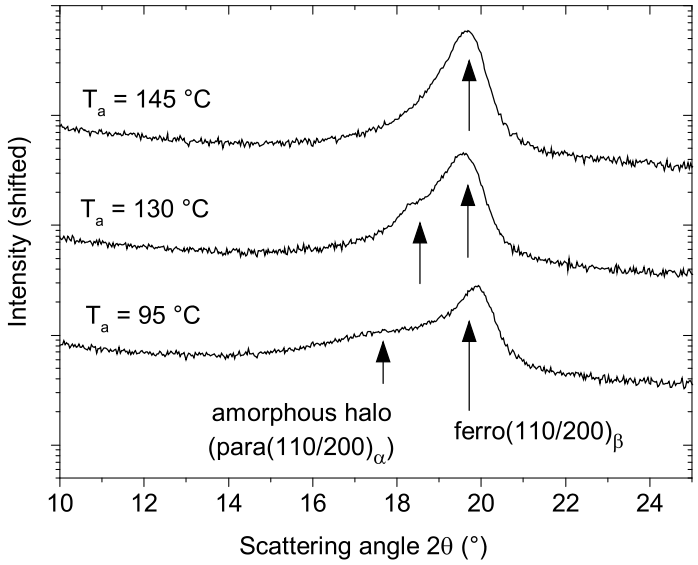

Figure 5.13 XRD spectra of printed P(VDF-TrFE) films with different annealing conditions. Curves are shifted for better readability.

Table 5.2 Ferroelectric and paraelectric lattice parameters for P(VDF-TrFE) copolymers with a VDF:TrFE ratio of 70:30 and corresponding first-order diffraction peaks, adapted from references [111,112,168].

Phase	**a** (Å)	**b** (Å)	**c** (Å)	**2Θ (110/200)** (°)
β-phase (ferroelectric, *all-trans*)	9.05	5.12	2.55	19.9
α-phase (paraelectric, *gauche-trans*)	9.86	n/a	2.3	17.1

The ferroelectric β-phase is orthorhombic and exhibits a (110/200) peak at 2Θ = 19.9° [111]. The non-ferroelectric or paraelectric α-phase has a hexagonal lattice and a (110/200)

peak at 2Θ = 17.1° [111]. All samples exhibit a Bragg peak at 2Θ ≈ 19.9°, which is attributed to the (110/200) peaks of the ferroelectric β-phase. Additionally, the P(VDF-TrFE) film that was annealed at 95 °C exhibits a shoulder or halo at 2Θ ≈ 16-18°. This can be interpreted as scattering from amorphous parts of the polymer. However, the shoulder occurs close to literature values of (110/200) reflexes of the paraelectric α-phase, which could indicate the existence of a certain amount of α crystals. For higher annealing temperatures of 130 °C and 145 °C, the peak at 19.9° becomes more pronounced and at the same time, the intensity of the shoulder significantly decreases. This indicates a structural rearrangement of the crystals during annealing and a formation of β-crystals during cooling to room temperature. The higher intensity of the (110/200) peak of the β-phase observed with those samples indicates a higher degree of crystallinity of the β-phase compared to the sample annealed at 95 °C.

5.5.3 Atomic force microscopy

In order to visualize the morphology of inkjet printed P(VDF-TrFE) films, atomic force microscopy (AFM) was employed. An NT-MDT Solver (NT-MDT, Russia) was run in tapping mode using JPK NSC35 tips with a radius of > 10 nm. The domain sizes denoted in Table 5.1 were derived from line scans of at least 30 objects. For each sample, images were taken at two to four representative spots on the sample. Figure 5.14 shows a height profile and phase image of the as-printed reference sample. Rod-shaped crystallites with a diameter of 21.0 ± 6.9 nm are visible, which is typical for P(VDF-TrFE) crystals [18]. Furthermore, several pinholes were observed at smaller magnifications (data not shown).

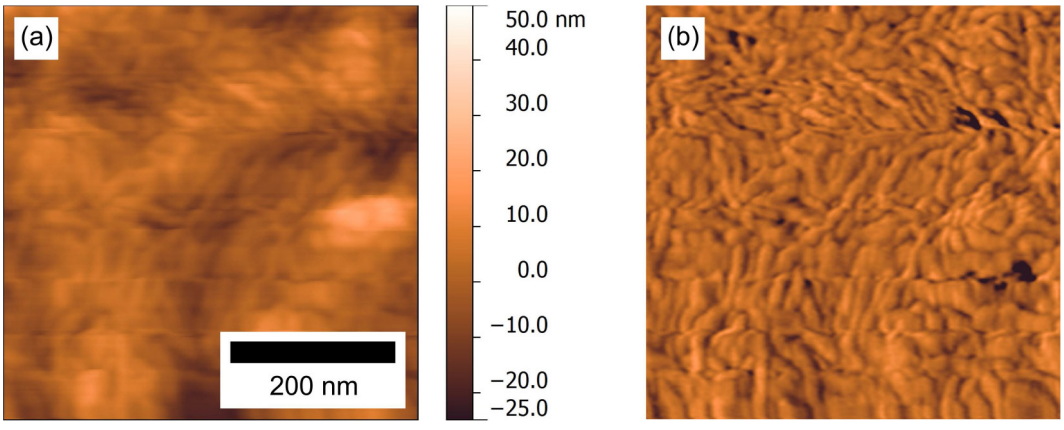

Figure 5.14 Height profile (a) and phase image (b) of one as-printed P(VDF-TrFE) sample.

Height and phase images of a sample annealed at 95 °C, which is below the phase transition, are displayed in Figure 5.15. The images are very similar to the un-treated sample. As before, rod-like crystallites with slightly larger diameters than for the untreated sample

were measured (21.2 ± 6.9 nm). However, this difference is within the measurement inaccuracy.

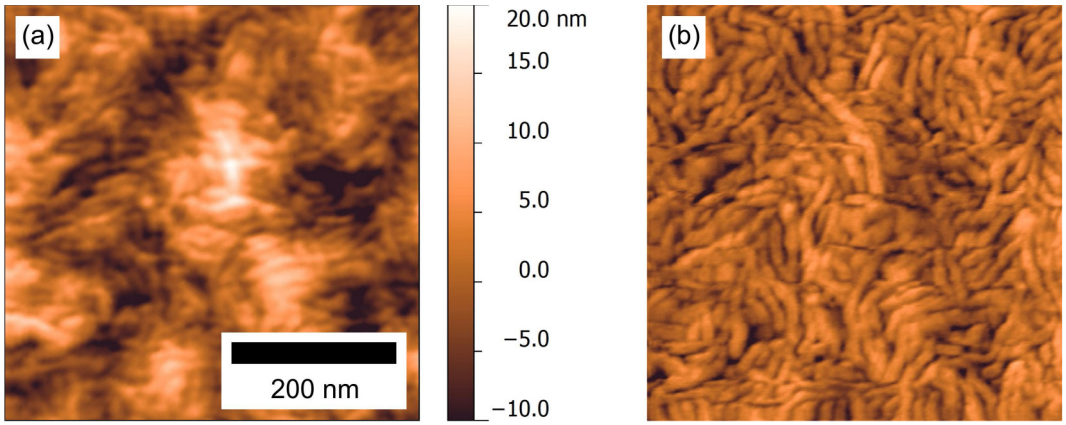

Figure 5.15 Height profile (a) and phase image (b) of one printed P(VDF-TrFE) sample annealed at 95 °C.

The sample annealed at 130 °C, thus above the Curie transition that was observed in DSC measurements, shows significant differences in morphology compared to the previous samples (see Figure 5.16). Significantly larger crystallites are visible with an average diameter of approximately 63 ± 24 nm. Furthermore, the morphology changes from rod-like to globular structures. This indicates that the increased thermal energy during annealing leads to changes in the overall morphology and not only induces a phase transformation.

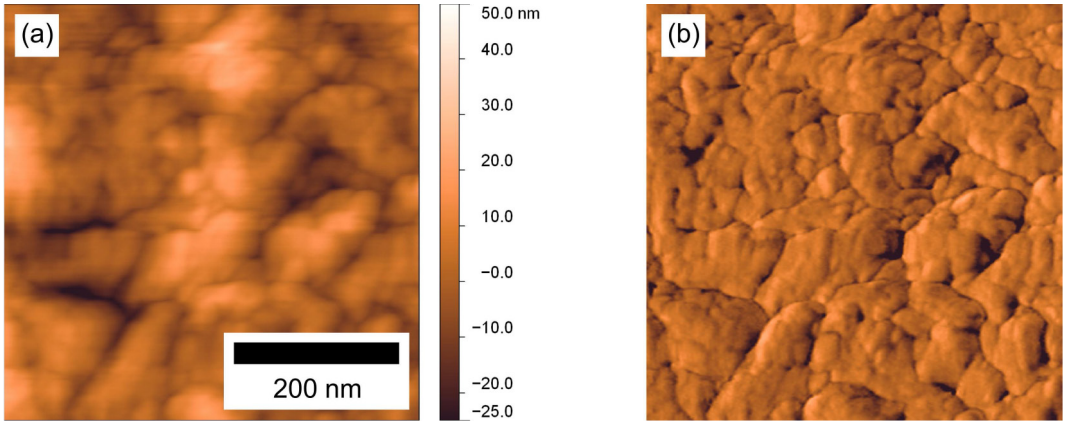

Figure 5.16 Height profile (a) and phase image (b) of one printed P(VDF-TrFE) sample annealed at 130 °C.

When the P(VDF-TrFE) films are annealed at 145 °C, a further increase in crystallite size is visible (138 ± 62 nm), as depicted in Figure 5.17. This increased healing of defects can be caused by an increased polymer chain mobility at higher annealing temperatures, which leads to larger crystallites. DSC characterization showed that the polymer is partly molten at such high annealing temperatures (see Figure 5.11). With a partly molten polymer, defect healing is accelerated further and melted crystallites can attach to larger crystallites [169].

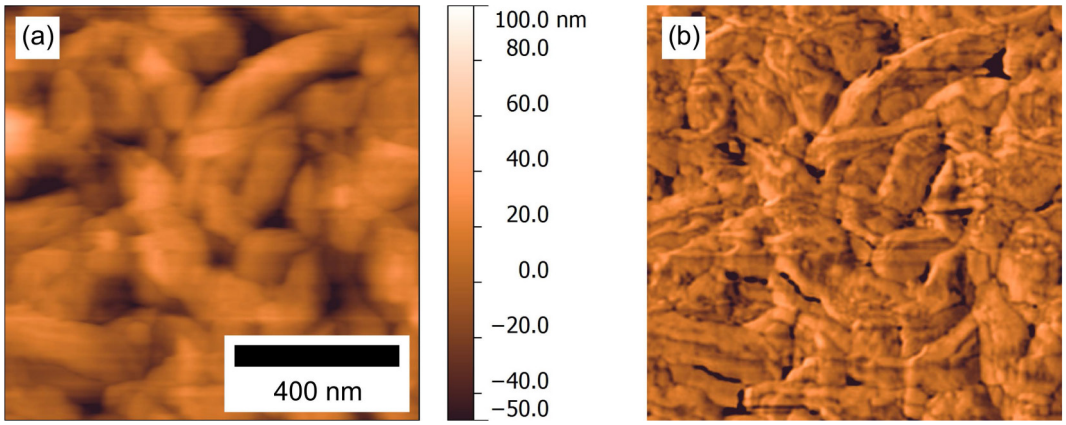

Figure 5.17 Height profile (a) and phase image (b) of one printed P(VDF-TrFE) sample annealed at 145 °C.

In general, the AFM images that were taken from inkjet printed P(VDF-TrFE) films compare well with results published by Mao et al. [18] (reprinted in Figure 2.2). The AFM height profiles in this work are very similar to those that were published by Mao et al. Furthermore, the increase in grain size with annealing at higher temperatures confirms the shift in melting temperature that was observed during DSC measurements.

5.6 Discussion and processing recommendations

In this section, the influence of processing conditions on electrical and electromechanical actuator performance as well as morphology are discussed. It is found that the thermal treatment that is employed after printing the P(VDF-TrFE) films strongly influences both device performance and morphology. A critical annealing temperature of 110 °C is observed. Samples annealed between 110 °C and 140 °C show high remanent polarization values of up to 5.8 µC cm^{-2} and d_{31} coefficients of up to 10 pm V^{-1}. At low annealing temperatures of 95 °C as well as in the as-printed reference sample, rod-like crystalline domains were observed, which is typical for P(VDF-TrFE) crystals [18]. Defect healing in this sample is localized and coincides with low piezoelectric d_{31} coefficients and remanent polarization P_{rem}. When annealing is performed at higher temperatures (130 °C and 140 °C), which corresponds to significantly higher actuator performance, the overall morphology changes from rod-like to globular. DSC measurements indicate larger crystals and XRD measurements suggest an increased degree of crystallinity for those samples. Unfortunately, no absolute values for the degree of crystallinity were derived. The high polarity of the P(VDF-TrFE) films lead to electrostatic interactions with the DSC pan, and therefore complete thermal contact between the P(VDF-TrFE) and the bottom of the DSC pan could not be guaranteed. Moreover, the degree of crystallinity could not be estimated by

XRD, since it is challenging to clearly separate the scattering contributions from the amorphous and crystalline phases.

The results that were obtained compare well with results from literature [6,17,18,119]. Additional information is gained in this work, as not only the remanent polarization but also the piezoelectric d_{31} coefficient is investigated. For the application of unimorph actuators, this is the most direct property. Furthermore, this work provides the first study of inkjet printed P(VDF-TrFE) films. Apart from solely thermally treated samples, also combinations of thermal treatments and subsequent low-pressure argon plasma treatments are investigated. The established knowledge can be applied to choose appropriate processing conditions and design also other P(VDF-TrFE)-based devices like sensors or non-volatile memory elements. For an actual application of inkjet printed P(VDF-TrFE) actuators, a trade-off has to be made between high actuator performance and thermal compatibility with the substrate material. The annealing should be carried out using a temperature of at least 110 °C to achieve reliable and distinct piezoelectric behavior. Higher temperatures of up to 140 °C lead to increased d_{31} coefficients. The upper working temperature of the PET substrates used in this work is approximately 140 °C [154] and thus higher than for many other technical polymer substrates like PMMA. Depending on the thermal stability of the substrate material, annealing temperatures up to these values might be applied. Apart from the maximum temperatures tolerated by the substrates, also the influence of the multi-material setup of substrate, electrodes and P(VDF-TrFE) films has to be considered.

6 Static and dynamic actuator behavior

In the previous sections, the process flow for all-printed P(VDF-TrFE) actuators was described and correlations between the crystallinity of the printed P(VDF-TrFE) films and device performance were investigated. Based on those findings, processing recommendations were derived. This section presents results of geometry-dependent actuator performance under static and dynamic driving conditions. Cantilever as well as membrane actuators with different lengths or diameters are investigated. For all samples, voltage-dependent static deflection, resonance frequency and deflection when driven at resonance frequency were recorded. Exemplary measurements of force-deflection characteristics were also performed. The results obtained are compared to the analytical actuator models that were described in chapter 3 and serve as a basis for setting up a micropump demonstrator. Furthermore, basic investigations of device stability were carried out. These investigations include measurements of deflection and resonance frequency under cyclic driving conditions, measurements of heat generation during cyclic operation and device operation at elevated temperatures.

6.1 Test structures and sample preparation

The geometry-dependent actuator performance was investigated using cantilever as well as membrane actuators. For both sample types, lengths or diameters of 10 mm and 15 mm were chosen for the experiments. Figure 6.1 shows a photograph of exemplary samples. The actuators were manufactured as described in chapter 3. Annealing of the printed P(VDF-TrFE) films was performed at a maximum temperature of 130 °C. Based on the findings discussed in chapter 5, this temperature regime leads to good actuator performance and is significantly below the upper working temperature of the PET substrates. The printed silver top electrodes were sintered with a combined thermal and low-pressure argon plasma treatment.

Cantilever beam samples were mounted on microscopic glass slides using commercial cyanoacrylate adhesive (Uhu GmbH, Germany), similar to the preparation of samples described in chapter 5. Membrane samples were mounted on custom aluminum rings with inner diameters of 10 mm or 15 mm. In order to reduce the mechanical stress in the membranes that result from the strain caused during the first application of an electric field, the membrane actuators were poled electrically prior to mounting.

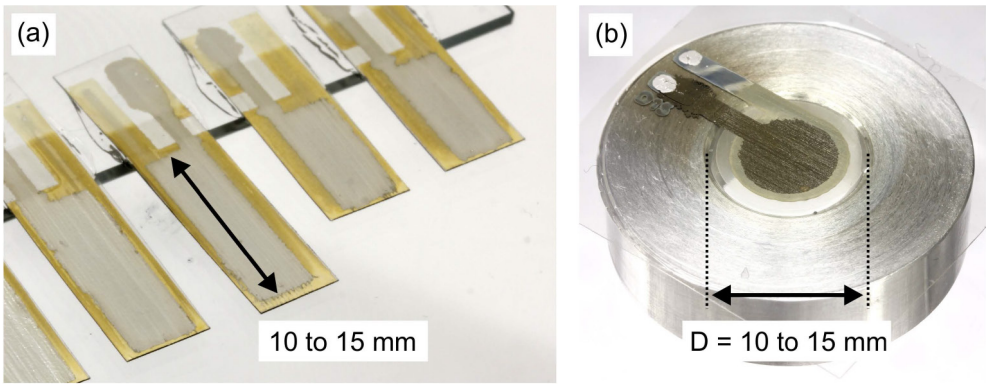

Figure 6.1 Cantilever (a) and membrane actuators (b) used as test structures for the investigation of static and dynamic actuator behavior.

6.2 Static actuator characterization

6.2.1 Geometry-dependent static deflection

Static deflection measurements were performed using the setup and measurement routine introduced in section 5.3. As described there, the samples were poled at room temperature for one minute using a voltage of 400 V. For characterization, three voltage cycles 0 V – 400 V – 0 V were applied and the third cycle was analyzed. For cantilever beam actuators, the deflection was measured close to the tip of the beam, while for membrane actuators the deflection was measured in the membrane center. For all types of geometries, five to ten samples were characterized.

The static deflection of cantilever actuators with respect to driving voltage is plotted in Figure 6.2. For both 10 mm and 15 mm long cantilever beams, an approximately linear increase of deflection with increasing voltage can be observed. The average correlation coefficient for a linear fit of the measured deflection is $R^2 = 0.96$. The measured deflections at selected voltages are plotted along with the corresponding standard deviation. Cantilevers with a length of 15 mm exhibit maximum deflections of approximately 145 µm, while those with a length of 10 mm yield maximum deflections of 65 µm. Standard deviations of the deflection were found to be in the range of 6% to 12%, which demonstrates a good reliability of the measurement setup and sample preparation. From the measured deflection, the average piezoelectric d_{31} coefficient was derived for both 10 mm and 15 mm long cantilevers by fitting the measured deflection to the analytical model discussed in chapter 3. d_{31} values between 7 pm V^{-1} and 9 pm V^{-1} are found, which is in good agreement with the results described in section 5.3 for the respective thermal annealing profile.

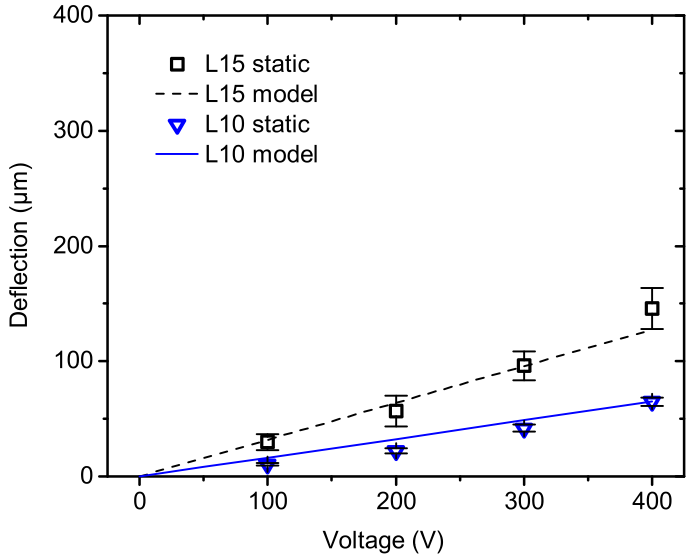

Figure 6.2 Static deflection behavior for cantilever actuators with different length dependent on driving voltage.

Table 6.1 lists the material parameters that were employed in the model. For modeling cantilever actuators, a Young's modulus of the PET substrate of 2 GPa is chosen. The modeled deflections are plotted as lines in Figure 6.2 and agree well with the measured actuator performance. This confirms the applicability of the model which was employed within the range of geometries under investigation.

Table 6.1 Material parameters used for modeling of actuator behavior.

	Substrate PET	**Electrodes** Ag	**Piezoelectric film** P(VDF-TrFE)
Layer thickness (µm)	125	2.3 (total)	9
Young's modulus (GPa)	2 to 4 [154]	40 [157]	2 [118]
Piezoelectric coefficient d_{31} (pm V^{-1})	n/a	n/a	7 to 9

Figure 6.3 depicts the voltage-dependent static deflection of membrane actuators with 10 mm and 15 mm diameter. As observed during characterization of cantilever actuators, an approximately linear dependence of deflection on voltage is found; the average correlation coefficient for a linear fit is $R^2 = 0.96$. The maximum deflections at 400 V driving voltage are approximately 2.1 µm and 1.2 µm for membrane diameters of 15 mm and 10 mm, respectively. Compared to cantilever bending beams the deflections are significantly lower due to the different clamping conditions. The standard deviations are in the range of 20 to 27%, which is higher than observed for cantilever actuators. The deviations are believed to occur mainly due to the small absolute deflections which are more sensitive to errors and tolerances in the measuring setup like positioning accuracy of the measurement spot.

Furthermore, the manual mounting of the membranes is expected to induce additional deviations.

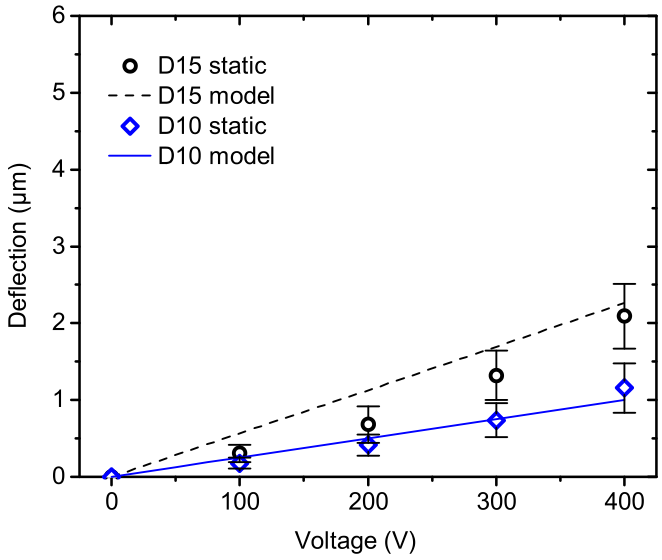

Figure 6.3 Static deflection behavior of membrane actuators with different diameters dependent on driving voltage.

When comparing measured deflections to results from the analytical model for membrane deflection that was introduced in chapter 3, good agreement between measurements and model was found when a Young's modulus of the substrate of 4 GPa was assumed. Compared to 2 GPa that were employed to model cantilever actuators, this is significantly higher. This indicates stresses in the membrane that occur during manufacturing of the actuators, especially during heat-treatments as well as during mounting and curing of the adhesive bonding layer. Altogether, these stresses lead to increased membrane stiffness. However, the stress-induced stiffening can be implemented in the model by varying the Young's modulus of the PET substrate within the range that is specified by the manufacturer [154]. When using more sophisticated bonding technologies, like thermal pressure bonding [10], it is expected that these influences can be reduced. Furthermore, an actuator sandwich with polymer-based electrodes (e.g. PEDOT:PSS) instead of silver electrodes could reduce the thermal mismatch and thus thermal stresses induced during manufacturing.

Summarizing the static deflection measurements, it was proven that the analytical models describe the scaling of the actuator deflection with driving voltage and geometry correctly. For membrane actuators, stresses in the membrane lead to more stiff behavior than observed for cantilever actuators. In the model this can be accounted for by modifying the Young's modulus of the PET substrate. For all samples, a linear dependency of deflection on voltage was verified. Standard deviations of the deflections were derived from five to ten

samples per type of geometry and size and are found to be low (6 to 12%) for cantilever and higher (20 to 27%) for membrane actuators. These deviations are assumed to occur due to variations in clamping conditions and for membrane actuators also due to the small absolute deflections.

6.2.2 Force-deflection behavior of printed actuators

Another key characteristic in actuator performance is the force-deflection behavior. For the application of an actuator, it is important to know the deflection under a certain mechanical load. This information can be extracted from a working diagram which plots force with respect to deflection at a given driving voltage. Characteristic points in such a working diagram are the free deflection where the force is equal to zero and the blocking force, which is the maximum force generated by the actuator at zero displacement. The force-deflection characteristics of inkjet printed P(VDF-TrFE) actuators was investigated exemplary for three cantilever actuators with a length of 15 mm and for one membrane actuator with a diameter of 15 mm. Force and deflection were measured with a tactile micro force sensor (FT-FS 1000, FemtoTools AG, Switzerland) with a piezo-driven micro positioning stage. Figure 6.4 shows a photograph of the measurement tip of the force sensor positioned over a membrane actuator. The device is capable of recording force and position automatically with user-defined step size and measurement range. With the type of sensing chip that was used, forces up to 10 mN can be measured with a force resolution of 0.5 µN and a displacement resolution of 5 nm.

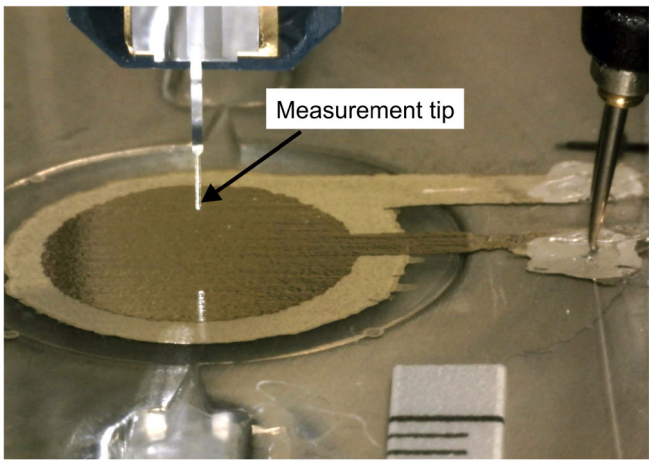

Figure 6.4 Close-up view of the setup used for force-deflection measurements. The measurement tip is positioned above a membrane actuator.

Prior to measuring, the force sensor was referenced by driving the sensor in contact with the actuator while no voltage was applied. Afterwards, the force sensor was moved away from the actuator and the actuator was deflected by applying a static voltage. Then, the force

sensor was driven into contact with the deflected actuator tip, and the force-deflection behavior was recorded automatically. For the measurements in this work, a displacement step size of 0.5 µm was chosen. Figure 6.5 shows the working diagram that was recorded for a cantilever actuator at driving voltages between 200 V and 600 V.

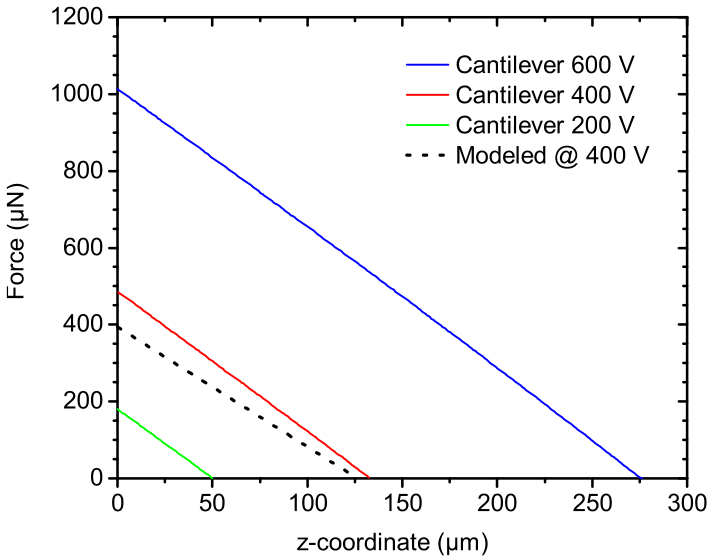

Figure 6.5 Measured working diagram of a cantilever actuator with 15 mm length.

With a driving voltage of 400 V, a free deflection of approximately 130 µm was measured, which is in good agreement with the deflections measured by the laser triangulation sensor setup that was employed to characterize the static actuator deflection. For higher driving voltages, up to 275 µm free deflection were measured. Blocking forces in the range of 180 µN to 1015 µN were measured. For all driving voltages, a linear relationship between force and deflection was observed. This is in accordance with the analytical model that was discussed in section 3.2. The slope of the lines in the working diagram is described by equation (3.9) and depends on beam geometry and Young's modulus. The working lines for different driving voltages are parallel to each other. In order to compare the measured values with the analytical model, the modeled force-deflection behavior for a driving voltage of 400 V is plotted as a dashed line. The modeled and measured free deflection values are in approximate agreement, while the measured blocking force is 23% higher than the modeled value, which is attributed to uncertainties of actuator geometry and furthermore drift effects during measurements.

In order to estimate the maximum force or backpressure in a membrane pump, Figure 6.6 displays a working diagram that was recorded for a pump demonstrator that is characterized in more detail in chapter 7. Due to the different clamping conditions compared to cantilever actuators, the deflections are significantly lower while the blocking forces are

larger. The force-deflection characteristics were recorded for driving voltages between 200 V and 600 V. In this range, free deflections of 2 µm to 8.5 µm and blocking forces of approximately 750 µN to 3750 µN were measured. Similar to the characterization of cantilever actuators, the working lines for different driving voltages are approximately parallel to each other. The modeled working line at a driving voltage of 400 V (extracted from section 3.3, Figure 3.7) is plotted as a dashed line. Measurements and model are in approximate agreement with a measured blocking force 13% above the modeled value. It should be noted that this exemplary pump demonstrator sample showed higher deflections than the samples discussed in section 6.2.1 due to higher poling fields and improved mounting that were employed.

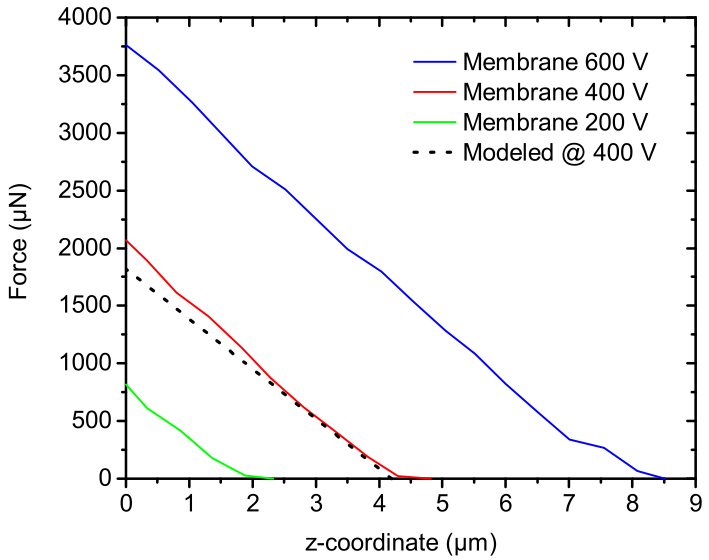

Figure 6.6 Measured working diagram of a membrane actuator with a diameter of 15 mm.

Based on the brief experimental investigation of force-deflection behavior discussed in this section, it can be concluded that the actuators exhibit relatively large free deflections but low blocking forces of up to 1 mN and 3.8 mN for cantilever and membrane actuators, respectively. Due to the intrinsic properties of the polymer actuators (low Young's modulus), blocking force and actuator stiffness are much lower than it would be the case for piezoceramic actuators, as discussed in section 2.2. In general, the force-deflection behavior that was derived experimentally is in agreement with basic analytical descriptions.

6.3 Dynamic actuator characterization

6.3.1 Geometry-dependent resonance frequency

Apart from the static actuator behavior, also the dynamic actuator deflection was investigated. These investigations include measurements of the frequency-depending actuator deflection to determine the resonance frequencies. The deflected shape at resonance frequency was recorded, too. Furthermore, the actuator deflection and the associated volume change under driving at resonance frequency with different voltage amplitudes were measured.

Dynamic actuator characterization was carried out using a laser scanning vibrometer (PSV-400/PSV-A-410, Polytec GmbH, Germany). The actuators were controlled using the same high-voltage amplifier that was used for static characterization. Measurements were run in the frequency domain, where dynamic voltages were applied to the actuator and the velocity was measured in the measurement spot. Using the vibrometer analysis software (PSV 9.1, Polytec GmbH, Germany), the actual frequency-dependent deflection was derived from the velocity by a fast Fourier transform algorithm. Deflected shapes were determined by scanning the measurement spot across the actuator surface in a user-defined grid. Figure 6.7 shows photographs of the measurement setup and the measurement grid for a cantilever actuator.

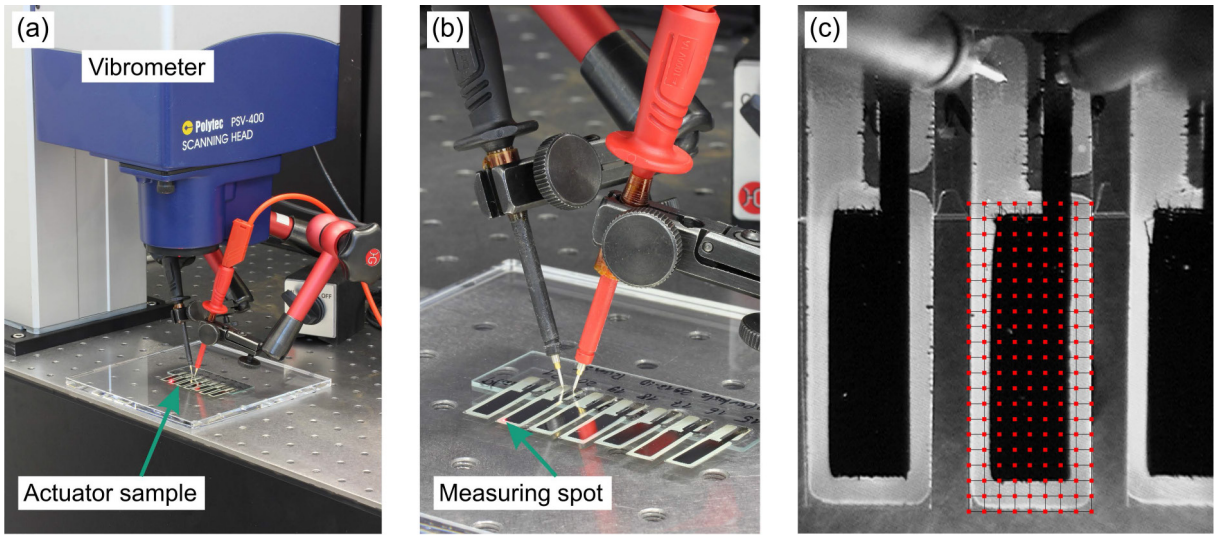

Figure 6.7 (a) Laser scanning vibrometer setup used for dynamic actuator characterization. (b) Close-up view of one cantilever sample. (c) Arrangement of measuring spots for a cantilever actuator.

The geometry-dependent resonance frequency was measured for both cantilever and membrane actuators by applying a periodic chirp signal with frequencies from 1 Hz to

20 kHz. Similar to the static measurements, at least five samples per type of geometry were characterized. Figure 6.8 plots the resonance spectra for cantilever actuators with 10 mm and 15 mm length. For both lengths, a sharp peak of the first resonance frequency is visible. The peaks are located at 274 Hz and 164 Hz for 10 mm and 15 mm cantilever length, respectively.

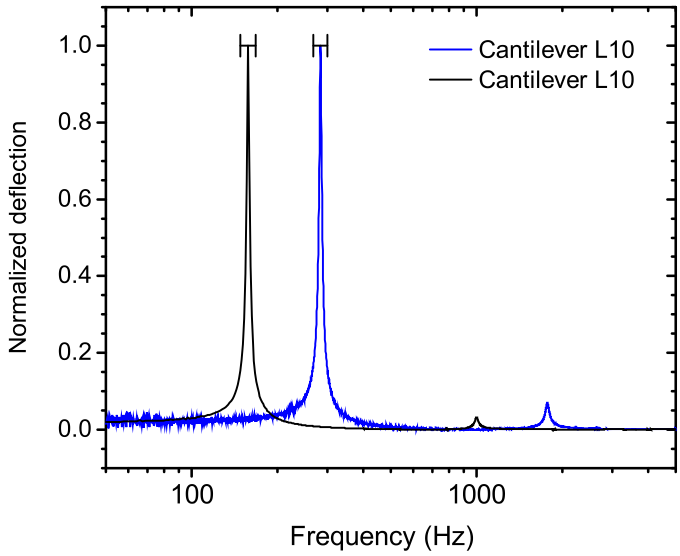

Figure 6.8 Normalized resonance spectra for cantilever actuators with 10 mm and 15 mm length. Standard deviations are indicated by error bars.

Standard deviations of approximately 6% for the first resonance frequency are obtained during measurements. The main reasons for these differences are assumed to be differences in actual cantilever length and mounting conditions that occur when the samples are glued on glass slides. The second resonance frequency was measured to be approximately 1.8 kHz and 1.0 kHz for 10 mm and 15 mm cantilever length, respectively. For the first resonance frequency f_{res}, the quality factor Q was calculated based on the following expression [148]:

$$Q = \frac{f_{res}}{B_{-3dB}}, \tag{6.1}$$

where B_{-3dB} is the bandwidth at which the deflection is reduced by -3 dB compared to the maximum deflection. For 10 mm and 15 mm cantilever length, quality factors of 104 and 50 were determined, respectively. These values are in a typical range for polymer-based cantilevers (10 to 100) [170,171].

Figure 6.9 shows the deflected shapes that were recorded for a cantilever actuator with 15 mm length for the first and second resonance frequency. The shapes agree with typical first and second order vibrational modes for cantilever beams [172].

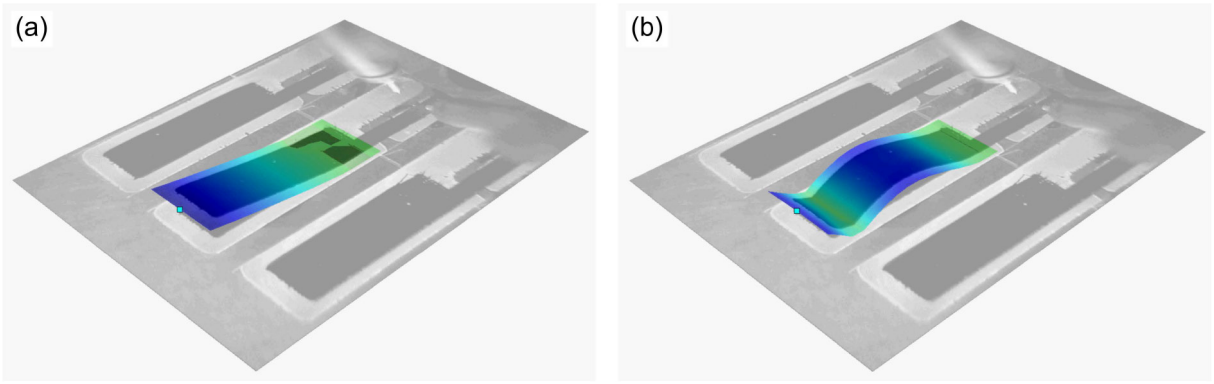

Figure 6.9 Deflected shapes measured for first (a) and second resonance frequency (b) of cantilever actuators.

For the first resonance frequency, one deflection node with zero displacement was observed (a), while for the second resonance frequency two deflection nodes were present (b). The deflected shapes were determined by measuring the frequency-dependent deflection over a grid of measurement points with a spacing of typically 0.5 mm.

Figure 6.10 displays the resonance spectra for membrane actuators. Due to the different clamping conditions compared to cantilever actuators, significantly higher resonance frequencies are obtained. The average peaks of the first resonance frequency are located at 5.8 kHz and 2.6 kHz for membrane diameters of 10 mm and 15 mm, respectively. The corresponding standard deviations are approximately 5% and quality factors between 30 and 40 were derived.

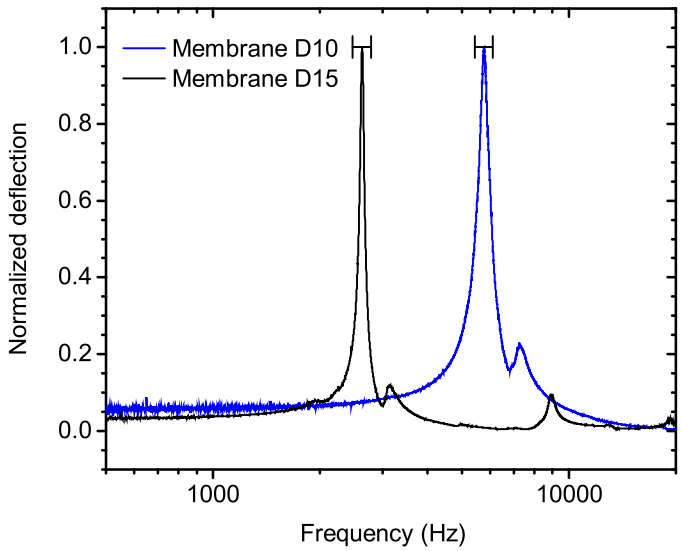

Figure 6.10 Normalized resonance spectra for membrane actuators with 10 mm and 15 mm diameter. Standard deviations are indicated by error bars.

The deflected shapes at the first and second resonance frequency were derived from the measurements and are displayed in Figure 6.11.

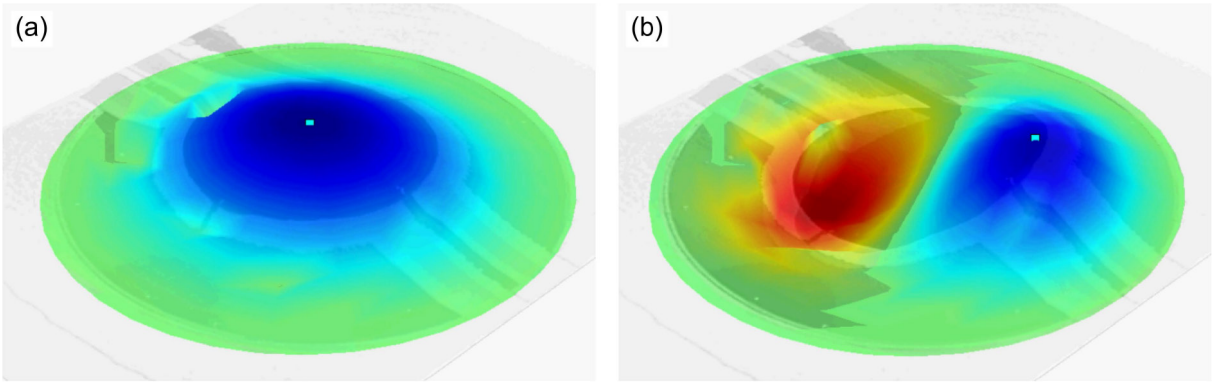

Figure 6.11 Deflected shape measured for first (a) and second resonance frequency (b) of membrane actuators.

For means of comparison, the measured dynamic deflected shape and the modeled shape of static membrane deflection are plotted in Figure 6.12 for a membrane actuator with 10 mm diameter. The deflected shape measured at the first resonance frequency qualitatively agrees well with the shape derived from the analytic model of static membrane actuator deflection that was introduced in chapter 3.

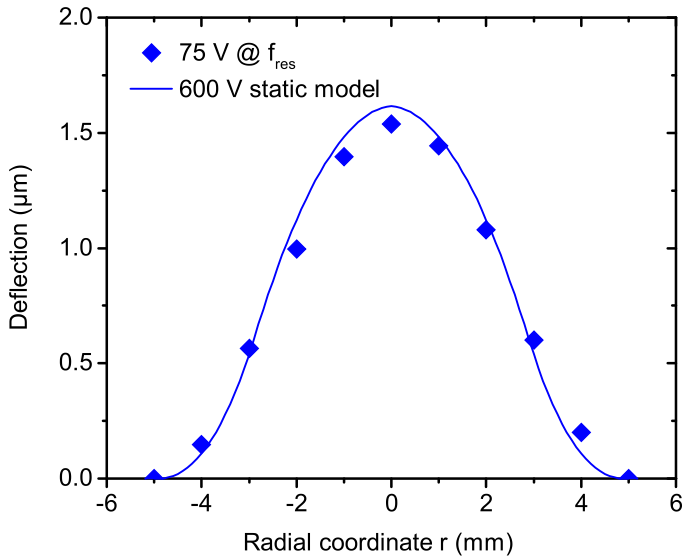

Figure 6.12 Comparison of measured deflected shape at resonance frequency and modeled deflected shape for a 10 mm-diameter membrane actuator.

6.3.2 Geometry-dependent dynamic deflection

For the application in a reciprocating membrane pump, driving membrane actuators at their first resonance frequency could be beneficial to generate large deflections at moderate driving voltages. Driving at the second resonance frequency yields no net volume change and is thus not applicable for a pumping function. Furthermore, the absolute deflection at the second resonance frequency is significantly lower than for the first resonance frequency. In order to investigate the large-signal resonant behavior, the actuators were driven by a

sinusoidal voltage at their previously determined first resonance frequency while the deflection amplitude was recorded. For the target application in portable devices for point-of-care diagnostics, low driving voltages would be beneficial to reduce the requirements for high-voltage electronics in the portable system. Therefore, moderate voltage amplitudes of 50 V to 100 V (peak-to-peak) were employed for the dynamic characterization of printed P(VDF-TrFE) actuators.

Figure 6.13 displays the measured dynamic deflection of cantilever actuators and provides the results from static actuator deflection (taken from Figure 6.2) for comparison. It can be clearly seen that driving at resonance frequency yields significantly higher deflections than static driving. For cantilevers with 15 mm length, approximately 315 µm deflection amplitude were measured when driven with 100 V voltage amplitude. Actuators with 10 mm length yield approximately 175 µm deflection amplitude at a driving voltage of 100 V. Similar to the static actuator behavior, the dependence of deflection amplitude on voltage is approximately linear. Correlation coefficients for a linear fit of $R^2 > 0.98$ were derived. The standard deviations of deflection amplitude increases slightly compared to static driving to values of 13% to 20%.

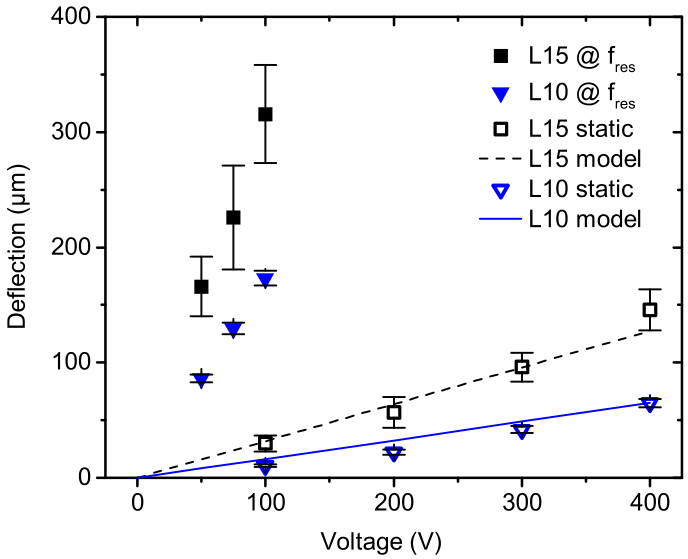

Figure 6.13 Deflection amplitudes of cantilever actuators driven at their respective resonance frequencies. Results from static deflection measurements are provided for comparison.

Similar trends were observed for membrane actuators driven at their respective resonance frequencies. The voltage-dependent dynamic as well as static deflection values (taken from Figure 6.3) are displayed in Figure 6.14.

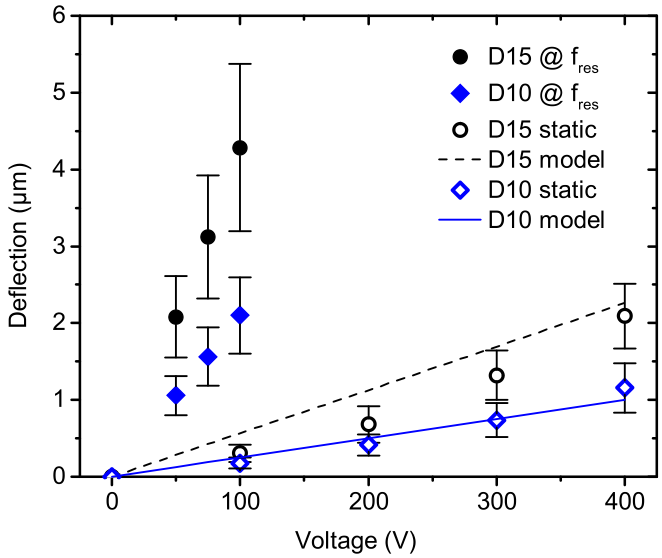

Figure 6.14 Deflection amplitude of membrane actuators driven at their respective resonance frequencies. Results from static deflection measurements are provided as a comparison.

When voltage amplitudes of 100 V were applied at the resonance frequency, deflection amplitudes of 2.1 µm and 4.3 µm were measured for membrane actuators with 10 mm and 15 mm diameter, respectively. Compared to static deflections this is a significant increase, considering the reduced driving voltages. Large correlation coefficients for a linear fit of the voltage-dependent deflection of $R^2 > 0.99$ were determined. The standard deviations remained in the same order of magnitude as during static deflection measurements. For membrane actuators driven at resonance frequency, deviations were found to be in the range of 20% to 30%.

6.3.3 Estimation of dynamic pump rate

The measurements of dynamic membrane deflection discussed in the previous sections serve as a basis for an estimate of the liquid pump rate in a micropump with a printed P(VDF-TrFE) actuator for operation at resonance frequency. These values support the analytically modeled quasi-static liquid pump rate values provided in section 3.4. As described in chapter 1, a reciprocating membrane pump consists of a pumping chamber, inlet and outlet valves, and an actuated membrane. When the membrane is deflected, the volume under the membrane will change. This volume change is converted to a net fluid flow from an inlet to an outlet channel by valves [14].

The surface profiles of deflected membrane actuators driven in air at their first resonance frequency were recorded using the scanning vibrometer setup. From these measurements, the deflection amplitude $\Delta z(r)$ along the membrane radius r was integrated

over the radius to calculate the volume change per cycle generated by the actuator (see equation (3.14)). The volume change in air was then calculated by multiplying the volume change per cycle with the driving frequency (see equation (3.15)). The resulting volume change in air for different driving voltages and membrane diameters is plotted in Figure 6.15. Measurements were performed on one sample per type of geometry. Error bars include the error percentage that was derived from membrane deflection measurements on similar samples.

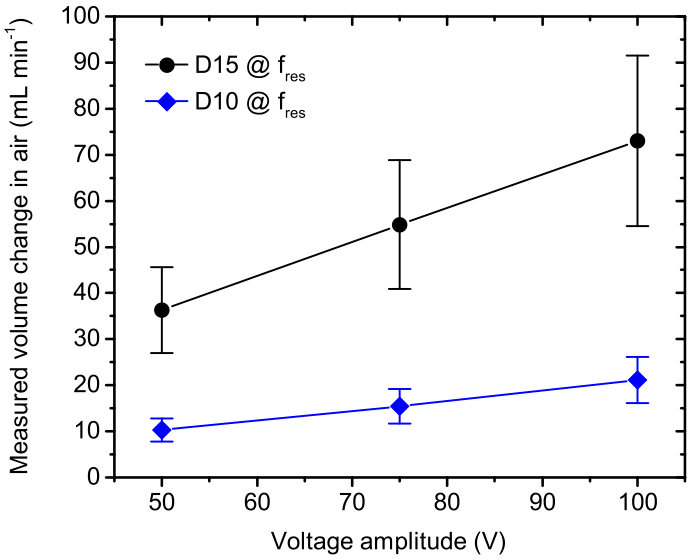

Figure 6.15 Measured volume change in air of membrane actuators with 10 mm and 15 mm diameter driven at resonance frequency.

For driving at resonance frequency with voltages of up to 100 V, volume changes in air of up to 10 mL min^{-1} and 73 ml min^{-1} were derived from measurements of membrane actuators with 10 mm and 15 mm diameter, respectively. It has to be noted that the actual liquid pump rate in a reciprocating membrane pump will be significantly lower than the volume change in air. As discussed along with the analytical modeling (section 3.4), an efficiency of the passive valves has to be taken into account, and furthermore the resonance frequency and deflection at resonance will decrease.

The efficiency factor η was estimated based on typical literature values and accounts for a valve direction sensitivity ($\eta_{valve} = 0.2$) [14]. Furthermore, for driving at resonance frequency, η includes a reduction of deflection caused by fluid loading ($\eta_{\Delta z} = 0.2$) [160] as well as fluid damping that leads to a reduced resonance frequency ($\eta_f = 0.25$) [123]. For resonant driving, this leads to an overall efficiency factor of $\eta = 0.01$. The resulting estimated liquid pump rates are displayed in Figure 6.16.

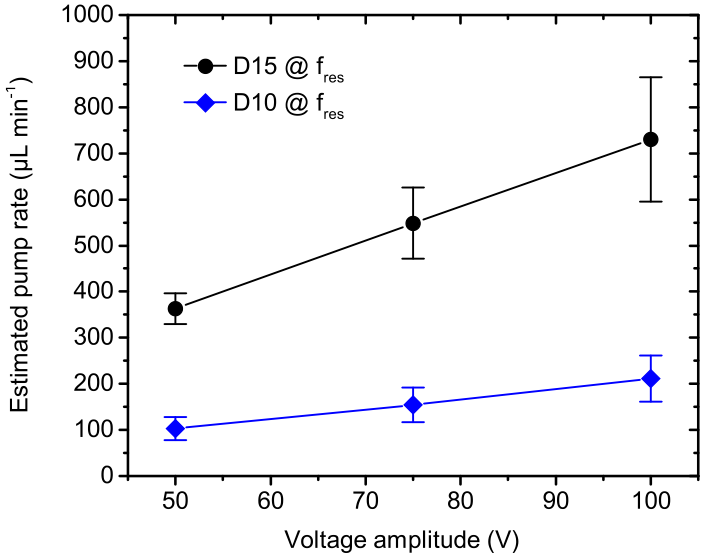

Figure 6.16 Estimation of liquid pump rate based on actuator deflection measurement in air.

For driving at resonance frequency with moderate driving voltages, relatively high pump rates of up to 100 µL min^{-1} and 730 µl min^{-1} were estimated for membrane actuators with 10 mm and 15 mm diameter, respectively. However, it has to be noted that these pump rates represent only estimates and do not include fluidic restrictions that can occur in a pump setup.

In summary, the dynamic actuator behavior was studied experimentally by laser scanning vibrometer measurements. The scaling of resonance frequency with actuator geometry was investigated for both cantilever and membrane actuators. The deflected shapes were visualized and the deflection of actuators driven at their first resonance frequency was measured for moderate voltage amplitudes of up to 100 V. The volume change generated when driving the actuators in air was measured, leading to estimates of liquid pump rates of several hundred µL min^{-1} in a pump demonstrator.

6.4 Device stability

Apart from the static and dynamic deflection behavior, the device stability is an important characteristic of all electromechanical, electrical or electronic devices. In the field of organic electronic devices this is of particular interest due to the fact that organic electronics is a relatively young topic. Furthermore, for active polymeric materials used in organic light-emitting devices or organic field-effect transistors, degradation is known to be a critical issue [25]. The target applications of actuators in this work are disposable microfluidic lab-on-a-chip systems for point-of-care applications. Typical times of operation in such

systems are in the range of few hours [173]. Therefore, the demands on device stability over a long lifetime are relatively low. However, it has to be investigated to which extent the device performance changes over lifetime. Therefore, the variation of actuator deflection and resonance frequency for a membrane actuator during cyclic operation was investigated. Another aspect that is of interest for cyclic operation of all piezoelectric materials especially with high driving voltages is the generation of heat due to dielectric losses that are associated to the polarization hysteresis [174]. Therefore, actuators under cyclic loads were imaged using an infrared camera. As a third aspect of device stability, the operation of printed P(VDF-TrFE) layers at elevated temperatures was investigated. For that purpose, ferroelectric hysteresis measurements were performed at different temperatures in order to set up thermal boundary conditions for operation of the samples.

6.4.1 Cyclic stability

For a study of the cyclic stability of printed P(VDF-TrFE) actuators, a membrane actuator with 10 mm diameter was operated in air at its first resonance frequency of 5.8 kHz and a voltage amplitude of 75 V continuously for 1.5×10^9 cycles, which is equivalent to 72 hours. During that test, deflection amplitude and resonance frequency were measured several times by vibrometer measurements. The results are plotted in Figure 6.17.

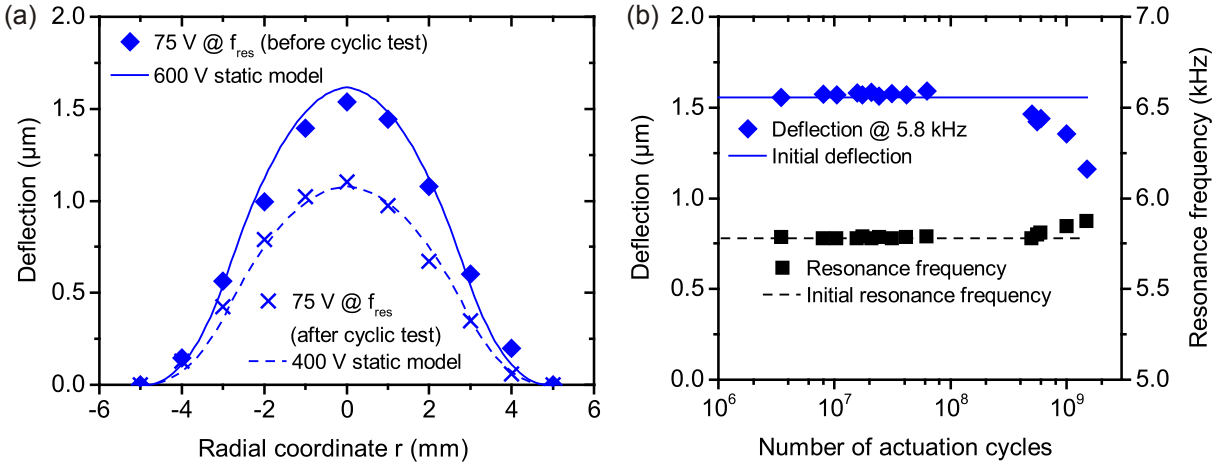

Figure 6.17 (a) Deflected shape of a 10 mm diameter actuator driven at resonance frequency before and after 1.5×10^9 actuation cycles compared to shapes derived from static analytic modeling. (b) Cyclic stability of a 10 mm diameter actuator driven at resonance frequency for 72 h. The initial values for deflection and resonance frequency are indicated by lines.

Within the first 6.2×10^7 cycles, which is equivalent to three hours of operation, no significant changes in deflection amplitude or resonance frequency are observed. This time of operation would be typical for applications in lab-on-a-chip systems [173]. For larger

numbers of cycles, a decrease in deflection and an increase in resonance frequency are observed. After 5×10^8 cycles and 1.5×10^9 cycles, the deflections are reduced to 94% and 75% of the initial deflection, respectively. These cycle numbers are equivalent to an operation time of 24 hours and 72 hours, respectively. The reduction in deflection indicates a certain loss of polarization or degradation of the active material. At the end of the cyclic stability tests, the resonance frequency was increased by 2% compared to the starting value. Before and after the cyclic stability test, the deflected shape of the actuators was recorded. The shapes are compared to analytically calculated shapes at equivalent static driving voltages in Figure 6.17 (a). Good agreement is achieved for modeled static driving voltages of 600 V before and 400 V after cyclic testing.

For the investigations of cyclic stability, the resonance frequency was determined and was set as a constant driving frequency throughout the measurements. This would also be a typical operation scheme in applications without closed-loop control of the driving frequency. As the actual resonance frequency changed during the investigations, the actuator was driven slightly off its resonance. This is expected to cause part of the reduction in deflection. In order to distinguish between that effect and actual degradation in actuator performance, the frequency-dependent normalized actuator deflection close to the resonance frequency is plotted in Figure 6.18 (a).

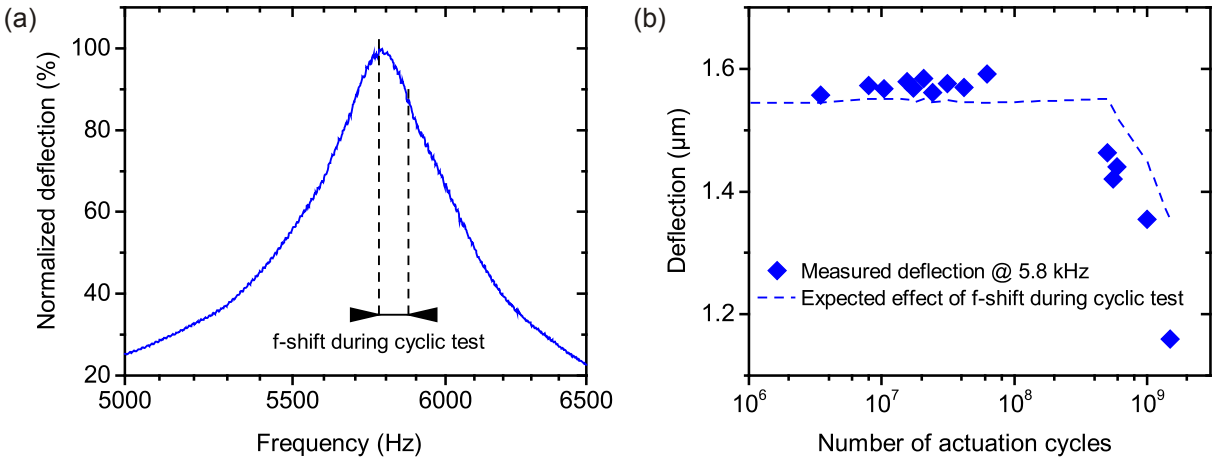

Figure 6.18 (a) Frequency-dependent membrane actuator deflection measured around the resonance frequency. The frequency shift observed during cyclic stability tests is indicated. (b) Expected effect of driving the actuator off its resonance frequency on deflection amplitude. Measured deflection is provided as a comparison.

Taking into account the measured change in resonance frequency, the expected reduced deflection amplitude is plotted in Figure 6.18 (b) and compared to the actual measured values. From that comparison it can be seen that driving the actuator off its resonance frequency is one factor that contributes to reduced deflection amplitudes. However,

this fact can only explain part of the measured decrease in deflection. The remaining part is attributed to polarization fatigue and damages within the P(VDF-TrFE) films that lead to a decrease in performance.

Although a certain decrease in performance was observed during cyclic stability investigations, this decrease occurred at relatively large cycle numbers. Within the target specifications for operation time, the performance remained mostly unchanged. In literature, the fatigue of P(VDF-TrFE) films for memory applications was recently investigated by Khan et al. [175]. The authors reported an "excellent polarization fatigue" of 80% retention after a total number of 10^6 cycles at a driving frequency of 1 kHz. Similar results were reported by Mao et al. [176]. A noticeable fatigue of the printed P(VDF-TrFE) films occurred only at larger numbers of cycles in this work. In summary, it was demonstrated that the printed P(VDF-TrFE) actuator can be assumed to be sufficiently robust for cyclic operation in single-use lab-on-a-chip systems.

6.4.2 Heat generation during cyclic operation

When piezoelectric actuators are operated at large fields, dielectric losses due to polarization hysteresis lead to energy dissipation within the piezoelectric layer. The actuator thus can heat up during operation, which can lead to undesired temperature changes e.g. on a microfluidic chip [174]. In order to quantify this effect for the inkjet printed P(VDF-TrFE) films, a membrane actuator with 15 mm diameter was operated at different driving conditions while the temperature distribution across the backside of the membrane was recorded using an infrared (IR) camera (FLIR T335, FLIR Systems, Inc., resolution 320 × 240 pixels, sensitivity < 50 mK).

Figure 6.19 shows photographs of the measurement setup (a-b) as well as an example thermogram (c). The membrane area is indicated by a dashed circle. Without electrical driving and using an emissivity of 0.95 (taken from the material database in the camera software), an average membrane temperature of approximately 25 °C was recorded. The areas that appear to have higher temperatures in Figure 6.19 (c) correspond to the aluminum sample mount, which would require different emissivity settings for correct analysis. For the actual measurements, only the temperature distribution on the membrane was analyzed, because the temperature change in the mount was assumed to be negligible.

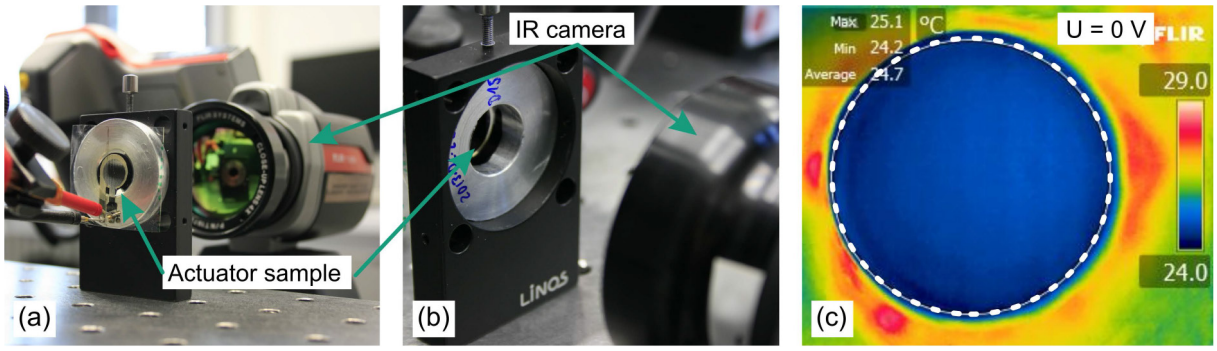

Figure 6.19 Infrared camera setup used for measurement of heat generation during cyclic operation of actuators (a-b). Thermogram recorded from the backside of an actuator membrane (c). Temperature distribution was analyzed on the PET membrane (indicated by dashed circle).

Figure 6.20 displays the time-dependent temperature change for different driving conditions. Generally, the temperature change reaches a steady-state within approximately 20 s to 40 s. Driving at resonance frequency with voltage amplitudes up to 200 V only leads to small temperature changes of up to 0.5 K. Large-signal sinusoidal driving at 600 V and a frequency of 30 Hz generates comparable temperature changes.

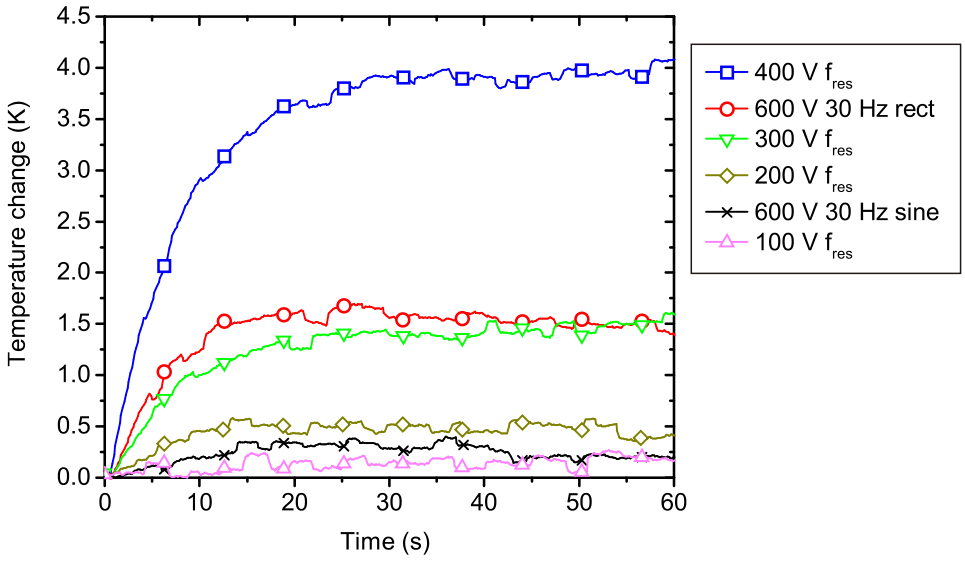

Figure 6.20 Time-dependent temperature change for different driving conditions of a membrane actuator measured by an infrared camera.

Resonant operation at large voltage amplitudes of 300 V and 400 V generates significantly higher temperature changes of 1.5 K and 4.2 K, respectively. Additionally, driving with a rectangular voltage of 600 V at a frequency of 30 Hz was performed, because this driving scheme was investigated in the actual pump demonstrator (see chapter 7). This leads to moderate temperature changes of approximately 1.7 K. Figure 6.21 displays thermograms for selected driving conditions.

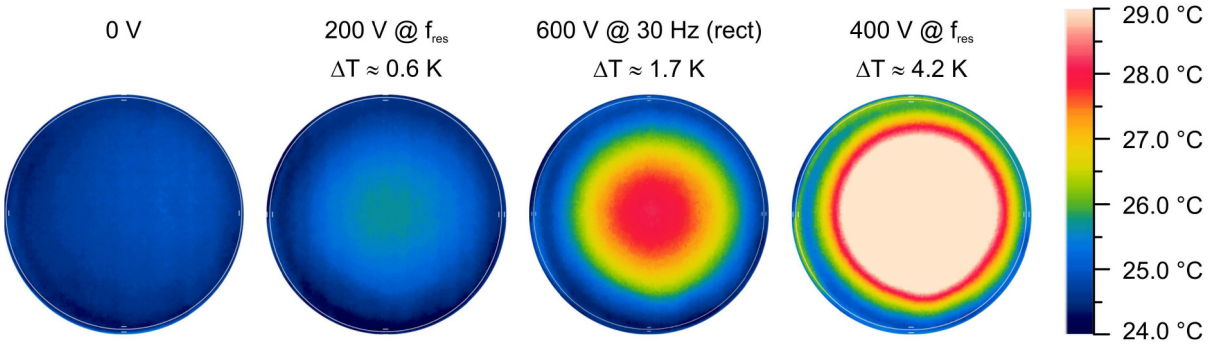

Figure 6.21 Steady-state thermograms of actuator backside for different electrical driving conditions.

Figure 6.22 plots the steady-state temperature change for all driving conditions that were investigated. Error bars indicate the noise of approximately 0.15 K that was present in the measurements. For most measurements, the temperature change remains below 2 K. Resonant driving at a large voltage amplitude of 400 V leads to a higher temperature change. These values confirm that dielectric losses lead to a certain generation of thermal energy. However, the temperature changes observed are relatively low and are not expected to pose a challenge in the target applications.

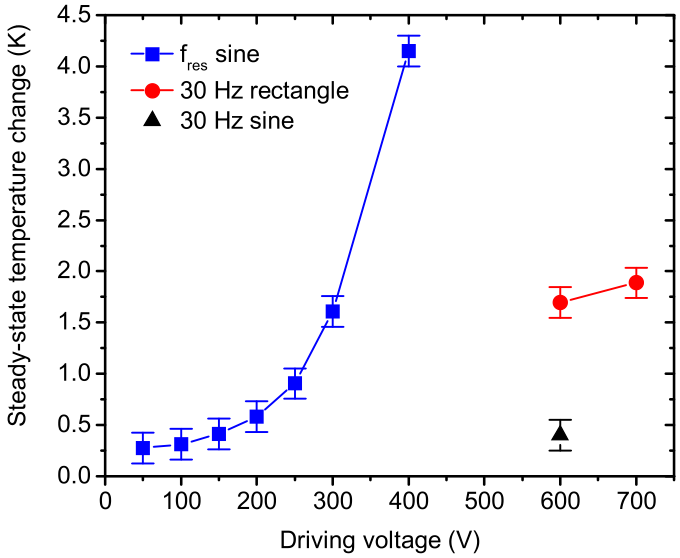

Figure 6.22 Steady-state temperature change for different driving conditions of a membrane actuator measured by an infrared camera.

6.4.3 Operation stability at elevated temperatures

Piezoelectric materials typically exhibit a Curie temperature, above which the piezoelectric effect is not present any more. For P(VDF-TrFE) copolymers, this transition occurs when the ferroelectric β-phase transforms into the paraelectric α-phase [17]. In chapter 5, the phase change was determined to occur at approximately 105 °C. For operation of the actuators, temperatures significantly below the Curie transition should be chosen to

ensure reliable behavior. In order to establish guidelines for operating temperatures, ferroelectric hysteresis loops of actuators were measured at different sample temperatures. For that purpose, a test pads for ferroelectric measurements was placed on a hotplate. Measurements of the ferroelectric hysteresis behavior were then performed at room temperature and in increments of 5 K up to a maximum temperature of 120 °C. Selected measurements are plotted in Figure 6.23.

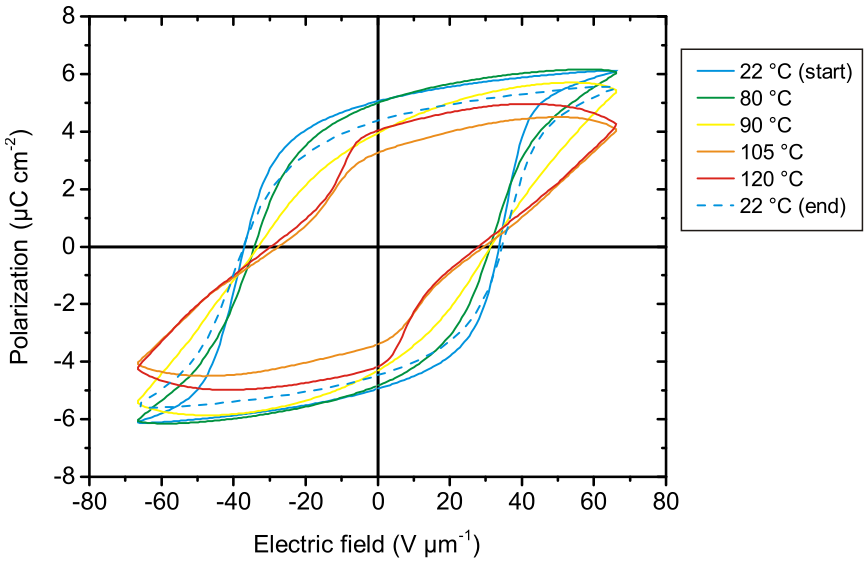

Figure 6.23 Polarization hysteresis loop for one printed P(VDF-TrFE) sample characterized at different operating temperatures. Up to temperatures of approximately 80 °C, the device behavior remains mostly unchanged. Higher temperatures lead to deformed hysteresis loops and should therefore be avoided during operation.

Distinct hysteresis curves with saturation polarizations of approximately 6 µC cm^{-2} and remanent polarizations of approximately 5 µC cm^{-2} were recorded at room temperature. For temperatures up to 80 °C, the hysteresis curves remain mostly unchanged when compared to the behavior at room temperature. The remanent polarization at 70 °C is 5.3 µC cm^{-2}, thus slightly higher than the room temperature value, which is assumed to be due to an improved polarizability at elevated temperatures [115]. For operating temperatures above 80 °C, the hysteresis loops change their shape significantly. With increasing temperature, more and more deformed loops were recorded that do not show distinct polarization saturation any more. When the sample was cooled from 120 °C down to room temperature and measured at room temperature again, distinct hysteresis loops are regained. It has to be noted that a lower remanent polarization was measured compared to the first measurement at room temperature. The main reason for this is assumed to be a different cooling rate than the one that was employed during initial processing and annealing of the printed P(VDF-TrFE) film.

From the operation tests at elevated temperatures, it is found that the samples show no significant change in electrical performance up to operating temperatures of approximately 80 °C. This temperature limit should be regarded as an absolute maximum temperature. In order to include a safety factor, typical operation temperatures of up to 50 °C are recommended to ensure consistent behavior.

To summarize the investigations on device stability, it could be demonstrated that the samples exhibit a good cyclic stability. Within typical operation times in disposable lab-on-a-chip systems, no significant degradation of the performance is expected. Furthermore, the heat dissipation in samples driven in resonance at large driving fields was studied. A certain temperature change in the samples is observed, but the absolute changes are in the range of 1 to 2 K and up to 4 K only for high voltages and resonant driving, which is considered not critical for the target application. As a third measure of device stability, the operation at elevated temperatures was investigated. Up to approximately 80 °C, no significant drop in performance is visible in ferroelectric hysteresis measurements. Thus, it is concluded that including a safety factor, operation at least up to temperatures of 50 °C should be possible. These combined characteristics should be considered for an application of the printed P(VDF-TrFE) films. For the target application in a micropump for disposable lab-on-a-chip systems, the device performance is considered sufficiently stable.

7 Micropump based on inkjet printed P(VDF-TrFE) actuators

In this chapter, the application of the inkjet printed P(VDF-TrFE) actuators that were characterized in the previous chapters in a micropump is demonstrated as a proof of concept. For that purpose, pump substrates were manufactured in PMMA and an aluminum alloy (RSA 905). The substrates were sealed with PET cover foils that exhibit a printed circular actuator. The pumps are designed as reciprocating membrane pumps with passive nozzle / diffuser valves. Two iterations of pump demonstrators were realized. Basic measurements of the pump rate under different driving conditions are presented. The design of the pump substrates is compatible with polymer replications technologies like injection molding or hot embossing and thus suitable for applications in polymer-based lab-on-a-chip systems.

7.1 Design of micropump demonstrator

Figure 7.1 shows a schematic view of the pump setups that were prepared in this work. Pump substrates were manufactured in PMMA and RSA 905 by precision milling. The lateral dimensions of the substrates are those of a standard microscopic glass slide (25.5×75.5 mm^2), which is also a typical chip size in microfluidic chips [12]. Into those substrates, a single fluidic channel with a width of 3 mm and a depth of 0.5 mm as well as a cylindrical pump chamber with a diameter of 15 mm were milled. Passive nozzle / diffuser valves were designed based on geometry recommendations by Olsson [14] while ensuring structure sizes that are compatible with manufacturing by milling. The valves were manufactured with a minimum opening width of 200 µm, an opening angle of 20° and a valve length of 3 mm.

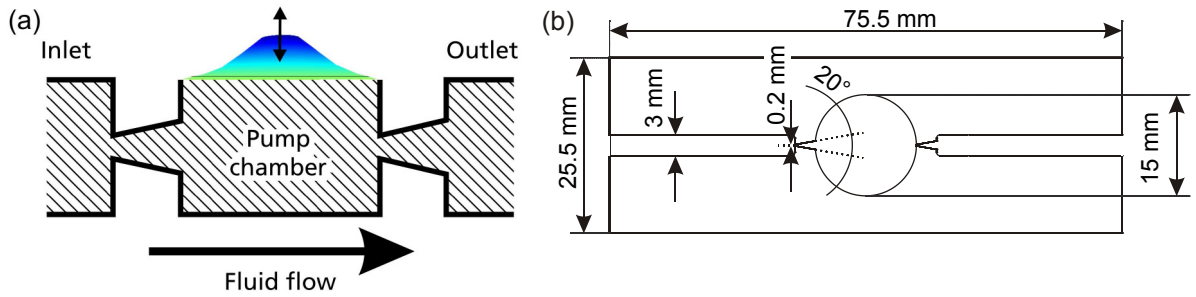

Figure 7.1 Schematic view (a) and dimensions (b) of the micropump setups that were manufactured and characterized in this work.

The main goal of this setup was the demonstration of a pumping function as a basic proof of concept. Therefore, no elaborate optimization of the valve design was carried out. As the pump substrate consists of simple 2.5-dimensional structures (two-dimensional structures with a constant depth) with moderate feature sizes, the design is fully compatible with standard polymer processing techniques typically employed to manufacture LOC systems.

7.2 Manufacturing of micropump demonstrators

Figure 7.2 shows photographs of pump substrates that were manufactured based on the design described above. The first iteration of a pump substrate was milled in PMMA (a-b). For that substrate, the paths of the milling tool are clearly visible on the sample and indicate a rough surface.

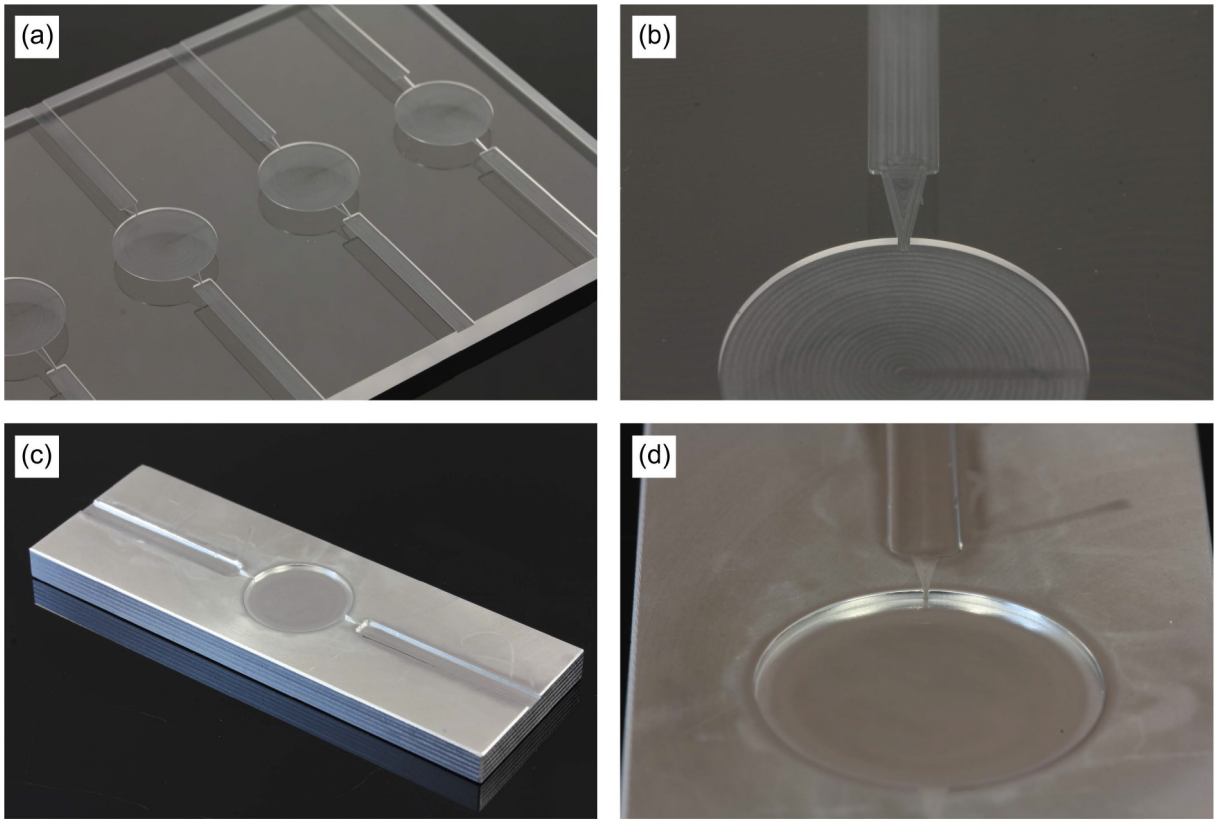

Figure 7.2 (a) Pump substrates milled in PMMA with different valve geometries and (b) detailed view of valve geometry. (c-d) Pump substrate milled and polished in an aluminum alloy (RSA 905).

A second iteration of a pump substrate was milled in an aluminum alloy (RSA 905) and is displayed in Figure 7.2 (c-d). For that iteration, the channels and pump chambers were polished manually after milling. The surface profile and roughness of pump substrates in PMMA and RSA 905 were measured using a tactile surface profilometer (Thalysurf PGI 1200, Taylor Hobson Ltd., UK). The results are plotted in Figure 7.3. The measured

channel depth in milled PMMA (a) and milled RSA 905 (b) are approximately 470 µm and 505 µm, respectively, which is close to the designed depth of 500 µm. The edge angle of approximately 50° in the plots occurs due to the size and shape of the measuring tip; the actual angle is close to 90° after milling.

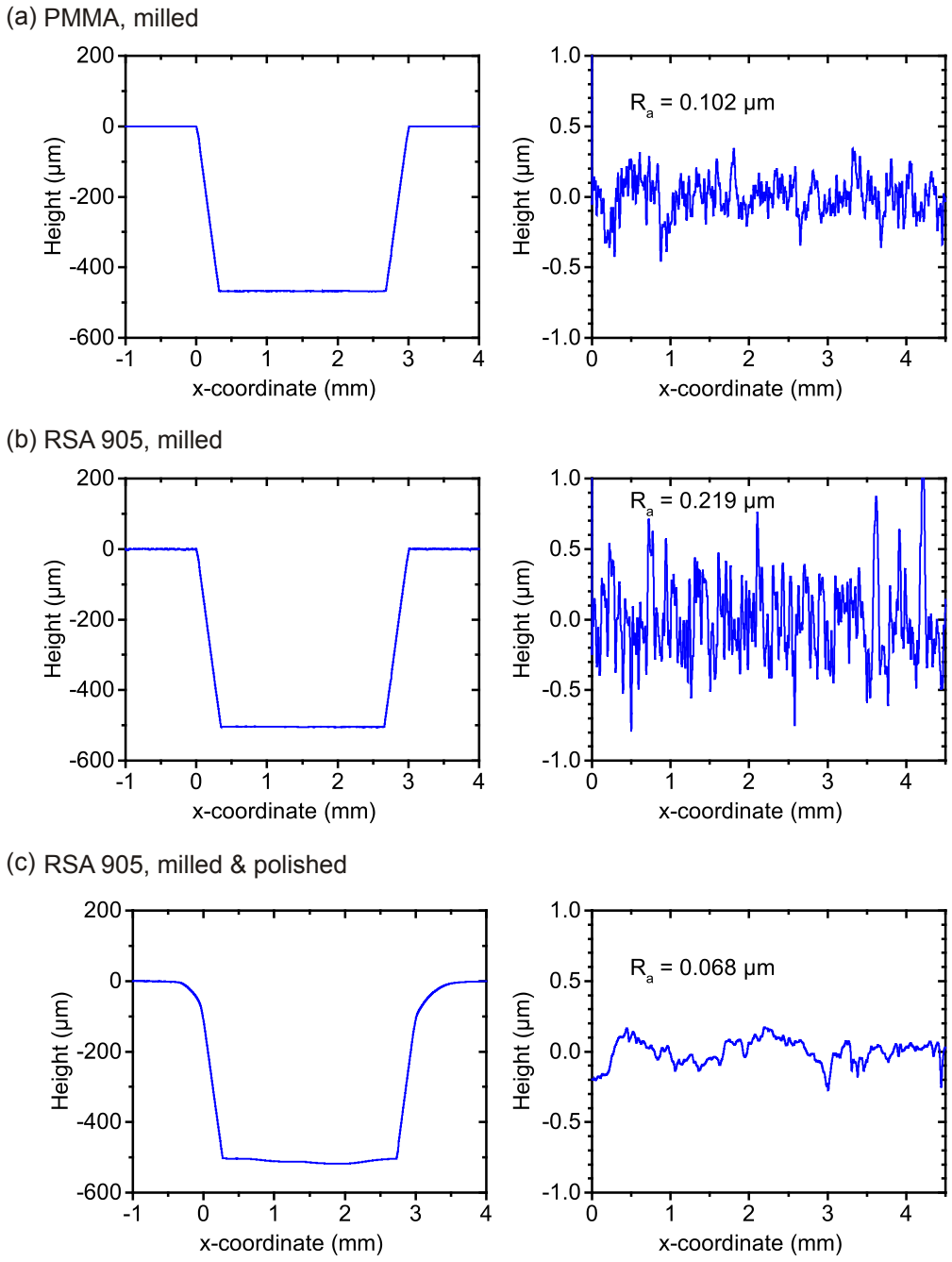

Figure 7.3 Surface profiles and roughness values R_a of three different pumping chambers: Milled PMMA (a), milled RSA 905 (b) and milled and polished RSA 905 (c). Channel profiles (left) and detailed views of pump chamber surfaces (right).

For milled PMMA, a surface roughness value of R_a = 0.102 µm (determined according to DIN EN ISO 4288:1998) is determined. Milled and unpolished samples made from

RSA 905 show an R_a value of 0.219 µm. Roughness is significantly reduced in polished RSA 905 (Figure 7.3 c). With that sample, an R_a value of 0.068 µm was measured. Due to the manual polishing process, rounded edges are visible in the channel profile.

Membrane actuators were first poled and then mounted on the pump substrates using cyanoacrylate adhesive, similar to the mounting procedure described in chapter 6. Mounting was performed manually. In order to aid alignment, single printed silver droplets around the membrane perimeter as alignment marks were included in the design of the bottom electrode. A readily processed pump demonstrator can be seen in Figure 7.4. The dead volume (volume of pump chamber + valve volume) of a pump demonstrator with a membrane diameter of 15 mm is approximately 90 µL.

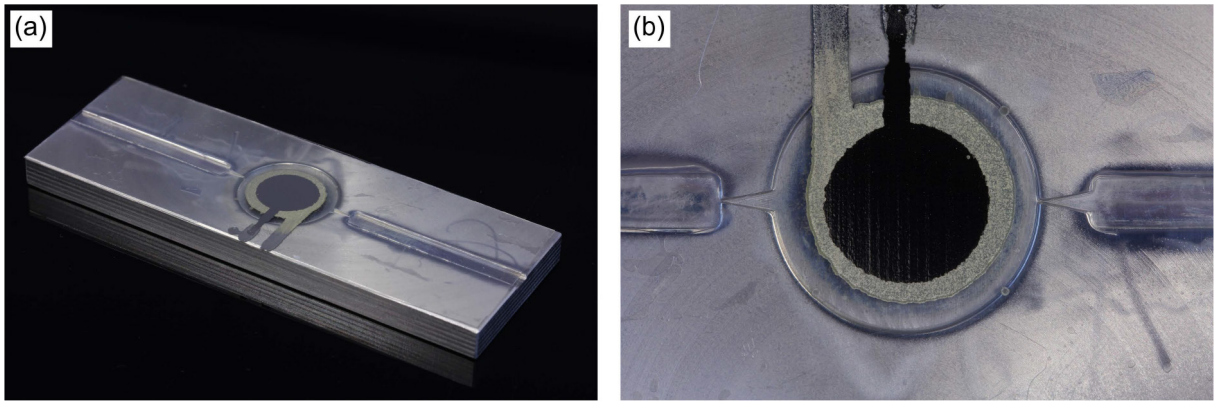

Figure 7.4 (a) Second iteration of micropump demonstrator (RSA 905, polished channels). (b) Detailed view of pump chamber.

7.3 Results and discussion

The liquid pump rate Q_l of the pump demonstrators was determined by analyzing videos recorded of the actuators during pumping. The volume change generated by the pump was calculated with the help of scale bars on the pump demonstrator. The pump rate was extracted based on the volume change that occurred between selected still images and the corresponding time difference. For the measurements, volume changes in the range of 10 µL to 15 µL were chosen. Depending on the pump rate, measurement times were in the range of 5 s to 60 s, which is large compared to the video frame rate of 25 frames per second. As a pumping medium, isopropanol was chosen due to its good wetting characteristics on all materials that it was in contact with, namely the PMMA or RSA 905 substrate and the PET cover foil.

A photograph of the first demonstrator iteration is provided in Figure 7.5. With this demonstrator a basic pump function could be demonstrated for quasi-static operation of the pump. At driving frequencies of 5 Hz to 10 Hz and a sinusoidal voltage with an amplitude of 600 V (peak-to-peak), low pump rates in the range of 6 µL min^{-1} to 8 µL min^{-1} were determined. Compared to the corresponding estimated quasi-static pump rates of approximately 50 µL min^{-1} provided in section 3.4, these measured pump rates are low. A possible reason for this behavior is a strong pinning of the fluid volume in the PMMA channels that was visible for the first demonstrator iteration. This pinning is expected to be due to the relatively large surface roughness of the milled PMMA. The effect was reduced slightly when tilting the pump demonstrator directly before characterization, which lead to wetting of the channels. For driving voltages below 600 V, the volume change was not large enough to overcome the surface pinning and thus no significant pump rate was observed.

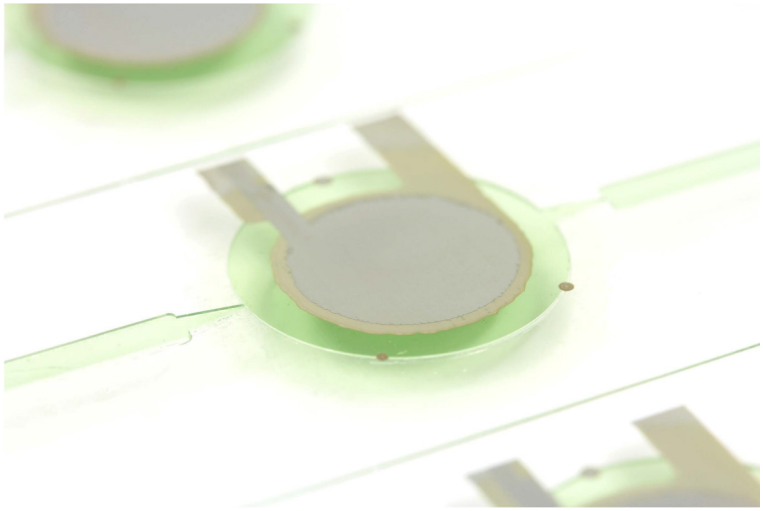

Figure 7.5 First iteration of micropump demonstrator (PMMA substrate, filled with colorant).

The pump performance was significantly higher for the second demonstrator iteration in which the pump chambers were first milled in RSA 905 and afterwards polished. Photographs of the pump demonstrator filled with a colorant for visualization of the channels are displayed in Figure 7.6. For that demonstrator, surface pinning effects could not be observed any more.

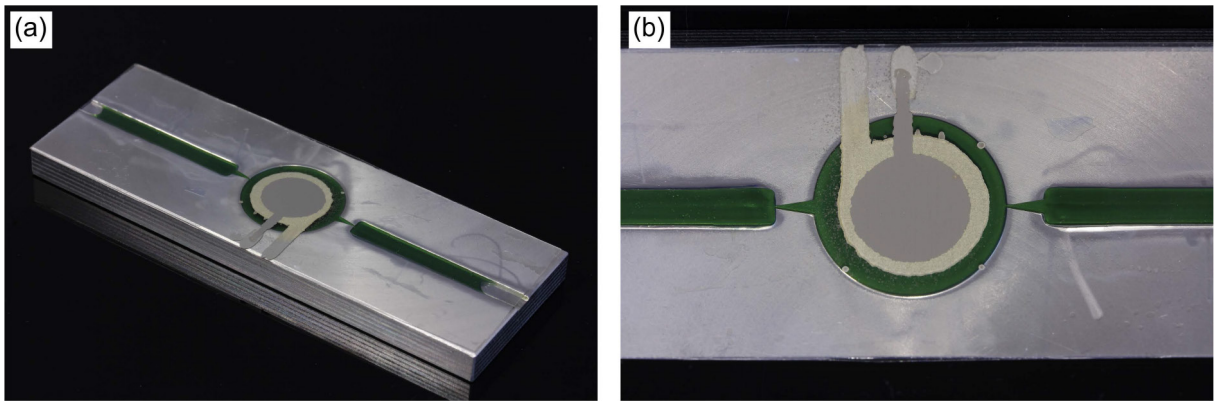

Figure 7.6 (a) Second iteration of micropump demonstrator (RSA 905, polished channels, channels filled with colorant). (b) Detailed view of pump chamber.

The pump rate was measured for different driving frequencies, voltages and backpressures. For characterization under different backpressures, the demonstrator was placed on a rotation stage with an angular resolution of 10 arcmin. The backpressure was then calculated based on the fluid volume in the setup, the angle-dependent normal force component and the cross-sectional area of the channel. Figure 7.7 shows the pump rate versus backpressure that was measured for the second demonstrator iteration.

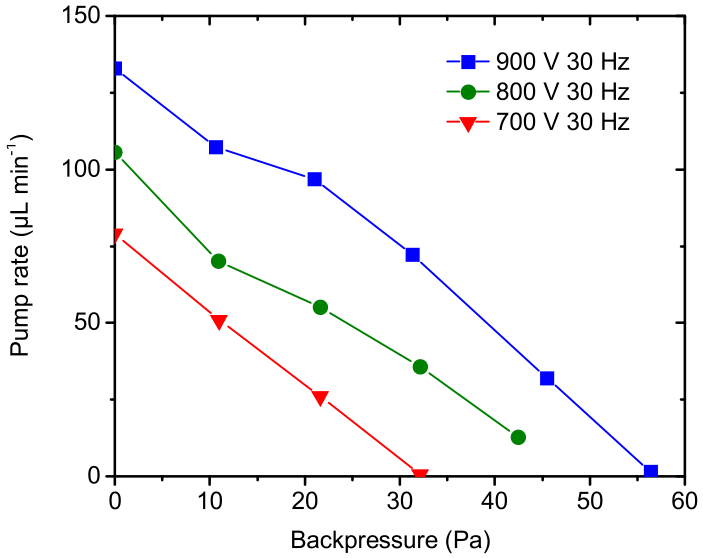

Figure 7.7 Pump rate versus backpressure for the second micropump demonstrator iteration pumping isopropanol.

When large driving voltages were employed, significant pump rates were measured. Driving with a rectangular voltage with an amplitude of 900 V at a frequency of 30 Hz results in a pump rate of approximately 130 µL min^{-1} at zero backpressure. When a backpressure is applied, the pump rate decreases linearly with increasing backpressure with a correlation coefficient for a linear fit of $R^2 \approx 0.98$. For 900 V driving voltage, a maximum backpressure

of 56 Pa leads to zero pump rate. With lower driving voltages down to 700 V, the pump rate and maximum backpressure are lower. An approximately linear dependency of both pump rate and maximum backpressure on driving voltage is observed. Below 600 V, no significant pump rate was observed, similar to the behavior of the first demonstrator iteration. This is attributed to the function of the nozzle / diffuser valves. The valve design employed in this work appears to have low direction sensitivity for low volume changes or flow gradients that occur for low driving voltages. The measured quasistatic pump rates for the second demonstrator iteration are in the same order of magnitude as the pump rates that were extracted from the quasistatic actuator model discussed in section 3.4. In the measurement, however, driving at voltages below 600 V did not lead to measurable pump rates.

The dependency of pump rate on driving frequency for a fixed voltage amplitude of 700 V (peak-to-peak) is plotted in Figure 7.8 (a). The curve exhibits a parabolic shape with a maximum pump rate at a frequency of 30 Hz above which the pump rate decreases significantly. Such characteristics have been described in literature for other pumps as well. Woias ([123], p. 31) stated that for low frequencies, "the pumping cycle is long enough for a full relaxation of the [...] pressure and flow transients." The decrease in pump rate for higher frequencies is attributed to insufficient relaxation and energy losses [123].

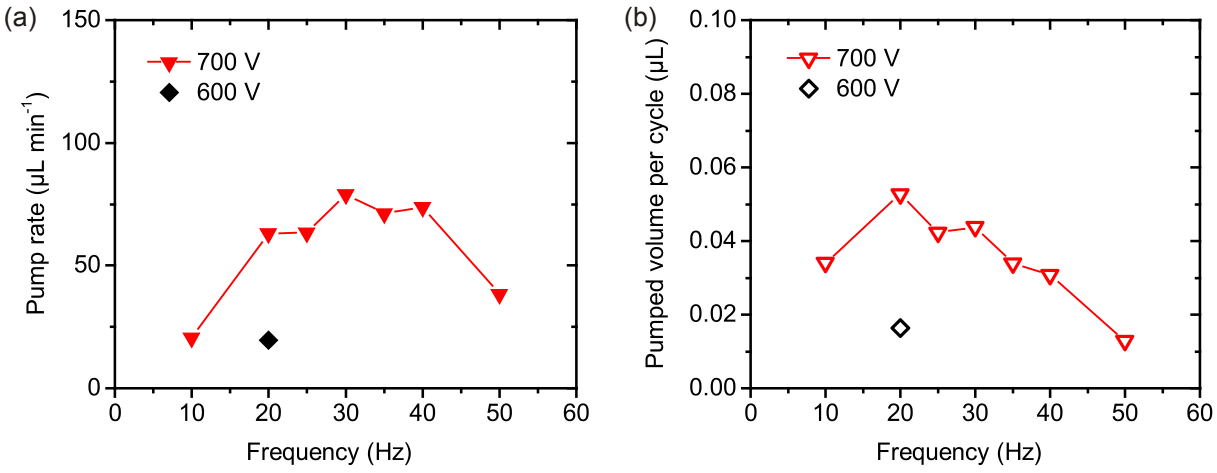

Figure 7.8 (a) Pump rate versus frequency at zero backpressure for the second micropump demonstrator iteration pumping isopropanol. (b) Pumped volume per cycle versus frequency.

The pumped volume per cycle derived from the frequency-dependent pump rate measurements is plotted in Figure 7.8 (b). Also here, a corner frequency exists where the pumped volume per cycle reaches a maximum. This maximum was measured at 20 Hz, which is lower than the frequency of maximum pump rate of 30 Hz. Between 20 Hz and 30 Hz, the

reduction in pumped volume per cycle is thus compensated by the higher frequency, leading to an overall increase in pump rate.

The electrical power required for driving a micropump is a critical factor especially for portable applications. During characterization of the second micropump demonstrator iteration, a maximum value of electrical power at maximum pump rate was measured to be approximately 12 mW. This is considered low enough for portable applications and comparable to typical values reported for other micropumps [125]. However, the large driving voltages required for quasistatic driving can be an issue for portable applications.

For an actual application of a micropump, the current demonstrator has two drawbacks. Firstly, larger backpressures than the ones realized (56 Pa) would be beneficial. Secondly, a directed fluid flow was observed only for large driving voltages above 600 V and for low driving frequencies. For portable devices in point-of-care applications, lower driving voltages would be preferred. Both drawbacks are believed to occur at least partially due to the valve setup. The actual blocking force of membrane actuators was found to be approximately 3.8 mN at a driving voltage of 600 V, as described in section 6.2.2. Dividing this force by the cross-sectional area of the fluid channel leads to a pressure of approximately 2500 Pa. This value would be a clear limitation due to actuator force and is significantly higher than the measured value of 56 Pa. Therefore, it is expected that with a more efficient valve design, the backpressure can still be tuned to higher values. One example would be to manufacture smaller valve throats (part of the valve with minimum opening size) or to include rounded inlets of the valves, as discussed by Olsson [14]. Alternatively, different valve concepts like active valves or passive moving valves could increase the backpressure [142]. Certainly, the stiffness of the PET membrane is low compared to ceramic or glass pump membranes, which also limits the actuator force and thus the backpressure.

The second issue of the relatively large driving voltages and low driving frequencies that yield large pump rates is tolerable for applications in lab-on-a-chip systems when the chips are inserted in larger but portable readout units that can provide sufficiently high voltages, which is nowadays typically the case [125]. However, for future hand-held LOC systems without separate readout units, lower driving voltages would be preferred [125]. In the pump demonstrators in this work, the pump rate dependency on voltage was linear above a threshold voltage of approximately 600 V. This implies that large volume and pressure changes are required to achieve a clear direction sensitivity of the specific nozzle / diffuser valve geometry. The presence of a threshold voltage also hinders driving of the actuators at

higher frequencies and moderate driving voltages. Therefore, the estimated pump rates for resonant driving of the micropump actuators discussed in section 6.3.3 could not yet be compared with actual measured values. A future more efficient valve design could improve the valve functionality also at lower volume changes.

To summarize, this chapter demonstrated the basic applicability of inkjet printed P(VDF-TrFE) actuators for pumping tasks in lab-on-a-chip systems. Pump rates of up to 130 $\mu L\,min^{-1}$ that were measured exceed the target range that was specified in the introduction of this thesis (10 $\mu L\,min^{-1}$ to 100 $\mu L\,min^{-1}$, chapter 1). These results are promising for lab-on-a-chip systems. It was found that polished channel surfaces lead to improved pump performance. The demonstrators were milled in PMMA and an aluminum alloy (RSA 905), but the pump design is compatible with large-scale polymer replication techniques like hot-embossing or injection molding. The current demonstrators show a significant pump performance only for large driving voltages and low driving frequencies, which is undesired for hand-held LOC systems. Furthermore, higher backpressures than those realized so far would be beneficial. These issues are attributed mostly to the valve design and have to be addressed in future work.

8 Conclusions and outlook

In this thesis, the first characterization of all inkjet printed piezoelectric polymer actuators based on P(VDF-TrFE) is presented. A novel process chain that consists of three inkjet printing and post-processing steps is established. Process temperatures are compatible with temperature-sensitive polymer substrates that are commonly used in disposable, polymer-based lab-on-a-chip systems. The process chain was employed to manufacture actuators in different geometries. Printed P(VDF-TrFE) actuators are characterized with respect to their piezoelectric d_{31} coefficients, remanent polarization P_{rem} as well as morphology for different thermal treatments of the as-printed P(VDF-TrFE) films for the first time here. The static and dynamic actuator performance is studied and good agreement with analytical models is achieved. Furthermore, a basic pumping function in a micropump demonstrator with an inkjet printed P(VDF-TrFE) actuator is characterized as a proof of concept.

Compared to the state-of-the-art, the process chain and the established knowledge about the actuator behavior and morphology of inkjet printed P(VDF-TrFE) films are novel. The results compare well with findings reported for other manufacturing approaches for P(VDF-TrFE) films and, in the future, can be transferred to design actuators for different applications as well as other piezoelectric devices. The low processing temperatures enable the direct integration of actuator functionalities into disposable, polymer-based lab-on-a-chip systems by cost-effective technologies. This would be challenging with conventional manufacturing techniques based on lithography and vacuum processes. Furthermore, the pump demonstrator presented in this work features an actuator that is printed directly on the cover foil that seals the underlying fluidic chip. Therefore, no additional joining step is necessary, which is required in most current micropumps where an actuator is manufactured separately and then attached to the pump membrane. The pump rates that were recorded are suitable for applications in LOC systems.

Analytical models for actuator behavior are adopted for basic cantilever and membrane actuators to predict the device performance. The influence of film thicknesses, lateral geometries and driving conditions is discussed and the models are employed to establish guidelines for sample preparation in this work. The manufacturing approach was employed to print a set of two silver electrodes and a P(VDF-TrFE) film onto a passive PET substrate. In order to ensure compatibility with temperature-sensitive polymer substrates,

combined low-temperature thermal and argon plasma-assisted treatments were performed for sintering the as-printed silver electrodes. The maximum temperature that was applied during post-treatments of the electrodes is 100 °C. Annealing of the P(VDF-TrFE) films requires temperatures above 110 °C. However, this is still compatible with relatively cost-effective polymer substrates like PC.

This work provides the first investigation of the electrical and electromechanical performance of printed P(VDF-TrFE) actuators with respect to different annealing steps applied to the as-printed P(VDF-TrFE) films. A clear influence of processing temperature on device performance is found with a critical minimum annealing temperature of approximately 110 °C which is required for reliable device performance. The electrical performance was characterized by ferroelectric hysteresis measurements. Maximum remanent polarization values of 5.8 μC cm^{-2} are determined for films annealed at 140 °C, which compares well with literature values for solution-processed P(VDF-TrFE) films [6]. Similar trends were observed for the electromechanical performance of printed P(VDF-TrFE) actuators. d_{31} coefficients are derived from measurements of cantilever deflection and are found to be up to 10 pm V^{-1}. For electrical and electromechanical measurements, the yield of samples was higher than 90% when using appropriate restrictions in electrical boundary conditions. Higher remanent polarization was observed for larger driving fields, however this lead to more frequent dielectric breakdown of the samples and was therefore avoided. The morphology and structure of samples annealed by different thermal treatments was investigated by means of differential scanning calorimetry, X-ray diffraction and atomic force microscopy. The investigations suggest an increased degree of crystallinity in the ferroelectric β-phase of P(VDF-TrFE) as well as larger crystalline domain sizes for samples that were annealed at higher temperatures and thus showed distinct piezoelectric behavior. These findings agree with previously published findings for bulk P(VDF-TrFE) and spin-coated P(VDF-TrFE) films [18,119]. The established knowledge about the correlation between morphology and device performance can be employed to design inkjet printed P(VDF-TrFE) actuators and other piezoelectric devices like sensors [7] or non-volatile memory elements [119], for which knowledge about d_{31} and P_{rem} is crucial as well.

The static and dynamic deflection behavior for cantilever and membrane actuators in different geometries was studied by optical measurements. Cantilever actuators with 15 mm length show significant static deflections of 145 μm at driving voltages of 400 V and more than 300 μm for driving at resonance frequency with a voltage amplitude of 100 V.

Membrane actuators show lower static and dynamic deflections of approximately 2 µm and 4 µm, respectively. Additionally, the force-deflection behavior was studied. The measurement results compare well with the analytically modeled values. The geometry-dependent resonance frequency and deflected shapes were recorded using a laser scanning vibrometer. Furthermore, the device stability for different driving conditions is studied. The cyclic stability was tested under resonant driving conditions for up to 1.5×10^9 cycles. Within typical operation times for the target application in disposable LOC systems, no significant change in performance is observed. A guideline for operating temperatures of the printed P(VDF-TrFE) elements is established based on ferroelectric hysteresis measurements that were run at different temperatures. Up to temperatures of approximately 80 °C, the remanent polarization remained mostly unchanged.

As an example application of printed P(VDF-TrFE) actuators, the first micropump with an inkjet printed P(VDF-TrFE) actuator is demonstrated in this thesis as a proof of concept. The pump is designed as a reciprocating membrane pump, in which a periodic movement of a membrane above a pumping chamber combined with valves induces a fluid flow in an underlying channel. Pump rates of up to 130 $\mu L\,min^{-1}$ are realized, which is suitable for applications in lab-on-a-chip systems. Pump substrates were manufactured in PMMA and an aluminum alloy with geometries that are suitable for future manufacturing by polymer replication techniques like injection molding. Currently the demonstrator exhibits a low backpressure and requires high driving voltages. These drawbacks are attributed mostly to the function of the valve geometries employed and will be addressed in future work.

The findings reported in this thesis can be used as a guideline for designing different devices based on printed P(VDF-TrFE) films in the future. The provided analytical models along with the device characterization are suitable for estimating the performance of printed P(VDF-TrFE) actuators for applications other than pumping tasks, like positioning of microoptical elements. Furthermore, the process chain that is introduced can be used to manufacture also piezoelectric sensors or non-volatile memories. The discussed relationship between annealing temperature, device performance and morphology of the P(VDF-TrFE) films can be employed to set up appropriate process conditions that represent a trade-off between compatibility with temperature-sensitive polymer substrates and device performance.

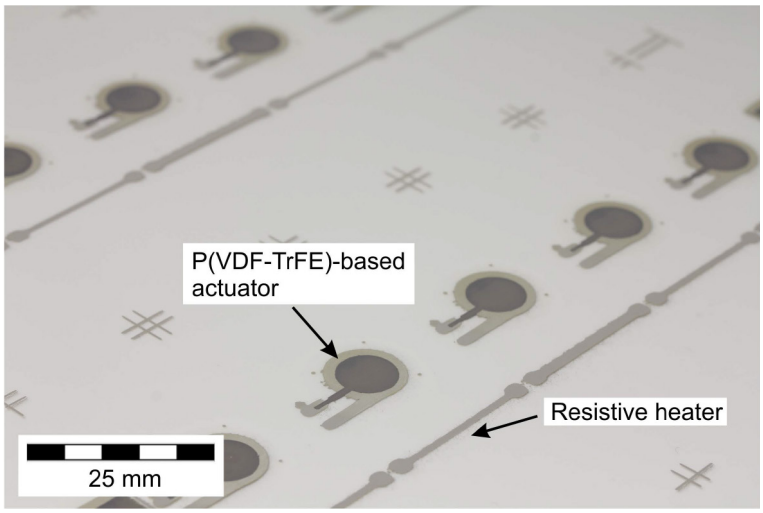

Figure 8.1 Outlook for further function integration in lab-on-a-chip systems: Membrane actuator combined with a resistive heating element.

Additionally, the manufacturing approach allows the combination with further functionalities for LOC systems along with pump actuators. Cost-effective function integration in LOC systems is considered a promising application of additive manufacturing techniques. When using the cover foil of a microfluidic chip as a basis, no hybrid integration of several separate components is required. As a first step towards this, inkjet printed resistive heating elements integrated on one common substrate with membrane actuators are depicted in Figure 8.1. The distribution of fluids across the channels of a LOC system along with the ability to apply defined temperatures represent key functionalities in LOC systems and are the basis for on-chip reactions like DNA analysis by polymerase chain reaction [19]. Apart from pumps and heating elements, printed organic light sources and detectors could enable on-chip fluorescent detection. This way, functionalities that are usually realized by separate external components could be implemented on a single chip in a cost-effective way and realize more complex on-chip reactions.

References

[1] M. Singh, H. M. Haverinen, P. Dhagat, G. E. Jabbour, Inkjet printing-process and its applications, Adv. Mater. 22 (6) (2010) 673–685.

[2] R. R. Søndergaard, M. Hösel, F. C. Krebs, Roll-to-roll fabrication of large area functional organic materials, J. Polym. Sci., Part B: Polym. Phys. 51 (1) (2013) 16–34.

[3] G. Helke, K. Lubitz, Piezoelectric PZT ceramics, in: W. Heywang, K. Lubitz, W. Wersing (Eds.), Piezoelectricity, Evolution and Future of a Technology, Vol. 114, Springer Berlin Heidelberg, 2008, pp. 89–130.

[4] Y. Bar-Cohen, Electroactive Polymer (EAP) Actuators as Artificial Muscles: Reality, Potential, and Challenges, Second edition, Vol. PM136, SPIE Press Monograph, 2004.

[5] S. Bauer, F. Bauer, Piezoelectric polymers and their applications, in: W. Heywang, K. Lubitz, W. Wersing (Eds.), Piezoelectricity, Evolution and Future of a Technology, Vol. 114, Springer Berlin Heidelberg, 2008, pp. 157–177.

[6] M. Zirkl, A. Haase, A. Fian, H. Schön, C. Sommer, G. Jakopic, G. Leising, B. Stadlober, I. Graz, N. Gaar, R. Schwödiauer, S. Bauer-Gogonea, S. Bauer, Low-voltage organic thin-film transistors with high-k nanocomposite gate dielectrics for flexible electronics and optothermal sensors, Adv. Mater. 19 (17) (2007) 2241–2245.

[7] M. Zirkl, A. Sawatdee, U. Helbig, M. Krause, G. Scheipl, E. Kraker, P. A. Ersman, D. Nilsson, D. Platt, P. Bodö, S. Bauer, G. Domann, B. Stadlober, An all-printed ferroelectric active matrix sensor network based on only five functional materials forming a touchless control interface, Adv. Mater. 23 (18) (2011) 1–6.

[8] A. Manz, N. Graber, H. Widmer, Miniaturized total chemical analysis systems: A novel concept for chemical sensing, Sensor Actuat. B-Chem. 1 (1-6) (1990) 244–248.

[9] L. Gervais, N. de Rooij, E. Delamarche, Microfluidic chips for point-of-care immunodiagnostics, Adv. Mater. 23 (24) (2011) H151–H176.

[10] H. Becker, C. Gärtner, Polymer microfabrication technologies for microfluidic systems, Anal. Bioanal. Chem. 390 (2008) 89–111.

[11] J. W. Judy, Microelectromechanical systems (MEMS): fabrication, design and applications, Smart Mater. Struct. 10 (6) (2001) 1115–1134.

[12] Microfludic ChipShop GmbH homepage, Lab-on-a-Chip Catalogue 03/2014, <www.microfluidic-chipshop.eu/Download/Lab-on-a-Chip%20Catalogue_032014.pdf> (accessed 23.07.2014).

[13] D. J. Laser, J. G. Santiago, A review of micropumps, J. Micromech. Microeng. 14 (6) (2004) R35–R64.

[14] A. Olsson, Valve-less diffuser micropumps, Ph.D. thesis, Royal Institute of Technology Stockholm, Sweden (1998).

[15] S. Zhang, B. Neese, K. Ren, B. Chu, F. Xia, T. Xu, S. Tadigadapa, Q. Wang, Q. M. Zhang, F. Bauer, Relaxor ferroelectric polymers, thin film devices, and ink-jet microprinting for thin film device fabrication, Ferroelectrics 342 (1) (2006) 43–56.

[16] J. Perelaer, U. S. Schubert, Novel approaches for low temperature sintering of inkjet-printed inorganic nanoparticles for roll-to-roll (R2R) applications, J. Mater. Res. 28 (4) (2013) 564–573.

[17] F. Baltá-Calleja, A. González Arche, T. A. Ezquerra, C. Santa Cruz, F. Batallán, B. Frick, E. López Cabarcos, Structure and properties of ferroelectric copolymers of poly(vinylidene) fluoride, in: H.-G. Zachmann (Ed.), Structure in Polymers with Special Properties, Springer-Verlag, 1993, pp. 1–48.

[18] D. Mao, B. E. Gnade, M. A. Quevedo-Lopez, Ferroelectric properties and polarization switching kinetic of poly (vinylidene fluoride-trifluoroethylene) copolymer, in: M. Lallart (Ed.), Ferroelectrics - Physical Effects, InTech Europe, 2011, pp. 77–100.

[19] C. Zhang, D. Xing, Y. Li, Micropumps, microvalves, and micromixers within PCR microfluidic chips: Advances and trends, Biotechnol. Adv. 25 (5) (2007) 483–514.

[20] Z. Bao, Y. Feng, A. Dodabalapur, V. R. Raju, A. J. Lovinger, High-performance plastic transistors fabricated by printing techniques, Chem. Mater. 9 (6) (1997) 1299–1301.

[21] B. A. Ridley, B. Nivi, J. M. Jacobson, All-inorganic field effect transistors fabricated by printing, Science 286 (5440) (1999) 746–749.

[22] H. Sirringhaus, T. Kawase, R. H. Friend, T. Shimoda, M. Inbasekaran, W. Wu, E. P. Woo, High-resolution inkjet printing of all-polymer transistor circuits, Science 290 (5499) (2000) 2123–2126.

[23] T. Kawase, H. Sirringhaus, R. H. Friend, T. Shimoda, All-polymer thin film transistors fabricated by high-resolution ink-jet printing, in: Proc. International Electron Devices Meeting, 2000, pp. 623–626.

[24] D. Tobjörk, R. Österbacka, Paper electronics, Adv. Mater. 23 (17) (2011) 1935–1961.

[25] H. Sirringhaus, Reliability of organic field-effect transistors, Adv. Mater. 21 (38-39) (2009) 3859–3873.

[26] S. Mihm, Print your next PC, in: MIT Technology Review, Vol. 11/12, 2000.

[27] Optomec homepage, datasheet of Aerosol Jet 300 series deposition system <http://www.optomec.com/printed-electronics/aerosol-jet-printers/> (accessed 23.07.2014).

[28] Microdrop GmbH Homepage, Microdrop dispenser heads, <http://www.microdrop.de/Microdrop_Dispenser_Heads.html> (accessed 23.07.2014).

[29] L. Rayleigh, On the instability of jets, P. Lond. Math. Soc. 10 (1878) 4–13.

[30] J. Perelaer, Microstructures prepared via inkjet printing and embossing techniques, Ph.D. thesis, Eindhoven University of Technology, The Netherlands (2009).

[31] H. P. Le, Progress and trends in ink-jet printing technology, J. Imaging Sci. Techn. 42 (1) (1998) 49–62.

[32] P. Calvert, Inkjet printing for materials and devices, Chem. Mater. 13 (10) (2001) 3299–3305.

[33] B. de Gans, P. C. Duineveld, U. S. Schubert, Inkjet printing of polymers: State of the art and future developments, Adv. Mater. 16 (3) (2004) 203–213.

[34] J. G. Korvink, P. J. Smith, D.-Y. Shin (Eds.), Inkjet-Based Micromanufacturing, Wiley-VCH Verlag GmbH & Co. KGaA, 2012.

[35] S. B. Fuller, E. J. Wilhelm, J. M. Jacobson, Ink-jet printed nanoparticle microelectromechanical systems, J. Microelectromech. Syst. 11 (1) (2002) 54–60.

[36] L. Yang, A. Rida, R. Vyas, M. Tentzeris, RFID tag and RF structures on a paper substrate using inkjet-printing technology, IEEE T. Microw. Theory 55 (12) (2007) 2894–2901.

[37] J. Shinar, R. Shinar, Organic light-emitting devices (OLEDs) and OLED-based chemical and biological sensors: An overview, J. Phys. D: Appl. Phys. 41 (13) (2008) 133001.

[38] C. Zhong, C. Duan, F. Huang, H. Wu, Y. Cao, Materials and devices toward fully solution processable organic light-emitting diodes, Chem. Mater. 23 (3) (2011) 326–340.

[39] S. Lilliu, M. Böberl, M. Sramek, S. F. Tedde, J. E. Macdonald, O. Hayden, Inkjet-printed organic photodiodes, Thin Solid Films 520 (1) (2011) 610–615.

[40] L. L. Lavery, G. L. Whiting, A. C. Arias, All ink-jet printed polyfluorene photosensor for high illuminance detection, Org. Electron. 12 (4) (2011) 682–685.

[41] G. Azzellino, A. Grimoldi, M. Binda, M. Caironi, D. Natali, M. Sampietro, Fully inkjet-printed organic photodetectors with high quantum yield, Adv. Mater. 25 (47) (2013) 6829–6833.

[42] A. Teichler, R. Eckardt, S. Hoeppener, C. Friebe, J. Perelaer, A. Senes, M. Morana, C. J. Brabec, U. S. Schubert, Combinatorial screening of polymer:fullerene blends for organic solar cells by inkjet printing, Adv. Energy Mater. 1 (1) (2011) 105–114.

[43] R. Søndergaard, M. Hösel, D. Angmo, T. T. Larsen-Olsen, F. C. Krebs, Roll-to-roll fabrication of polymer solar cells, Mater. Today 15 (1-2) (2012) 36–49.

[44] J. Leppäniemi, M. Aronniemi, T. Mattila, A. Alastalo, M. Allen, H. Seppä, Printed WORM memory on a flexible substrate based on rapid electrical sintering of nanoparticles, IEEE T. Electron Dev. 58 (1) (2011) 151–159.

[45] U. S. Bhansali, M. Khan, H. Alshareef, Organic ferroelectric memory devices with inkjet-printed polymer electrodes on flexible substrates, Microelectron. Eng. 105 (2013) 68–73.

[46] B. Li, S. Santhanam, L. Schultz, M. Jeffries-EL, M. C. Iovu, G. Sauvé, J. Cooper, R. Zhang, J. C. Revelli, A. G. Kusne, J. L. Snyder, T. Kowalewski, L. E. Weiss, R. D. McCullough, G. K. Fedder, D. N. Lambeth, Inkjet printed chemical sensor array based on polythiophene conductive polymers, Sensor Actuat. B-Chem. 123 (2) (2007) 651–660.

[47] J. Jang, J. Ha, J. Cho, Fabrication of water-dispersible polyaniline-poly(4-styrenesulfonate) nanoparticles for inkjet-printed chemical-sensor applications, Adv. Mater. 19 (13) (2007) 1772–1775.

[48] A. M. J. van den Berg, A. W. M. de Laat, P. J. Smith, J. Perelaer, U. S. Schubert, Geometric control of inkjet printed features using a gelating polymer, J. Mater. Chem. 17 (7) (2007) 677–683.

[49] R. D. Deegan, O. Bakajin, T. F. Dupont, G. Huber, S. R. Nagel, T. A. Witten, Capillary flow as the cause of ring stains from dried liquid drops, Nature 389 (6653) (1997) 827–829.

[50] D. Soltman, V. Subramanian, Inkjet-printed line morphologies and temperature control of the coffee ring effect, Langmuir 24 (5) (2008) 2224–2231.

[51] P. Buffat, J.-P. Borel, Size effect on the melting temperature of gold particles, Phys. Rev. A 13 (6) (1976) 2287–2298.

[52] J. Chung, S. Ko, N. R. Bieri, C. P. Grigoropoulos, D. Poulikakos, Conductor microstructures by laser curing of printed gold nanoparticle ink, Appl. Phys. Lett. 84 (5) (2004) 801–803.

[53] S. H. Ko, H. Pan, C. P. Grigoropoulos, C. K. Luscombe, J. M. J. Fréchet, D. Poulikakos, All-inkjet-printed flexible electronics fabrication on a polymer substrate by low-temperature high-resolution selective laser sintering of metal nanoparticles, Nanotechnology 18 (34) (2007) 345202.

[54] B. Polzinger, F. Schoen, V. Matic, J. Keck, H. Willeck, W. Eberhardt, H. Kueck, UV-sintering of inkjet-printed conductive silver tracks, in: Proc. IEEE Nano, 2011, pp. 201–204.

[55] S. Farnsworth, K. M. Rawson, K. Schroder, D. Pope, Evaluation of tool for processing metallic conductive inks on low temperature substrates, in: Proc. International Symposium on Microelectronics, 2009.

[56] N. Marjanovic, J. Hammerschmidt, J. Perelaer, S. Farnsworth, I. Rawson, M. Kus, E. Yenel, S. Tilki, U. S. Schubert, R. R. Baumann, Inkjet printing and low temperature sintering of CuO and CdS as functional electronic layers and Schottky diodes, J. Mater. Chem. 21 (35) (2011) 13634–13639.

[57] J. Perelaer, R. Abbel, S. Wünscher, R. Jani, T. van Lammeren, U. S. Schubert, Roll-to-roll compatible sintering of inkjet printed features by photonic and microwave exposure: From non-conductive ink to 40% bulk silver conductivity in less than 15 seconds, Adv. Mater. 24 (19) (2012) 2620–2625.

[58] M. L. Allen, M. Aronniemi, T. Mattila, A. Alastalo, K. Ojanperä, M. Suhonen, H. Seppä, Electrical sintering of nanoparticle structures, Nanotechnology 19 (17) (2008) 175201.

[59] M. Allen, A. Alastalo, M. Suhonen, T. Mattila, J. Leppäniemi, H. Seppä, Contactless electrical sintering of silver nanoparticles on flexible substrates, IEEE T. Microw. Theory 59 (5) (2011) 1419–1429.

[60] I. Reinhold, C. E. Hendriks, R. Eckardt, J. M. Kranenburg, J. Perelaer, R. R. Baumann, U. S. Schubert, Argon plasma sintering of inkjet printed silver tracks on polymer substrates, J. Mater. Chem. 19 (21) (2009) 3384–3388.

[61] V. Bromberg, S. Ma, F. D. Egitto, T. J. Singler, Highly conductive lines by plasma-induced conversion of inkjet-printed silver nitrate traces, J. Mater. Chem. C 1 (41) (2013) 6842–6849.

[62] S. Wünscher, S. Stumpf, A. Teichler, O. Pabst, J. Perelaer, E. Beckert, U. S. Schubert, Localized atmospheric plasma sintering of inkjet printed silver nanoparticles, J. Mater. Chem. 22 (47) (2012) 24569–24576.

[63] S. Wünscher, S. Stumpf, J. Perelaer, U. S. Schubert, Towards single-pass plasma sintering: Temperature influence of atmospheric pressure plasma sintering of silver nanoparticle ink, J. Mater. Chem. C 2 (9) (2014) 1642–1649.

[64] J. Perelaer, B.-J. de Gans, U. S. Schubert, Ink-jet printing and microwave sintering of conductive silver tracks, Adv. Mater. 18 (16) (2006) 2101–2104.

[65] M. Grouchko, A. Kamyshny, C. F. Mihailescu, D. F. Anghel, S. Magdassi, Conductive inks with a "built-in" mechanism that enables sintering at room temperature, ACS Nano 5 (4) (2011) 3354–3359.

[66] J. Olkkonen, J. Leppäniemi, T. Mattila, K. Eiroma, Sintering of inkjet printed silver tracks with boiling salt water, J. Mater. Chem. C 2 (18) (2014) 3577–3582.

[67] L. E. Cross, W. Heywang, Introduction, in: W. Heywang, K. Lubitz, W. Wersing (Eds.), Piezoelectricity, Evolution and Future of a Technology, Springer Berlin Heidelberg, 2008, pp. 1–5.

[68] S. O. R. Moheimani, Accurate and fast nanopositioning with piezoelectric tube scanners: Emerging trends and future challenges, Rev. Sci. Instrum. 79 (7) (2008) 071101.

[69] E. Fujii, R. Takayama, K. Nomura, A. Murata, T. Hirasawa, A. Tomozawa, S. Fujii, T. Kamada, H. Torii, Preparation of (001)-oriented Pb(Zr,Ti)O3 thin films and their piezoelectric applications, IEEE T. Ultrason. Ferr. 54 (12) (2007) 2431–2431.

[70] S. Gebhardt, L. Seffner, F. Schlenkrich, A. Schönecker, PZT thick films for sensor and actuator applications, J. Eur. Ceram. Soc. 27 (2007) 4177–4180.

[71] V. Walter, P. Delobelle, P. L. Moal, E. Joseph, M. Collet, A piezo-mechanical characterization of PZT thick films screen-printed on alumina substrate, Sensor Actuat. A-Phys. 96 (2-3) (2002) 157–166.

[72] T. Wang, B. Derby, Ink-jet printing and sintering of PZT, J. Am. Ceram. Soc. 88 (8) (2005) 2053–2058.

[73] J. Madden, N. Vandesteeg, P. Anquetil, P. Madden, A. Takshi, R. Pytel, S. Lafontaine, P. Wieringa, I. Hunter, Artificial muscle technology: Physical principles and naval prospects, IEEE J. Oceanic Eng. 29 (3) (2004) 706–728.

[74] F. Carpi, E. Smela (Eds.), Biomedical Applications of Electroactive Polymer Actuators, John Wiley & Sons, Ltd, 2009.

[75] Y. Osada, H. Okuzaki, H. Hori, A polymer gel with electrically driven motility, Nature 355 (6357) (1992) 242–244.

[76] D. Kaneko, J. P. Gong, Y. Osada, Polymer gels as soft and wet chemomechanical systems-an approach to artificial muscles, J. Mater. Chem. 12 (8) (2002) 2169–2177.

[77] C.-A. Dai, C.-J. Chang, A.-C. Kao, W.-B. Tsai, W.-S. Chen, W.-M. Liu, W.-P. Shih, C.-C. Ma, Polymer actuator based on PVA/PAMPS ionic membrane: Optimization of ionic transport properties, Sensor Actuat. A-Phys. 155 (1) (2009) 152–162.

[78] G. M. Spinks, G. Alici, S. McGovern, B. Xi, G. G. Wallace, Conjugated polymer actuators: Fundamentals, in: F. Carpi, E. Smela (Eds.), Biomedical Applications of Electroactive Polymer Actuators, John Wiley & Sons, Ltd, 2009, pp. 193–227.

[79] J. Tangorra, P. Anquetil, T. Fofonoff, A. Chen, M. D. Zio, I. Hunter, The application of conducting polymers to a biorobotic fin propulsor, Bioinspr. Biomim. 2 (2) (2007) S6–S17.

[80] R. Izquierdo, F. Lefevre, S. Schougaard, M. Packirisam, A. Acharya, Integration of polypyrrole microactuators and organic optoelectronic devices for lab-on-chip applications, in: IEEE I. C. Elect. Circ., 2009, pp. 639–642.

[81] R. H. Baughman, C. Cui, A. A. Zakhidov, Z. Iqbal, J. N. Barisci, G. M. Spinks, G. G. Wallace, A. Mazzoldi, D. De Rossi, A. G. Rinzler, O. Jaschinski, S. Roth, M. Kertesz, Carbon nanotube actuators, Science 284 (5418) (1999) 1340–1344.

[82] H. Kawai, The piezoelectricity of poly (vinylidene fluoride), Jpn. J. Appl. Phys. 8 (7) (1969) 975–976.

[83] H. S. Nalwa (Ed.), Ferroelectric Polymers: Chemistry: Physics, and Applications, CRC Press, 1995.

[84] T. R. Howarth, K. M. Rittenmyer, Transduction applications, in: H. S. Nalwa (Ed.), Ferroelectric Polymers: Chemistry: Physics, and Applications, CRC Press, 1995, pp. 735–770.

[85] Robert Bosch GmbH, Vorrichtung zur Ermittlung des Betriebsverhaltens eines Einspritzventils, DE Patent 10 2007 063 103 A1 (2009).

[86] B. Ameduri, From vinylidene fluoride (VDF) to the applications of VDF-containing polymers and copolymers: Recent developments and future trends, Chem. Rev. 109 (12) (2009) 6632–6686.

[87] Q. M. Zhang, V. Bharti, X. Zhao, Giant electrostriction and relaxor ferroelectric behavior in electron-irradiated poly(vinylidene fluoride-trifluoroethylene) copolymer, Science 280 (5372) (1998) 2101–2104.

[88] W. Lehmann, H. Skupin, C. Tolksdorf, E. Gebhard, R. Zentel, P. Kruger, M. Losche, F. Kremer, Giant lateral electrostriction in ferroelectric liquid-crystalline elastomers, Nature 410 (6827) (2001) 447–450.

[89] R. Pelrine, R. Kornbluh, Q. Pei, J. Joseph, High-speed electrically actuated elastomers with strain greater than 100%, Science 287 (5454) (2000) 836–839.

[90] R. Pelrine, R. Kornbluh, G. Kofod, High-strain actuator materials based on dielectric elastomers, Adv. Mater. 12 (16) (2000) 1223–1225.

[91] R. Kornbluh, R. Heydt, R. Pelrine, Dielectric elastomer actuators: Fundamentals, in: F. Carpi, E. Smela (Eds.), Biomedical Applications of Electroactive Polymer Actuators, John Wiley & Sons, Ltd, 2009, pp. 385–393.

[92] S. Rosset, H. Shea, Flexible and stretchable electrodes for dielectric elastomer actuators, Appl. Phys. A-Mater. 110 (2) (2013) 281–307.

[93] H. F. Schlaak, M. Jungmann, M. Matysek, P. Lotz, Novel multilayer electrostatic solid state actuators with elastic dielectric, in: Proc. SPIE, Vol. 5759, 2005, pp. 121–133.

[94] R. Pelrine, R. Kornbluh, J. Joseph, R. Heydt, Q. Pei, S. Chiba, High-field deformation of elastomeric dielectrics for actuators, Mater. Sci. Eng. C 11 (2) (2000) 89–100.

[95] U. Kim, J. Kang, C. Lee, H. Y. Kwon, S. Hwang, H. Moon, J. C. Koo, J.-D. Nam, B. H. Hong, J.-B. Choi, H. R. Choi, A transparent and stretchable graphene-based actuator for tactile display, Nanotechnology 24 (14) (2013) 145501.

[96] RP-Acoustics e.K. homepage, <http://rp-acoustics.de/english/PVDF_e.htm> (accessed 23.07.2014).

[97] Force Technology homepage, <http://www.forcetechnology.com/en/Menu/Products/Hydrophones/> (accessed 23.07.2014).

[98] Precision Acoustics homepage, <http://acoustics.co.uk/products/ultrasonic-transducers/pvdf-transducers/> (accessed 23.07.2014).

[99] Z. Li, Z. Cheng, Piezoelectric and electrostrictive polymer actuators: Fundamentals, in: F. Carpi, E. Smela (Eds.), Biomedical Applications of Electroactive Polymer Actuators, John Wiley & Sons, Ltd, 2009, pp. 317–334.

[100] H. Ohigashi, K. Omote, T. Gomyo, Formation of "single crystalline films" of ferroelectric copolymers of vinylidene fluoride and trifluoroethylene, Appl. Phys. Lett. 66 (24) (1995) 3281–3283.

[101] K. Omote, H. Ohigashi, K. Koga, Temperature dependence of elastic, dielectric, and piezoelectric properties of "single crystalline" films of vinylidene fluoride trifluoroethylene copolymer, J. Appl. Phys. 81 (6) (1997) 2760–2769.

[102] I. Seo, D. Zou, Electromechanical applications, in: H. S. Nalwa (Ed.), Ferroelectric polymers: chemistry, physics, and applications, Marcel Dekker, Inc., 1995, pp. 699–734.

[103] Arkema Inc. Homepage, Kynar PVDF Properties table <http://americas.kynar.com/export/sites/kynar-americas/.content/medias/downloads/literature/kynar-kynar-flex-pvdf-performance-chracteristics.pdf> (accessed 23.07.2014).

[104] H. Wang, Q. M. Zhang, L. E. Cross, A. O. Sykes, Piezoelectric, dielectric, and elastic properties of poly(vinylidene fluoride/trifluoroethylene), J. Appl. Phys. 74 (5) (1993) 3394–3398.

[105] Solvay Specialty Polymers S.p.A. homepage, Properties of solvene EAP, <http://www.solvayplastics.com/sites/solvayplastics/EN/specialty_polymers/Specialties/Pages/solvene_EAP.aspx> (accessed 23.07.2014).

[106] PI Ceramic GmbH, Material data of PZT materials, <http://piceramic.com/products/piezoelectric-materials.html?eID=dam_frontend_push&docID=5258> (accessed 23.07.2014).

[107] T. Kaura, R. Nath, M. M. Perlman, Simultaneous stretching and corona poling of PVDF films, J. Phys. D: Appl. Phys. 24 (10) (1991) 1848–1852.

[108] Y. Tajitsu, H. Ogura, A. Chiba, T. Furukawa, Investigation of switching characteristics of vinylidene fluoride/trifluoroethylene copolymers in relation to their structures, Jpn. J. Appl. Phys. 26 (1987) 554–560.

[109] J. F. Legrand, Structure and ferroelectric properties of P(VDF-TrFE) copolymers, Ferroelectrics 91 (1) (1989) 303–317.

[110] H. Xu, J. Zhong, X. Liu, J. Chen, D. Shen, Ferroelectric and switching behavior of poly(vinylidene fluoride-trifluoroethylene) copolymer ultrathin films with polypyrrole interface, Appl. Phys. Lett. 90 (9) (2007) 092903.

[111] N. Shingne, Morphology and crystal orientation of ferroelectric P(VDF-ran-TrFE) nanostructures in porous aluminium oxide, Ph.D. thesis, University of Halle, Germany (2011).

[112] M.-C. Garcia-Gutierrez, A. Linares, I. Martin-Fabiani, J. J. Hernandez, M. Soccio, D. R. Rueda, T. A. Ezquerra, M. Reynolds, Understanding crystallization features of P(VDF-TrFE) copolymers under confinement to optimize ferroelectricity in nanostructures, Nanoscale 5 (2013) 6006–6012.

[113] A. J. Lovinger, T. Furukawa, G. Davis, M. Broadhurst, Crystallographic changes characterizing the curie transition in three ferroelectric copolymers of vinylidene fluoride and trifluoroethylene: 1. as-crystallized samples, Polymer 24 (10) (1983) 1225–1232.

[114] A. Kumar, M. M. Periman, Simultaneous stretching and corona poling of PVDF and P(VDF-TriFE) films. II, J. Phys. D: Appl. Phys. 26 (3) (1993) 469–473.

[115] Y. Higashihata, J. Sako, T. Yagi, Piezoelectricity of vinylidene fluoride-trifluoroethylene copolymers, Ferroelectrics 32 (1) (1981) 85–92.

[116] G. Teyssèdre, A. Bernes, C. Lacabanne, DSC and TSC study of a VDF/TrFE copolymer, Thermochim. Acta 226 (1993) 65–75.

[117] G. Teyssèdre, C. Lacabanne, Compositional variation of the glass transition and the associated dielectric relaxation in copolymers of vinylidene fluoride and trifluoroethylene, Polymer 36 (19) (1995) 3641–3648.

[118] S.-W. Hahm, D.-Y. Khang, Crystallization and microstructure-dependent elastic moduli of ferroelectric P(VDF-TrFE) thin films, Soft Matter 6 (22) (2010) 5802–5806.

[119] D. Mao, M. Quevedo-Lopez, H. Stiegler, B. Gnade, H. Alshareef, Optimization of poly(vinylidene fluoride-trifluoroethylene) films as non-volatile memory for flexible electronics, Org. Electron. 11 (5) (2010) 925–932.

[120] A. Teichler, J. Perelaer, U. S. Schubert, Inkjet printing of organic electronics - comparison of deposition techniques and state-of-the-art developments, J. Mater. Chem. C 1 (10) (2013) 1910–1925.

[121] S. Zhang, Z. Liang, Q. Wang, Q. Zhang, Ink-jet printing of ferroelectric poly(vinylidene fluoride-trifluoroethylene) copolymers, in: Mater. Res. Soc. Symp. Proc., Vol. 889, 2006, pp. 167–186.

[122] A. C. Hübler, M. Bellmann, G. C. Schmidt, S. Zimmermann, A. Gerlach, C. Haentjes, Fully mass printed loudspeakers on paper, Org. Electron. 13 (11) (2012) 2290–2295.

[123] P. Woias, Micropumps - past, progress and future prospects, Sensor Actuat. B-Chem. 105 (1) (2005) 28–38.

[124] B. Iverson, S. Garimella, Recent advances in microscale pumping technologies: a review and evaluation, Microfluid. Nanofluid. 5 (2) (2008) 145–174.

[125] F. Amirouche, Y. Zhou, T. Johnson, Current micropump technologies and their biomedical applications, Microsyst. Technol. 15 (5) (2009) 647–666.

[126] M. Koch, N. Harris, A. G. Evans, N. M. White, A. Brunnschweiler, A novel micromachined pump based on thick-film piezoelectric actuation, Sensor Actuat. A-Phys. 70 (1998) 98–103.

[127] M. Richter, R. Linnemann, P. Woias, Robust design of gas and liquid micropumps, Sensor Actuat. A-Phys. 68 (1998) 480–486.

[128] H. Andersson, W. van der Wijngaart, P. Nilsson, P. Enoksson, G. Stemme, A valve-less diffuser micropump for microfluidic analytical systems, Sensor Actuat. B-Chem. 72 (3) (2001) 259–265.

[129] N.-T. Nguyen, T.-Q. Truong, A fully polymeric micropump with piezoelectric actuator, Sensor Actuat. B-Chem. 97 (1) (2004) 137–143.

[130] R. Zengerle, J. Ulrich, S. Kluge, M. Richter, A. Richter, A bidirectional silicon micropump, Sensor Actuat. A-Phys. 50 (1-2) (1995) 81–86.

[131] C. Yamahata, C. Lotto, E. Al-Assaf, M. Gijs, A PMMA valveless micropump using electromagnetic actuation, Microfluid. Nanofluid. 1 (3) (2005) 197–207.

[132] S. Santra, P. Holloway, C. D. Batich, Fabrication and testing of a magnetically actuated micropump, Sensor Actuat. B-Chem. 87 (2) (2002) 358–364.

[133] M. Schüller, J. Nestler, A. Morschhauser, T. Otto, T. Gessner, Low cost valveless magnetic micropumps suitable for array applications, in: Proc. Actuator 2008, Bremen, 2008.

[134] W. K. Schomburg, J. Vollmer, B. Bustgens, J. Fahrenberg, H. Hein, W. Menz, Microfluidic components in LIGA technique, J. Micromech. Microeng. 4 (4) (1994) 186–191.

[135] O. C. Jeong, S. S. Yang, Fabrication and test of a thermopneumatic micropump with a corrugated p+ diaphragm, Sensor Actuat. A-Phys. 83 (1-3) (2000) 249–255.

[136] E. Makino, T. Mitsuya, T. Shibata, Fabrication of TiNi shape memory micropump, Sensor Actuat. A-Phys. 88 (3) (2001) 256–262.

[137] S. Lee, K. J. Kim, Design of IPMC actuator-driven valve-less micropump and its flow rate estimation at low Reynolds numbers, Smart Mater. Struct. 15 (4) (2006) 1103–1109.

[138] F. Xia, S. Tadigadapa, Q. Zhang, Electroactive polymer based microfluidic pump, Sensor Actuat. A-Phys. 125 (2) (2006) 346–352.

[139] S. Zeng, C.-H. Chen, J. C. Mikkelsen Jr., J. G. Santiago, Fabrication and characterization of electroosmotic micropumps, Sensor Actuat. B-Chem. 79 (2-3) (2001) 107–114.

[140] P. Wang, Z. Chen, H.-C. Chang, A new electro-osmotic pump based on silica monoliths, Sensor Actuat. B-Chem. 113 (1) (2006) 500–509.

[141] R. Fobel, A. E. Kirby, A. H. C. Ng, R. R. Farnood, A. R. Wheeler, Paper microfluidics goes digital, Adv. Mater. 26 (18) (2014) 2838–2843.

[142] K. W. Oh, C. H. Ahn, A review of microvalves, J. Micromech. Microeng. 16 (5) (2006) R13–R39.

[143] G. Waibel, J. Kohnle, R. Cernosa, M. Storz, M. Schmitt, H. Ernst, H. Sandmaier, R. Zengerle, T. Strobelt, Highly integrated autonomous microdosage system, Sensor Actuat. A-Phys. 103 (2-3) (2003) 225–230.

[144] G.-H. Feng, E. S. Kim, Micropump based on PZT unimorph and one-way parylene valves, J. Micromech. Microeng. 14 (4) (2004) 429–435.

[145] M. Koch, A. Evans, A. Brunnschweiler, Simulation and fabrication of micromachined cantilever valves, Sensor Actuat. A-Phys. 62 (1-3) (1997) 756–759.

[146] T. Gerlach, Microdiffusers as dynamic passive valves for micropump applications, Sensor Actuat. A-Phys. 69 (2) (1998) 181–191.

[147] A. Olsson, G. Stemme, E. Stemme, Numerical and experimental studies of flat-walled diffuser elements for valve-less micropumps, Sensor Actuat. A-Phys. 84 (1-2) (2000) 165–175.

[148] K. Uchino (Ed.), Ferroelectric Devices, Marcel Dekker, Inc., 2000.

[149] D. DeVoe, A. Pisano, Modeling and optimal design of piezoelectric cantilever microactuators, J. Microelectromech. Syst. 6 (3) (1997) 266–270.

[150] E. Ellis, Low-cost bimorph mirrors in adaptive optics, Ph.D. thesis, University of London, UK (1999).

[151] J. Smits, W.-s. Choi, The constituent equations of piezoelectric heterogeneous bimorphs, IEEE T. Ultrason. Ferr. 38 (3) (1991) 256–270.

[152] M. Weinberg, Working equations for piezoelectric actuators and sensors, J. Microelectromech. Syst. 8 (4) (1999) 529–533.

[153] C. Hsueh, Thermal stresses in elastic multilayer systems, Thin Solid Films 418 (2) (2002) 182–188.

[154] Goodfellow GmbH homepage, Material properties table PET, <http://www.goodfellow.com/PDF/TAB302G.pdf> (accessed 23.07.2014).

[155] W. Y. Ng, B. Ploss, H. L. W. Chan, F. Shin, C.-L. Choy, Pyroelectric properties of PZT/P(VDF-TrFE) 0-3 composites, in: Proc. 12th IEEE Int. Symp. Appl. Ferroel., Vol. 2, 2000, pp. 767–770.

[156] W. Dax, N. Drozd, W.-D. Gläser, H. Itschner, G. Kotsch, J. Slaby, A. Weiß, K. Zeimer (Eds.), Tabellenbuch für Metalltechnik, Handwerk und Technik GmbH, 2012.

[157] J. Park, D. J. Lee, S. J. Kim, J. H. Oh, Dynamic characteristics measurements of inkjet-printed thin films of nanosilver suspensions on a flexible plastic substrate, J. Micromech. Microeng. 19 (9) (2009) 095021.

[158] T. Zhang, Q.-M. Wang, Performance evaluation of a valveless micropump driven by a ring-type piezoelectric actuator, IEEE T. Ultrason. Ferr. 53 (2) (2006) 463–473.

[159] P. J. Schreurs, Linear plate bending and laminate theory (lecture notes Design Tools, Eindhoven University of Technology), <http://www.mate.tue.nl/~piet/edu/dnt/pdf/doc/docplb.pdf> (accessed 23.07.2014).

[160] G.-H. Feng, E.-S. Kim, Piezoelectrically actuated dome-shaped diaphragm micropump, J. Microelectromech. Syst. 14 (2) (2005) 192–199.

[161] Harima Chemicals Inc. homepage, <www.harima.co.jp/en/products/electronics/pdf/E_P21.pdf> (accessed 23.07.2014).

[162] F. M. Wolf, J. Perelaer, S. Stumpf, D. Bollen, F. Kriebel, U. S. Schubert, Rapid low-pressure plasma sintering of inkjet-printed silver nanoparticles for RFID antennas, J. Mater. Res. 28 (2013) 1254–1261.

[163] D.-Y. Shin, K. A. Brakke, Issues in color filter fabrication with inkjet printing, in: J. Korvink, P. J. Smith, D.-Y. Shin (Eds.), Inkjet-based Micromanufacturing, First Edition, Wiley-VCH Verlag GmbH & Co. KG, 2012.

[164] K. J. Kim, G. B. Kim, C. L. Vanlencia, J. F. Rabolt, Curie transition, ferroelectric crystal structure, and ferroelectricity of a VDF/TrFE(75/25) copolymer 1. The effect of the consecutive annealing in the ferroelectric state on Curie transition and ferroelectric crystal structure, J. Polym. Sci. Polym. Phys. 32 (15) (1994) 2435–2444.

[165] M. Barique, H. Ohigashi, Annealing effects on the Curie transition temperature and melting temperature of poly(vinylidene fluoride/trifluoroethylene) single crystalline films, Polymer 42 (11) (2001) 4981–4987.

[166] A. J. Lovinger, Ferroelectric polymers, Science 220 (4602) (1983) 1115–1121.

[167] G. Höhne, Another approach to the Gibbs-Thomson equation and the melting point of polymers and oligomers, Polymer 43 (17) (2002) 4689–4698.

[168] E. Bellet-Amalric, J. Legrand, Crystalline structures and phase transition of the ferroelectric P(VDF-TrFE) copolymers, a neutron diffraction study, Eur. Phys. J. B 3 (2) (1998) 225–236.

[169] B. Fillon, J. C. Wittmann, B. Lotz, A. Thierry, Self-nucleation and recrystallization of isotactic polypropylene (α phase) investigated by differential scanning calorimetry, J. Polym. Sci. Pol. Phys. 31 (10) (1993) 1383–1393.

[170] M. Calleja, M. Nordström, M. Álvarez, J. Tamayo, L. Lechuga, A. Boisen, Highly sensitive polymer-based cantilever-sensors for DNA detection, Ultramicroscopy 105 (1-4) (2005) 215–222.

[171] N. Shiraishi, T. Ikehara, D. Dao, S. Sugiyama, Y. Ando, Fabrication and testing of polymer cantilevers for VOC sensors, Sensor Actuat. A-Phys. 202 (2013) 233–239.

[172] E. Volterra, E. C. Zachmanoglou, Dynamics of vibrations, C.E. Merrill Books, 1965.

[173] C. A. Heid, J. Stevens, K. J. Livak, P. M. Williams, Real time quantitative PCR, Genome Res. 6 (10) (1996) 986–994.

[174] S.-W. Zhou, C. A. Rogers, Heat generation, temperature, and thermal stress of structurally integrated piezo-actuators, J. Intel. Mat. Syst. Str. 6 (3) (1995) 372–379.

[175] M. A. Khan, U. S. Bhansali, M. N. Almadhoun, I. N. Odeh, D. Cha, H. N. Alshareef, High-performance ferroelectric memory based on phase-separated films of polymer blends, Adv. Funct. Mater. 24 (10) (2014) 1372–1381.

[176] D. Mao, I. Mejia, H. Stiegler, B. Gnade, M. Quevedo-Lopez, Fatigue characteristics of poly(vinylidene fluoride-trifluoroethylene) copolymer ferroelectric thin film capacitors for flexible electronics memory applications, Org. Electron. 12 (8) (2011) 1298–1303.

Nomenclature

Symbols

Symbol	*Full expression*	*Unit*
a / b / c	lattice parameters	Å
$B_{\text{-3bB}}$	-3 dB-bandwidth	Hz
d	piezoelectric coefficient	m V^{-1} or C N^{-1}
d_{31}	piezoelectric coupling coefficient	m V^{-1} or C N^{-1}
D	flexural modulus	N m^{-2}
D_{el}	electric displacement	C m^{-2}
E	electric field	V m^{-1}
E_c	coercive field	V m^{-1}
F	force	N
F_{B}	blocking force	N
f	frequency	Hz
f_{res}	resonance frequency	Hz
I	second moment of area	m^4
L	cantilever length	m
P	electric polarization	C m^{-2}
P_{rem}	remanent polarization	C m^{-2}
Q	quality factor	-
Q_{l}	liquid pump rate	L min^{-1}
R	resistance	Ω
R^2	correlation coefficient	-
R_{a}	surface roughness	m
R_{p}	membrane radius	m
R_{act}	radius of piezoelectric film	m
r_{c}	radius of curvature	m
r	radial coordinate	m
s_{ijkl}^{E}	elastic compliance under constant electric field	m^2 N^{-1}

t	thickness	m
T_C	Curie temperature	°C
T_G	glass transition temperature	°C
U	voltage	V
ΔV	volume change	m^3
Y	Young's modulus	$N\ m^{-2}$
Δz	actuator deflection	m
ε_{piezo}	strain caused by the piezoelectric effect	-
ε	dielectric permittivity	$F\ m^{-1}$
$\varepsilon_{ik}^{\sigma}$	dielectric permittivity under constant stress	$F\ m^{-1}$
η	efficiency factor	-
2Θ	scattering angle in XRD measurements	°
$\Theta_{i/o}$	inlet / outlet flow	L
ν	Poisson's ratio	-
ρ	resistivity	Ω m
σ	mechanical stress	$N\ m^{-2}$

Abbreviations

AFM	atomic force microscopy
CAD	computer-aided design
DSC	differential scanning calorimetry
EAP	electroactive polymer actuator
FTIR	Fourier-transform infrared spectroscopy
IPMC	ionic polymer-metal composite
IR	infrared
LOC	lab-on-a-chip
MW	molecular weight
OLED	organic light-emitting diode

OPD	organic photodiode
OPV	organic photovoltaics
PC	polycarbonate
PDMS	poly(dimethyl siloxane)
PE	polyethylene
PEDOT:PSS	poly(3,4-ethylenedioxythiophene):polystyrene sulfonate
PET	poly(ethylene terephthalate)
PMMA	poly(methyl methacrylate)
PP	polypropylene
PVDF	poly(vinylidene fluoride)
P(VDF-TrFE)	poly(vinylidene fluoride-*co*-trifluoroethylene)
PZT	lead zirconate titanate
RF	radio frequency
RFID	radio-frequency identification
SEM	scanning electron microscope
wt	weight
XRD	X-ray diffraction

Prefixes

Symbol	*Prefix*	*10^n*
G	Giga	10^9
M	Mega	10^6
k	Kilo	10^3
m	Milli	10^{-3}
µ	Micro	10^{-6}
n	Nano	10^{-9}
p	Pico	10^{-12}

List of publications

Refereed publications

- O. Pabst, J. Perelaer, E. Beckert, U. S. Schubert, R. Eberhardt, A. Tünnermann, All inkjet-printed piezoelectric polymer actuators: Characterization and applications for micropumps in lab-on-a-chip systems, Org. Electron. 14 (12) (2013) 3423–3429.
- O. Pabst, S. Hölzer, E. Beckert, J. Perelaer, U. S. Schubert, R. Eberhardt, A. Tünnermann, Inkjet printed micropump actuator based on piezoelectric polymers: Device performance and morphology studies, Org. Electron. 15 (11) (2014) 3306-3315 (*submitted prior to submission of thesis, accepted after submission of thesis*).

Patent

- E. Beckert, O. Pabst, Mikropumpe, DE Patent 102011107046 A1, *patent pending* (2013).

Non-refereed publications:

- O. Pabst, J. Perelaer, E. Beckert, H. Becker, U. S. Schubert, R. Eberhardt, A. Tünnermann, Inkjet printing and argon plasma sintering of an electrode pattern on polymer substrates using silver nanoparticle ink, in: Proc. 26th International Conference on Digital Printing Technologies, 2010, pp. 146–149.
- O. Pabst, J. Perelaer, E. Beckert, U. S. Schubert, R. Eberhardt, A. Tünnermann, Inkjet printing of electroactive polymer actuators on polymer substrates, in: Proc. SPIE, Vol. 7976, 2011, p. 79762H.
- O. Pabst, J. Perelaer, M. Hornaff, E. Beckert, H. Becker, U. S. Schubert, R. Eberhardt, A. Tünnermann, Inkjet-Druck und Niedertemperatur-Sintern von Ag-Nanopartikeltinten auf Polymersubstraten, in: Proc. 3. GMM Workshop Mikro-Nano-Integration, 2011.
- O. Pabst, J. Perelaer, E. Beckert, U. S. Schubert, R. Eberhardt, A. Tünnermann, All inkjet-printed electroactive polymer actuators for active microoptical and polytronical systems, in: Proc. LOPE-C, 2011, pp. 139–142.
- O. Pabst, J. Perelaer, E. Beckert, U. S. Schubert, R. Eberhardt, A. Tünnermann, Erzeugung von elektroaktiven Polymeraktoren mittels Inkjet Drop-on-Demand zur

Anwendung in mikrofluidischen Systemen, in: Proc. 4. VDE/VDI Mikrosystemtechnik-Kongress, 2011, pp. 281–284.

- O. Pabst, E. Beckert, R. Eberhardt, A. Tünnermann, Inkjet printing of functional structures for lab-on-chip systems, in: Proc. Smart Systems Integration, 2012.
- O. Pabst, J. Perelaer, E. Beckert, U. S. Schubert, R. Eberhardt, A. Tünnermann, Static and dynamic behavior of all inkjet-printed piezoelectric polymer actuators for use in microfluidic systems, in: Proc. Actuator, 2012, pp. 414–417.
- E. Beckert, O. Pabst, J. Perelaer, U. S. Schubert, R. Eberhardt, A. Tünnermann, Inkjet printing for applications in microfluidic lab-on-chip systems, in: Proc. Digital Fabrication, 2012, pp. 457–460.
- E. Beckert, R. Eberhardt, O. Pabst, F. Kemper, Z. Shu, A. Tünnermann, J. Perelaer, U. Schubert, H. Becker, Inkjet printed structures for smart lab-on-chip systems, in: Proc. SPIE, Vol. 8615, 2013, p. 86150E.
- O. Pabst, E. Beckert, J. Perelaer, U. S. Schubert, R. Eberhardt, A. Tünnermann, All inkjet-printed electroactive polymer actuators for microfluidic lab-on-chip systems, in: Proc. SPIE, Vol. 8687, 2013, p. 86872H.
- E. Beckert, O. Pabst, Z. Shu, J. Perelaer, R. Eberhardt, A. Tünnermann, U. S. Schubert, H. Becker, Inkjet-printed functionalities for microfluidic lab-on-a-chip systems, in: Proc. Smart Systems Integration, 2013.

Presentations

- O. Pabst, J. Perelaer, E. Beckert, U. S. Schubert, R. Eberhardt, A. Tünnermann, All inkjet-printed electroactive polymer actuators for lab-on-a-chip systems, at: LOPE-C 2013, 11.-13.06.2013, München, Germany.
- O. Pabst, E. Beckert, R. Eberhardt, A. Tünnermann, Inkjet printing of functional materials for applications in polymer-based microfluidic lab-on-a-chip systems, at: 24th Micromechanics and Microsystems Europe Conference MME, 01.-03.09.2013, Espoo, Finland.
- O. Pabst, F. Kemper, Z. Shu, S. Mittwoch, E. Beckert, Drucken funktionaler Materialien für Lab-on-Chip Systeme, at: OptoNet-Workshop Additive Fertigung, 6.11.2013, Jena, Germany.

Publications not directly related to the topic of the thesis

- O. Pabst, M. Schiffer, E. Obermeier, T. Tekin, K. D. Lang, H.-D. Ngo, Measurement of Young's modulus and residual stress of thin SiC layers for MEMS high temperature applications, in: Proc. SPIE, Vol. 8066, 2011, pp. 806608–806608–9.
- O. Pabst, M. Schiffer, E. Obermeier, T. Tekin, K. Lang, H.-D. Ngo, Measurement of Young's modulus and residual stress of thin SiC layers for MEMS high temperature applications, Microsystem Technologies 18 (7-8) (2012) 945–953.
- S. Wünscher, S. Stumpf, A. Teichler, O. Pabst, J. Perelaer, E. Beckert, U. S. Schubert, Localized atmospheric plasma sintering of inkjet printed silver nanoparticles, J. Mater. Chem. 22 (47) (2012) 24569–24576.
- D. Ernst, B. Bramlage, S. Gebhardt, A. Schönecker, O. Pabst, H.-J. Schreiner, Enhanced large signal performance of PZT thick film actuators for active micro-optics, in: Proc. IEEE International Symposium on the Applications of Ferroelectric and Workshop on Piezoresponse Force Microscopy (ISAF/PFM), 2013, pp. 5–8.
- D. Ernst, B. Bramlage, S. Gebhardt, A. Oberdörster, O. Pabst, F. Wippermann, Plenoptic camera with adaptable depth of field using PZT thick film actuators, in: Proc. Actuator, 2014, pp. 134–137.

Danksagung / Acknowledgements

An dieser Stelle möchte ich mich herzlich bei all denen bedanken, die mich während der Bearbeitung meiner Dissertation unterstützt haben.

An erster Stelle gilt mein Dank Prof. Dr. Andreas Tünnermann für die wissenschaftliche Betreuung der Arbeit, Anregungen und Diskussionen. Weiterhin gilt mein Dank Dr. Ramona Eberhardt und Dr. Erik Beckert für die Möglichkeit, die Arbeit in der Abteilung Feinwerktechnik des Fraunhofer-Instituts für Angewandte Optik und Feinmechanik (IOF) anzufertigen. Ihre wohlwollende Unterstützung sowie die gewährte Freiheit bei der Ausgestaltung des Promotionsthemas haben diese Arbeit ermöglicht. Weiterhin bedanke ich mich bei allen externen Gutachtern für die Bewertung der Arbeit.

Für die konstruktive Arbeitsatmosphäre sowie viele gute Diskussionen danke ich allen Mitarbeitern der Abteilung Feinwerktechnik des IOF, insbesondere der Gruppe Mikromontage und Systemintegration. Besonderer Dank für unzählige fachliche und nicht-fachliche Gespräche gilt hierbei Thomas Burkhardt, Dr. Claudia Reinlein, Sandra Müller, Andreas Joswig, Nicolas Lange, Jan Kinast, Zhe Shu, Falk Kemper, Steffen Gramens sowie Andrea Kliner.

Für die Unterstützung in Form von Messungen bedanke ich mich herzlich bei folgenden, teilweise ehemaligen Kollegen aus dem IOF: Dr. Sergiy Yulin sowie Viatcheslav Nesterenko für die Durchführung von XRD-Messungen, Andrea Morales für einen Teil der Vibrometer-Messungen, Nicolas Lange für das Aufnehmen von Kraft-Weg Kennlinien und die Gestaltung von Figure 4.2, Stephan Mittwoch für einzelne Sintertests, Roland Klein und Michael Appelfelder für das Erstellen von LabVIEW-Steuerungen sowie Christian Hupel für REM-Aufnahmen. Andreas Kamm danke ich für das Erstellen von CAD-Modellen der Pumpsubstrate. Hans-Ulrich Abbe und Ralf Steinkopf gilt mein Dank für die Fertigung der Pumpsubstrate. Weiterhin danke ich folgenden Kollegen aus der Schubert-Group (Friedrich-Schiller-Universität Jena, Institut für Organische Chemie und Makromolekulare Chemie) für die freundliche Unterstützung: Stefan Hölzer für AFM-Aufnahmen sowie Hilfe bei der Auswertung von AFM-, DSC- und XRD-Messungen, Renzo Paulus für DSC-Analysen sowie Igor Perevyazko für die Unterstützung bei Viskositätsmessungen. Dr. Robert Schulze (Friedrich-Schiller-Universität Jena, Lehrstuhl für Materialwissenschaft) danke ich für Empfehlungen zur Durchführung von Morphologie-Untersuchungen.

I would especially like to thank Dr. Jolke Perelaer (previously Schubert-Group) for countless discussions, reading and commenting my manuscripts and for inviting me to attend the inkjet meetings at Schubert-Group. This support helped a lot to progress with my research.

Furthermore, I would like to say *thank you* or *kiitos paljon* to the colleagues at VTT Technical Research Centre of Finland in Espoo for support, discussions, a great research environment and their warm hospitality during my stay at VTT: Ari Alastalo, Tomi Mattila, Marc Allen, Kim Eiroma, Jaakko Leppäniemi, Kimmo Ojanperä, Mika Suhonen and Anna Leimaussyy.

Für Unterstützung und starken Rückhalt bedanke ich mich bei meinen Eltern, Geschwistern, Nichten und Freunden. Darüber hinaus geht ein lieber Dank an Tiina für Motivation, Verständnis und Dasein – *kiitos tuesta ja kannustuksesta ja että olette minun rakas*.

Ehrenwörtliche Erklärung

Ich erkläre hiermit ehrenwörtlich, dass ich die vorliegende Arbeit selbstständig, ohne unzulässige Hilfe Dritter und ohne Benutzung anderer als der angegebenen Hilfsmittel und Literatur angefertigt habe. Die aus anderen Quellen direkt oder indirekt übernommenen Daten und Konzepte sind unter Angabe der Quelle gekennzeichnet. Bei der Auswahl und Auswertung folgenden Materials haben mir die nachstehend aufgeführten Personen in der jeweils beschriebenen Weise unentgeltlich geholfen:

1. Stefan Hölzer (Friedrich-Schiller-Universität Jena, Institut für Organische Chemie und Makromolekulare Chemie): Hilfe bei der Auswertung der in Abschnitt 5.5 aufgeführten Untersuchungen zur Morphologie gedruckter P(VDF-TrFE) Schichten.
2. Dr. Sergiy Yulin (Fraunhofer IOF): Unterstützung bei der Auswertung von XRD-Messungen.

Weitere Personen waren an der inhaltlich-materiellen Erstellung der vorliegenden Arbeit nicht beteiligt. Insbesondere habe ich hierfür nicht die entgeltliche Hilfe von Vermittlungs- bzw. Beratungsdiensten (Promotionsberater oder andere Personen) in Anspruch genommen. Niemand hat von mir unmittelbar oder mittelbar geldwerte Leistungen für Arbeiten erhalten, die im Zusammenhang mit dem Inhalt der vorgelegten Dissertation stehen. Die Arbeit wurde bisher weder im In- noch im Ausland in gleicher oder ähnlicher Form einer anderen Prüfungsbehörde vorgelegt. Die geltende Promotionsordnung der Physikalisch-Astronomischen Fakultät ist mir bekannt.

Ich versichere ehrenwörtlich, dass ich nach bestem Wissen die reine Wahrheit gesagt und nichts verschwiegen habe.

Jena, ...

Oliver Pabst